Dynamics at Solid State Surfaces and Interfaces
Volume 2: Fundamentals
Edited by Uwe Bovensiepen, Hrovje Petek, and Martin Wolf
WILEY-VCH Verlag GmbH & Co. KGaA
Weinheim, 2012

2
Quasi-Particles and Collective Excitations

Evgueni V. Chulkov, Irina Sklyadneva, Mackillo Kira, Stephan W. Koch, Jose M. Pitarke, Leonid M. Sandratskii, Paweł Buczek, Kunie Ishioka, Jörg Schäfer, and Martin Weinelt

2.1
Introduction

A solid contains about 10^{22} electrons and vibrating ions per cubic centimeter all of which interact with each other via the long-range Coulomb interaction. In this respect, it is astounding that we can describe the electronic band structure of a solid in a single-particle picture and obtain in most cases reasonable agreement with experimental data. In such a single-particle approach, we hide the electron–electron interaction in some average potential and neglect all the other elementary excitations of the solid. Essentially, we consider a bare electron moving through the modified periodic potential of the crystal. The outcome of such a simplified model are Bloch states characterized by the wave vector $\mathbf{k}$ and the dispersion relation $E(\mathbf{k})$. The electron's velocity and mass are modified by the crystal potential. They can be expressed by the first and second derivatives of $E(\mathbf{k})$ with respect to $\mathbf{k}$ (see, for example, Appendix E in Ref. [1]). The interaction of the electron with the crystal potential is now included in the dispersion relation. The electron is no longer free but can be considered as a quasi-electron with a $\mathbf{k}$-dependent velocity and effective mass.

We can extend this concept of the quasi-electron and argue that all kinds of elementary excitations in a solid that modify the properties of the electron contribute to its quasi-particle nature. For example, each electron repels all the other electrons of the crystal by Coulomb interaction. This must lead to a positive cloud around each electron relative to the average electron density of the solid. The charge of the electron becomes screened and the long-range Coulomb interaction is replaced by the screened Coulomb interaction. This screened Coulomb interaction can be described by individual electron–electron scattering processes in which two electrons

Dynamics at Solid State Surfaces and Interfaces: Volume 2: Fundamentals, First Edition.
Edited by Uwe Bovensiepen, Hrvoje Petek, and Martin Wolf.

transfer among themselves a particular momentum Δk and energy ΔE. In contrast to the steady state of Bloch electrons, the screened Coulomb interaction among the electrons leads to a finite lifetime τ of all interacting electronic states. Furthermore, the dynamics of the screening process may lead to collective excitations. At the birth of a quasi-particle, such as a photoexcited electron or hole, the long-range Coulomb interaction is barely suppressed by screening. This can lead to collective oscillations of the electron gas, the so-called plasmons. At lower electron densities, we retrieve some of the long-range character of the Coulomb interaction. This becomes particularly important for systems with an energy gap between ground and first excited electronic state, where the mutual interaction between excited electrons and holes leads to the formation of excitons. Besides carrier–carrier scattering, the Coulomb interaction of the moving electron with the ion cores leads to deformation of the lattice, which can be described by emission and reabsorption of phonons, the quanta of the lattice vibrations. The electron becomes dressed by a virtual phonon cloud that it carries through the crystal. This interaction, where the polarization of the lattice acts back on the electron, can be transformed into a quasi-particle called a polaron. The electron may become heavier and slower and the band dispersion $E(\mathbf{k})$ will have a smaller slope near the Fermi level, where such low-energy excitations are important. The electron with its phonon cloud behaves like a noninteracting particle with a $\mathbf{k}$-dependent effective mass.

So far we have neglected the spin of electrons. It is the spins, in combination with the Pauli principle, that underlie the exchange interaction. The latter can lead to alignment of the electron spins and support a magnetically ordered ground state. The low-energy excitations of this ground state are spin waves and the corresponding quanta are called magnons. These collective magnetic excitations will couple to electrons and phonons and enrich the response function of magnetic materials.

The coarse energy- and timescales of quasi-particle and collective excitations are illustrated in Figure 2.1. The decay rate $\hbar/\tau$, and thus lifetime τ of a quasi-particle, relates to the natural linewidth Γ of the corresponding photoemission line, and thus to the imaginary part of the self energy Σ of the corresponding state via

$$\hbar/\tau = \Gamma = -2\,\mathrm{Im}\,\Sigma \tag{2.1}$$

This relationship allows us to experimentally detect and analyze the signatures of quasi-particle and collective excitations in both energy- and time-resolved spectroscopy. However, one must be careful when evaluating lifetimes from energy-resolved spectroscopy via Eq. (2.1) since besides the decay rate, the band dispersion, the inhomogeneous broadening, and the dephasing processes may add to the linewidth in a solid-state system. Though often used as a rule of thumb, the lifetime of a quasi-particle should not be mistaken for the time it requires to excite the quasi-particle [2, 3].

This chapter is intended as a short introduction to the physics of elementary excitations in solids. Each section is written by experts in the field who are listed below. To structure the theoretical description, we make a distinction between quasi-particle and collective excitations that should not be taken axiomatic.

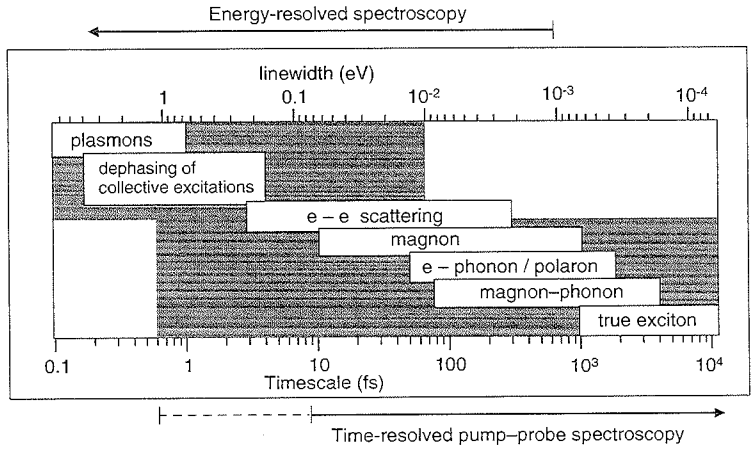

Figure 2.1 Quasi-particle and collective excitations. The lifetime of an excitation τ and its approximate energy Γ are related via $\Gamma \cdot \tau = \hbar = 658$ meV fs. After Ref. [4].

In Section 2.2, electrons and phonons are introduced by Evgueni Chulkov and Irina Sklyadneva with an emphasis on electron–phonon coupling in metals. This is followed by a discussion of the physics of coherent and incoherent excitons in semiconductor quantum wells and their signatures in terahertz and photoluminescence spectroscopy by Mackillo Kira and Stephan W. Koch. A contribution by Jose M. Pitarke on polarons, that is, electron–phonon coupling in polar and ionic materials, completes the description of quasi-particle excitations.

Section 2.3 deals with collective excitations. Jose M. Pitarke gives an introduction to plasmons, the collective oscillations of the electron gas in metals. Magnons are the low-energy collective excitations in magnetically ordered systems. Their physics is discussed by Leonid M. Sandratskii and Paweł Buczek.

Many experimental techniques allow us to study quasi-particle formation and decay, most of which are discussed in Volume 1 of this series. Section 2.4 restricts itself to an overview of three techniques quite prominent in the field. First, the all-optical ultrafast spectroscopy of coherent phonons, as an example of collective excitations, is introduced by Kunie Ishioka. Jörg Schäfer summarizes recent developments in high-resolution photoemission spectroscopy, which gives experimental access to elementary excitations in the energy domain. Finally, the signatures of quasi-particle and collective exciations in time-resolved photoelectron spectroscopy are outlined by Martin Weinelt.

There is a wealth of books and review articles on quasi-particle and collective excitations. For a comprehensive introduction, we refer the reader to the textbooks by Kittel, Madelung, and Czycholl [5–7]. Furthermore, there are a number of excellent reviews, for example, [4, 8–12], which may be useful.

2.2 Quasi-Particles

2.2.1 Electrons and Holes

As outlined in the introduction, various experiments, in particular photoemission measurements, show that excitation spectra of metals can be understood in terms of excited single particles, electrons and holes, with certain momentum $\mathbf{k}$ and energy $E(\mathbf{k})$ [13]. This picture is analogous to that of a free (noninteracting) electron gas (FEG) model where an electron excitation is formed by transition of an electron from an occupied state (below the Fermi level, E_F) to an unoccupied state (above E_F) with a hole left below E_F [14]. These two excited particles are protected from decay by the absence of any interaction between the electrons in the FEG model irrespective of the excitation energy.

In real systems despite that electrons strongly interact with each other, a single-particle excitation picture is still valid for relatively low excitation energies since electron–electron interaction results in the decay of excited electrons and holes, that is, final lifetimes of these particles. The final lifetime or lifetime broadening is also influenced by the interaction of the excited electron with other (quasi)particles [15], for example, with single-particle excitations, electrons and holes [9], and with collective excitations, phonons [16], magnons [17], and plasmons [18].

Electron excitation energies and the excited particle decay being closely related to the electron band structure of a metal are also related to the phonon, magnon, and plasmon spectra of a metal via the interaction with these quasi-particles and depend on the dimensionality of a system. For instance, on metal surfaces the decay of electrons excited in surface electron states will be modified by the interaction with surface phonons, magnons, and plasmons [9, 16–18]. Therefore, decay mechanisms on surfaces and a single-particle interpretation of electron excitations may be very different from those in bulk. Bulk metals exibit three-dimensional translational symmetry that results in discrete electron spectra at any selected momentum in the Brillouin zone. With such an electronic structure, the decay of excited electrons in the absence of defects can occur only via inelastic scattering of the excited particle with other electrons and other quasi-particles (phonons, magnons, and plasmons). The formation of a metal surface leads to the loss of translational symmetry in the direction perpendicular to the surface. As a result, such a semiinfinite metal exibits only two-dimensional (2D) translational symmetry and the bulk states form a continuum of electronic states with energy gaps in the projection of the bulk band structure onto the 2D surface Brillouin zone. As a consequence, at metal surfaces there exist not only gap surface states and gap image potential states but also surface and image potential resonances can be found lying outside the energy gaps and, therefore, are degenerate in energy with bulk electronic states. The change in the character of the electronic states from gap state to resonance results in a change in the dominating decay mechanism. Gap states decay via many-body electron–electron (inelastic) scattering, while resonance decay via one-electron transition, that is,

energy conserving resonant electron transfer into the bulk metal states. The latter mechanism is significatly more efficient than inelastic electron–electron scattering for electrons excited into resonance states. This one-electron decay mechanism does not exist in bulk metals. However, it is ubiquitous on clean metal surfaces, on surfaces with adatoms/clusters/islands, and on surfaces covered with adlayers making a single particle interpretation of electron excitations more complicated.

2.2.2 Phonons

One of the most important physical phenomena in solids is the vibration of atoms about their equilibrium positions. In general, a description of such a motion is a formidable problem. In solids, it can be simplified (i) by taking into account the lattice translational symmetry and (ii) making approximations such as adiabatic and harmonic. The first one allows us to reduce the problem to the atomic motion in the primitive unit cell containing a reduced number of atoms and electrons, the second simplifies the equation of motion.

2.2.2.1 Adiabatic Approximation

To exclude from our consideration the motion of electrons around the ion cores, the well-known adiabatic approximation is used. This approximation means that the nuclei and electron degrees of freedom can be decoupled due to the considerable difference in their masses. In this case, (i) the values concerning the motion of electrons are calculated at the fixed equilibrium positions of the ion cores and (ii) the dynamics of the ion cores is considered as a motion in an averaged potential field generated by the electrons.

2.2.2.2 Harmonic Approximation

Let us consider the potential energy of a crystal as a function of atomic positions $\mathbf{R}_{m\alpha} = \mathbf{R}^{\circ}_{m\alpha} + \mathbf{S}_{m\alpha}$. Here, $\mathbf{R}^{\circ}_{m\alpha} = \mathbf{R}^{\circ}_{m} + \tau^{\circ}_{\alpha}$, superscript $\circ$ indicates the equilibrium position expressed in terms of the position $\mathbf{R}^{\circ}_{m}$ of unit cell m, and the position τ°_{α} of atom α in the unit cell, and $\mathbf{S}_{m\alpha}$ is a displacement of atom α in unit cell m from the equilibrium position. In most of the physically interesting cases, the relative displacements of the atoms are small compared to interatomic distances. Therefore, one can expand the potential energy in powers of the atomic displacements from the equilibrium position:

$$V(\ldots \mathbf{R}_{m\alpha} \ldots) = V(\ldots \mathbf{R}^{\circ}_{m\alpha} \ldots) + \sum_{m\alpha i} \left.\frac{\partial V}{\partial R_{m\alpha i}}\right|_{\mathbf{R}_{m\alpha}=\mathbf{R}^{\circ}_{m\alpha}} S_{m\alpha i} + \frac{1}{2}\sum_{\substack{m\alpha i \\ n\beta j}} \left.\frac{\partial^2 V}{\partial R_{m\alpha i}\partial R_{n\beta j}}\right|_{\substack{\mathbf{R}_{m\alpha}=\mathbf{R}^{\circ}_{m\alpha} \\ \mathbf{R}_{n\beta}=\mathbf{R}^{\circ}_{n\beta}}} S_{m\alpha i} S_{n\beta j} + \cdots \tag{2.2}$$

Here, $R_{m\alpha i}$, $R^{\circ}_{m\alpha i}$, and $S_{m\alpha i}$ are the components of vectors $\mathbf{R}_{m\alpha}$, $\mathbf{R}^{\circ}_{m\alpha}$, and $\mathbf{S}_{m\alpha}$, respectively. Since we are interested in the atomic motion, the first term can be

omitted: it does not depend on $\mathbf{S}_{m\alpha}$. The linear term vanishes as the potential energy is expanded at the equilibrium position of atoms where the potential energy has to have an absolute or relative minimum to stabilize the crystal lattice. The first term that determines the dynamical properties of a crystal is the quadratic one. If we take the potential energy of a crystal in this quadratic form and neglect the higher order terms in the Expansion 2.2, we express the potential energy in the so-called harmonic approximation.

2.2.2.3 Lattice Dynamics

Let us define

$$\underset{n\beta j}{\Phi_{m\alpha i}} = \left.\frac{\partial^2 V}{\partial X_{m\alpha i}\partial X_{n\beta j}}\right|_{\substack{\mathbf{R}_{m\alpha}=\mathbf{R}^{\circ}_{m\alpha}\\ \mathbf{R}_{n\beta}=\mathbf{R}^{\circ}_{n\beta}}} \tag{2.3}$$

Now one can write the equation of motion where each atom can be considered as a simple harmonic oscillator:

$$M_\alpha \ddot{S}_{m\alpha i} + \sum_{n\beta j} \underset{n\beta j}{\Phi_{m\alpha i}} S_{n\beta j} = 0 \tag{2.4}$$

Here, M_α is the mass of atom α and $\underset{n\beta j}{\Phi_{m\alpha i}}$ are interatomic force constants that determine the force acting on atom α in unit cell m along direction i when atom β in unit cell n shifts in j-direction over distance $S_{n\beta j}$, while all other atoms keep their equilibrium positions.

The simplest solutions of the equation of motion are normal crystal vibrations when all atoms vibrate with the same frequency ω. The number of such normal vibrations and frequencies is equal to the number of atoms N multiplied by 3. Such vibrations are equivalent to a system of independent harmonic oscillators with frequencies equal to the normal frequencies of the lattice. A normal vibration mode can be taken in a general form of $S_{m\alpha i} = A_{\alpha i}\cdot\exp\left[i(\mathbf{q}\cdot\mathbf{R}^{\circ}_{m\alpha}-\omega t)\right]$, where $\mathbf{q}$ is a wave vector showing the direction of wave propagation, ω is the circular frequency of the wave, and $A_{\alpha i}$ is the amplitude of vibration. The energies of the normal modes are quantized and the quantum of energy, $\omega_{\mathbf{q}}$, is associated with an elementary excitation, the phonon. In the harmonic approximation, the lattice dynamics can be expressed in terms of a system of noninteracting phonons that can be considered as quasi-particles since, for convenience, a momentum $\hbar\mathbf{q}$ is assigned to each phonon in mode $\mathbf{q}$. Thus, the problem is to find the energies (or frequencies) of the independent phonons as a function of their wave vector, $\omega = \omega(\mathbf{q})$, the so-called phonon dispersion.

By substituting $S_{m\alpha i}$ into the equation of motion (Eq. (2.4)) and multiplying by $\exp\left[-i(\mathbf{q}\mathbf{R}^{\circ}_{m\alpha}-\omega t)\right]$, we obtain

$$\sum_{\beta j}\left[\left(\sum_{\mathbf{h}} \underset{\beta j}{\Phi^{\mathbf{h}}_{\alpha i}} \exp\left[i\mathbf{q}(\mathbf{h}+\tau_\beta-\tau_\alpha)\right]\right) - \sqrt{M_\alpha M_\beta}\,\omega^2\,\delta_{\alpha\beta}\,\delta_{ij}\right] A_{\beta j} = 0 \tag{2.5}$$

where $\mathbf{h} = \mathbf{R}^{\circ}_n - \mathbf{R}^{\circ}_m$. Let us define the dynamical matrix of a crystal as

$$\underset{\beta j}{D_{\alpha i}}(\mathbf{q}) = \frac{1}{\sqrt{M_\alpha M_\beta}} \sum_{\mathbf{h}} \underset{\beta j}{\Phi^{\mathbf{h}}_{\alpha i}} \exp\left[i\mathbf{q}(\mathbf{h}+\tau_\beta-\tau_\alpha)\right] \tag{2.6}$$

Now, one can rewrite Eq. (2.5) as a system of linear equations:

$$\sum_{\beta j}\left[\underset{\beta j}{D_{\alpha i}}(\mathbf{q}) - \omega^2\,\delta_{\alpha\beta}\,\delta_{ij}\right]\varepsilon_{\beta j}(\mathbf{q}) = 0, \tag{2.7}$$

which is equivalent to

$$\det\left|\underset{\beta j}{D_{\alpha i}}(\mathbf{q}) - \omega^2\,\delta_{\alpha\beta}\,\delta_{ij}\right| = 0, \tag{2.8}$$

where $\varepsilon_{\beta j}(\mathbf{q}) = \sqrt{M_\beta}\cdot A_{\beta j}$. Equations (2.7) and (2.8) are general and can be used for 1D, 2D, and 3D translationally invariant systems. For each $\mathbf{q}$, there are $3n$ vibrational modes or phonon branches (here n is the number of atoms in the unit cell) with frequencies $\omega_{\mathbf{q},\nu}(\nu = 1,\ldots,3n)$ and $3n$ eigenvectors $\hat{\varepsilon}_{\mathbf{q},\nu}$ describing the polarization of the wave of displacements.

To evaluate the phonon dispersion of normal modes, various approximations are used. For instance, if we consider only acoustic modes (phonons) that at low frequencies have a linear relationship between their frequency and wave vector $\mathbf{q}$ and extend the low-frequency limit to the maximum phonon frequency $\omega_{\max}$, we obtain the Debye model for phonons where $\omega_{\max}$ is replaced by the Debye frequency ω_{D}. In this model, optical branches of the phonon spectrum correspond to large values of $\mathbf{q}$. The optical phonon modes can also be taken into account in the Einstein model where the phonon density of states (DOS) is simply $F(\omega) = \delta(\omega-\omega_{\mathrm{E}})$. In this approximation, the frequencies of optical phonons do not depend on $\mathbf{q}$ and are equal to the Einstein frequency ω_{E}.

2.2.2.4 Phonons at Surfaces

At surfaces the number of nearest neighbors changes when compared to the bulk. As a result, vibrational modes appear that are not allowed within the solid. These modes propagate along the surface with wave vector $\mathbf{q}$ ($\mathbf{q}$ is now two dimensional) and decay exponentially in amplitude into the bulk. Such modes are called surface phonons and include both atomic vibrations localized at the surface and manifestations of bulk vibrations at the surface, the so-called surface resonances. The surface-localized modes exist in the gaps of the bulk phonon spectrum where particular values of $\mathbf{q}$ are not allowed for bulk phonons. The surface atoms can also acquire relatively large (or small) displacement amplitudes compared to atoms in the bulk due to the change in the force constants near the surfaces. The corresponding decrease (or increase) in coupling constants tends to lower (or elevate) the vibrational mode frequencies such that they lie beyond the limits of the bulk phonon frequencies.

As far as the surface resonances are concerned, they exist inside the bulk continuum and have both surface-localized and bulk-like components. To illustrate

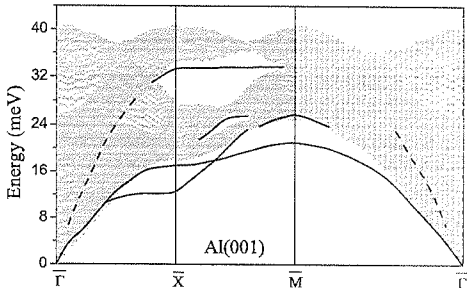

Figure 2.2 Example of a calculated dispersion of surface vibrational modes: the surface phonons (solid lines) and surface resonances (dashed lines) on Al(001) are shown together with the bulk vibrational modes projected on the two-dimensional Brillouin zone of the Al(001) surface (gray dots).

the above, Figure 2.2 shows the dispersion of the surface phonons and resonances on the Al(001) surface.

2.2.3 Electron–Phonon Coupling in Metals

The effect produced by the moving lattice on the conducting electrons can be considered as the scattering of electrons by phonons or as the electron–phonon (e–ph) coupling. As a result of this interaction, an electron can change its momentum and (i) emit a phonon to be released from its excess energy or (ii) a phonon can be absorbed by an electron.

The e–ph interaction is a fundamental many-body process that can be tested both experimentally and theoretically. For example, this interaction contributes to the finite lifetime of excited electrons (cf. Section 2.4.3.3). In addition, at the Fermi level, within a typical phonon energy $\hbar\omega_{max}$, the electronic dispersion is renormalized due to the scattering of electrons by phonons such that the dispersion becomes flatter (cf. Section 2.4.2.2). As a result, the electron's effective mass at the Fermi energy and the density of states is enhanced [19]. The increase in the effective mass can be described by the electron–phonon mass enhancement parameter λ: $m^* = m_0(1+\lambda)$, where m^* and m_0 are the effective masses with and without taking into account the e–ph interaction, respectively.

The effect of the e–ph coupling on the dispersion and lifetime of electronic states can be expressed in terms of the complex e–ph self-energy Σ_{e-ph}. The real part of the self-energy, $\mathrm{Re}\Sigma_{e-ph}$, determines the renormalization of an electronic energy band i close to the Fermi level.

$$m^*_{(i)}(\mathbf{k}) = m_0\left(1-\frac{\partial \mathrm{Re}\Sigma_{e-ph}(\mathbf{k};\omega)}{\partial\omega}\right) \equiv m_0(1+\lambda_{(i)}(\mathbf{k})). \tag{2.9}$$

The phonon-induced decay rate (lifetime broadening) Γ_{e-ph} of an electronic state can be obtained from the imaginary part $\mathrm{Im}\Sigma_{e-ph}$ of the self-energy:

$\Gamma_{e-ph} = 2\mathrm{Im}\,\Sigma_{e-ph}$. All these quantities are related to the Eliashberg spectral function [19, 20] $\alpha^2F(\omega)$. For an initial electron state (i) with momentum $\mathbf{k}$ and energy ε_i

$$\alpha^2F^{E(A)}_{(i)}(\mathbf{k};\omega) = \sum_{\nu,f}\int d\mathbf{q}\,\delta(\varepsilon_i-\varepsilon_f \mp \omega_{\mathbf{q},\nu}) \times|g^{i,f}(\mathbf{k},\mathbf{q},\nu)|^2\delta(\omega-\omega_{\mathbf{q},\nu}). \tag{2.10}$$

It is nothing else than the phonon density of states weighted by the e–ph coupling due to phonon emission (E, sign " − " in the delta function) and phonon absorption (A, sign " + " in the delta function) processes. During phonon emission, an electron is scattered from $\mathbf{k}$ to $\rightarrow\mathbf{k}' = \mathbf{k}-\mathbf{q}$ creating a phonon with momentum $\mathbf{q}$. In the phonon absorption process, an electron is scattered from $\mathbf{k}$ to $\rightarrow\mathbf{k}' = \mathbf{k}+\mathbf{q}$ absorbing a phonon with momentum $\mathbf{q}$. The summation in Eq. (2.10) is carried out over all possible final states (f) and phonon modes ν. The probability of electron scattering from an initial state (i) with momentum $\mathbf{k}$ to a final electronic state (f) with momentum $\mathbf{k}' = \mathbf{k}\mp\mathbf{q}$ by emission (absorption) of a phonon ($\mathbf{q},\nu$) is described by the e–ph matrix element $g^{i,f}(\mathbf{k},\mathbf{q},\nu)$:

$$g^{i,f}(\mathbf{k},\mathbf{q},\nu) = \sqrt{\frac{1}{2M\omega_{\mathbf{q},\nu}}}\langle\Psi_{\mathbf{k}i}|\hat{\varepsilon}_{\mathbf{q},\nu}\,\delta V_{\mathbf{q},\nu}|\Psi_{\mathbf{k}\mp\mathbf{q}f}\rangle. \tag{2.11}$$

Here, M is the atomic mass, $\Psi_{\mathbf{k}i}$ and $\Psi_{\mathbf{k}\mp\mathbf{q}f}$ are the electronic wave functions for the initial and final states, respectively. $\delta V_{\mathbf{q},\nu}$ gives the gradient of the crystal potential with respect to atomic displacements induced by the phonon mode ($\mathbf{q},\nu$) with frequency $\omega_{\mathbf{q},\nu}$ and phonon polarization vector $\hat{\varepsilon}_{\mathbf{q},\nu}$. As an example, Figure 2.3 shows

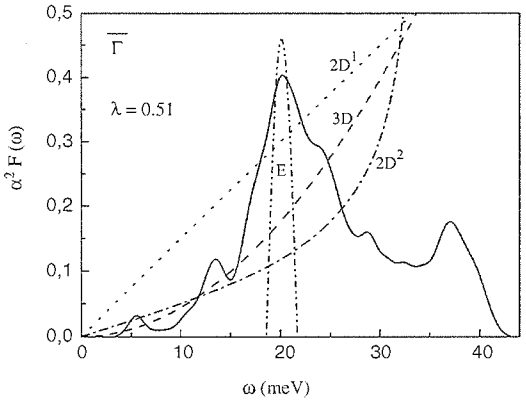

Figure 2.3 Example of a calculated Eliashberg spectral function, $\alpha^2F(\omega)$, for the surface electronic state at the $\bar{\Gamma}$ point of the surface Brillouin zone of Al(001) (solid line). Also shown are the spectral functions obtained in the 3D Debye model (dashed line), in the 2D Debye model when only the first-order diagram is included ($2D^1$, dotted line), in the 2D Debye model with the first- and second-order diagrams included ($2D^2$, dashed-dotted line), and in the Einstein approximation (E).

the Eliashberg spectral function for the surface electronic state at the $\bar{\Gamma}$ point of the Al (001) surface (solid line) [21].

The inverse lifetime or lifetime broadening $\Gamma_{e-ph} = \hbar/\tau$ is the integral over all the scattering events that conserve energy and momentum [19].

$$\begin{aligned}\Gamma^{(i)}_{e-ph}(\mathbf{k};T) &= -2\,\mathrm{Im}\,\Sigma_{e-ph} \\ &= 2\pi\hbar\int_0^\infty \{\alpha^2 F^{E}_{(i)}(\mathbf{k};\omega)[1+n(T;\omega)-f(T;\varepsilon_i-\omega)] \\ &\quad + \alpha^2 F^{A}_{(i)}(\mathbf{k};\omega)[n(T;\omega)+f(T;\varepsilon_i+\omega)]\mathrm{d}\omega. \end{aligned} \tag{2.12}$$

Here, f and n are the Fermi and Bose distribution functions, which introduce the temperature dependence of Γ_{e-ph}. Since the phonon energies are small compared to the electronic energy scale, one can neglect the change in energy in the e–ph scattering processes and assume that $\delta(\varepsilon_i - \varepsilon_f \mp \omega_{\mathbf{q},\nu}) \approx \delta(\varepsilon_i - \varepsilon_f)$. This so-called quasi-elastic assumption allows us to use the same Eliashberg function for both emission and absorption processes:

$$\begin{aligned}\Gamma^{(i)}_{e-ph}(\mathbf{k};T) = 2\pi\hbar\int_0^\infty \alpha^2 F_{(i)}(\mathbf{k};\omega)[1-f(T;\varepsilon_i-\omega) \\ +f(T;\varepsilon_i+\omega)+2n(T;\omega)]\mathrm{d}\omega. \end{aligned} \tag{2.13}$$

Let us obtain the behavior of the e–ph induced linewidth in the limiting cases. When $T \to 0$ and the electronic energy ε_i exceeds the maximum phonon energy $\hbar\omega_{max}$

$$T \to 0 : \Gamma^{(i)}_{e-ph}(\mathbf{k}) = 2\pi\hbar\int_0^{\omega_{max}} \alpha^2 F(k;\omega)\mathrm{d}\omega. \tag{2.14}$$

Since at $T = 0$ all the electronic states above the Fermi energy, E_F, are empty, electrons cannot scatter into a hole at the Fermi level. In the same way, the hole cannot decay into a lower energy state as only phonon emission is allowed. Therefore, the linewidth for holes at E_F is equal to zero and they have infinite lifetime. As the temperature is increased, some electronic states above E_F become occupied and can now fill the hole by emitting phonons or the holes can decay to a lower energy state by phonon absorption. Γ_{e-ph} increases monotonically with temperature up to a maximum value at $\omega = \omega_{max}$. An important feature of the e–ph interaction is the linear temperature dependence of Γ_{e-ph} at elevated temperatures, when $k_B T$ is higher than the maximum phonon energy. In this limit, Eq. (2.13) can be written as

$$\Gamma^{(i)}_{e-ph}(\mathbf{k};T) = 2\pi\lambda_{(i)}(\mathbf{k})\,k_B T \tag{2.15}$$

with a slope determined by the electron–phonon coupling parameter λ [19]

$$\lambda_{(i)}(\mathbf{k}) = 2\int_0^{\omega_{max}} \frac{\alpha^2 F_{(i)}(\mathbf{k};\omega)}{\omega}\mathrm{d}\omega. \tag{2.16}$$

As an example, the temperature dependence of Γ_{e-ph} is shown in Figure 2.4 (solid line) for the surface electronic state at the $\bar{\Gamma}$ point of the Al(001) surface [21].

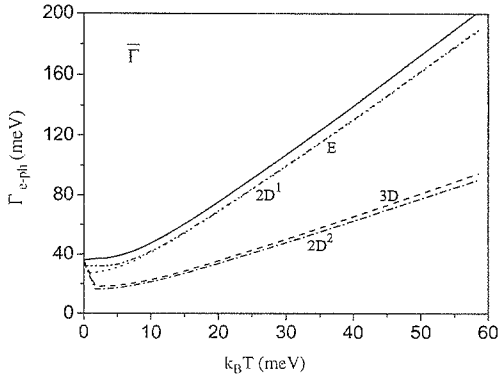

Figure 2.4 Example of the temperature dependence of the phonon-induced inverse lifetime, $\Gamma_{e-ph}(T)$, for the surface electronic state at the $\bar{\Gamma}$ point of the surface Brillouin zone of Al(001) (solid line). Also shown are $\Gamma_{e-ph}(T)$ in the Debye and Einstein models, the notations are the same as in Figure 2.3.

The linear dependence has often been used to extract the e–ph coupling parameter λ for electronic states with energies much larger than the maximum phonon energy. The method uses the temperature dependence of the linewidths of quasi-particle peaks measured in angle-resolved photoemission spectroscopy (ARPES). At temperatures much higher than the Debye temperature ($T \gg T_D$), this relation becomes linear and independent of the details of the phonon spectrum. Thus, if the Debye temperature T_D is not too high, λ can be deduced experimentally from the slope $\mathrm{d}\Gamma/\mathrm{d}T$ of the linewidth Γ plotted versus the temperature T [19]. In most other cases, the e–ph parameter can be obtained by fitting the experimental data with a simple model for the phonon density of states. This method with the assumption that the predominant contribution to the linewidth's temperature dependence can be attributed to e–ph coupling has widely been used to obtain λ for many surface electronic states except for those located close to E_F [16].

For a first estimate of the e–ph coupling and its contribution to the lifetime of excited electrons, the Debye and Einstein models are widely used to describe the phonon spectrum of a system. With the drastic simplification of a constant e–ph matrix element $g^{i,f}(\mathbf{k},\mathbf{q},\nu)$, one can obtain analytical expressions for both Eliashberg function and Γ_{e-ph} in terms of the e–ph coupling parameter and the characteristic Debye (Einstein) frequency ω_D (ω_E):

i) In the 3D Debye model for the bulk [19], $\alpha^2 F(\omega) = \lambda(\omega/\omega_D)^2$ for $\omega < \omega_D$ and zero otherwise. The lifetime broadening for $\omega < \omega_D$ is then given by

$$\Gamma_{e-ph} = \frac{2\pi\hbar\lambda\omega_D}{3}\left(\frac{\omega}{\omega_D}\right)^3 \tag{2.17}$$

and $\Gamma_{e-ph} = 2\pi\hbar\lambda\omega_D/3$ for $\omega \geq \omega_D$.

ii) In the 2D Debye model of a surface when only the first-order diagram is included, the Eliashberg spectral function $\alpha^2F(\omega) = \lambda(\omega/\omega_D)$ and

$$\Gamma_{e-ph} = \frac{\pi\hbar\lambda\omega_D}{2}\left(\frac{\omega}{\omega_D}\right)^2 \tag{2.18}$$

for $\omega < \omega_D$ and $\Gamma_{e-ph} = \pi\hbar\lambda\omega_D/2$ otherwise [19].

If both the first- and the second-order diagrams are included, the 2D Debye model yields

$$\alpha^2F(\omega) = (\lambda/\pi)\omega(\omega_D^2-\omega^2)^{-1/2},\ \omega < \omega_D, \tag{2.19}$$

$$\Gamma_{e-ph} = 2\hbar\lambda\omega_D\left(1-\sqrt{1-\left(\frac{\omega}{\omega_D}\right)^2}\right),\quad \omega < \omega_D \tag{2.20}$$

and $\alpha^2F(\omega) = 0$ and $\Gamma_{e-ph} = 2\hbar\lambda\omega_D$ for $\omega \geq \omega_D$.

Obviously, for $\omega < \omega_D$ both $\alpha^2F(\omega)$ and Γ_{e-ph} are linear functions of λ and scale with ω/ω_D.

iii) In the Einstein model, electrons interact only with a single-phonon mode with frequency ω_E. In this case,

$$\alpha^2F(\omega) = \frac{\lambda\omega_E}{2}\delta(\omega-\omega_E). \tag{2.21}$$

And one obtains $\Gamma_{e-ph} = \pi\hbar\lambda\omega_E$.

The corresponding Eliashberg spectral functions and the temperature behavior of Γ_{e-ph} in the Debye ($\omega_D = 34$ meV) and Einstein ($\omega_E = 20$ meV) models are shown for the surface electronic state at the $\bar{\Gamma}$ point of the Al(001) surface in Figures 2.3 and 2.4 by dashed and dotted lines.

2.2.4
Excitons: Electron–Hole Pairs in Semiconductor Quantum Wells

The discussion in this subsection deals with three kinds of quasi-particles: electrons, holes, and excitons. As our model, we take a semiconductor quantum well (QW), that is, a quasi-two-dimensional system where the charge carriers are free to move in a planar structure. Therefore, most of the concepts can also be used for the description of surface excitations.

The unexcited system is an insulator where all low-lying bands are fully occupied by electrons and the conduction-band states are free. The highest occupied band – the valence band – is separated by an energy gap from the lowest conduction band. Here, we focus on systems where this band gap is "direct", that is, the valence-band maximum and the conduction-band minimum (CBM) correspond to the same electron-momentum state, usually zero momentum, which is the center of the Brillouin zone (see Figure 2.5a).

Optical excitation of semiconductors in the spectral vicinity of the direct band gap causes electron transitions from the valence into the conduction band. Referring to

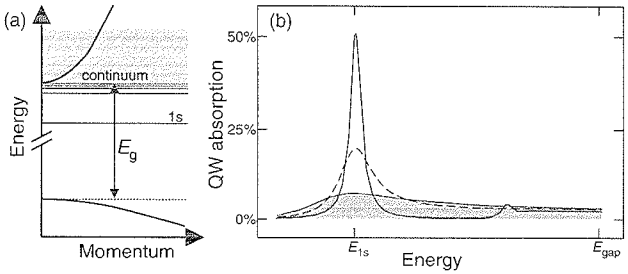

Figure 2.5 (a) Schematic conduction-band and valence-band structure showing energy versus in-plane carrier momentum. The horizontal lines mark the energies of the energetically lowest excitonic states. (b) Quantum well absorption spectra for increasing carrier densities, 10^9 cm^{-2} (solid line), 4×10^{10} cm^{-2} (dashed line), and 9×10^{10} cm^{-2} (gray solid line) assuming a temperature of 40 K.

the missing valence band electrons as "holes," we speak of optically-induced electron–hole pair transitions. The properties of the valence-band holes are those of the missing electrons, that is, they are Fermions and have a spin, charge, effective mass, and so on, which are opposite to that of the valence-band electrons. Since the electron charge is $-|e|$, where e is the elementary charge, the holes are positively charged and we have an attractive Coulomb interaction between the valence-band holes and the conduction-band electrons. (For more details and background information, see, for example, Refs [22–25] and work cited therein.)

Mathematically, the problem of a single electron–hole pair in parabolic bands is identical to that of the hydrogen atom, where the hole plays the role of the proton. In semiconductor physics, the corresponding Schrödinger equation is known as the Wannier equation, and the bound pair-state solutions are the (Wannier) excitons [26–30]. However, instead of the roughly 13.1 eV binding energy (Rydberg energy) in atomic hydrogen, the excitonic Rydberg is typically in the range of a few to 100 meV. This reduction in the pair-state binding energy is observed because the effective electron and hole masses are substantially lighter than the free electron and proton masses. Furthermore, the background dielectric constant reduces the Coulomb interaction strength roughly by one order of magnitude compared to hydrogen.

2.2.4.1 Microscopic Theory

For the model of a simple two-band system with a parabolic band structure, see Figure 2.5a, we have the standard many-body Hamiltonian

$$H = H_0 + H_C + H_I. \tag{2.22}$$

Here,

$$H_0 = \sum_{\mathbf{k}_\parallel} \varepsilon^c_{\mathbf{k}_\parallel} a^\dagger_{c,\mathbf{k}_\parallel} a_{c,\mathbf{k}_\parallel} + \sum_{\mathbf{k}_\parallel} \varepsilon^v_{\mathbf{k}_\parallel} a^\dagger_{v,\mathbf{k}_\parallel} a_{v,\mathbf{k}_\parallel} \tag{2.23}$$

is the single-particle part,

$$
\begin{aligned}
H_C = & \frac{1}{2}\sum_{\mathbf{k}_\parallel,\mathbf{k}'_\parallel,\mathbf{q}_\parallel\neq 0} V_{\mathbf{q}_\parallel}\, a^\dagger_{c,\mathbf{k}_\parallel+\mathbf{q}_\parallel} a^\dagger_{c,\mathbf{k}'_\parallel-\mathbf{q}_\parallel} a_{c,\mathbf{k}'_\parallel} a_{c,\mathbf{k}_\parallel} \\
& + \frac{1}{2}\sum_{\mathbf{k}_\parallel,\mathbf{k}'_\parallel,\mathbf{q}_\parallel\neq 0} V_{\mathbf{q}_\parallel}\, a^\dagger_{v,\mathbf{k}_\parallel+\mathbf{q}_\parallel} a^\dagger_{v,\mathbf{k}'_\parallel-\mathbf{q}_\parallel} a_{v,\mathbf{k}'_\parallel} a_{v,\mathbf{k}_\parallel} \\
& - \sum_{\mathbf{k}_\parallel,\mathbf{k}'_\parallel,\mathbf{q}_\parallel\neq 0} V_{\mathbf{q}_\parallel}\, a^\dagger_{c,\mathbf{k}_\parallel+\mathbf{q}_\parallel} a_{v,\mathbf{k}'_\parallel} a^\dagger_{v,\mathbf{k}'_\parallel-\mathbf{q}_\parallel} a_{c,\mathbf{k}_\parallel}
\end{aligned}
\tag{2.24}
$$

is the Coulomb interaction Hamiltonian, and

$$
H_I = -E(t)\sum_{\mathbf{k}_\parallel}\left(d^*_{cv} a^\dagger_{c,\mathbf{k}_\parallel} a_{v,\mathbf{k}_\parallel} + d_{cv} a^\dagger_{c,\mathbf{k}_\parallel} a_{v,\mathbf{k}_\parallel}\right) \tag{2.25}
$$

describes the interaction with a classical electromagnetic field. To account for the QW geometry, we have split all three-dimensional momentum vectors $\mathbf{k}$ into their components in z-direction and parallel to the plane of the QW,

$$
\mathbf{k} = (\mathbf{k}_\parallel, k_z). \tag{2.26}
$$

Furthermore, we introduced the creation and annihilation operators $(a^\dagger_{\lambda,\mathbf{k}_\parallel}, a_{\lambda,\mathbf{k}_\parallel})$ for the conduction ($\lambda = c$) and valence ($\lambda = v$) band electrons.

In Eq. (2.23), $\varepsilon^c_{\mathbf{k}_\parallel}$ ($\varepsilon^v_{\mathbf{k}_\parallel}$) denotes the single-particle energy of an electron in the conduction (valence) band with in-plane momentum $\mathbf{k}_\parallel$. In Eq. (2.24), the first two sums describe the repulsion among electrons in the same bands and the last term includes the interband attraction. Here, the Fourier transform of the Coulomb interaction potential is denoted by $V_{\mathbf{q}_\parallel}$ that incorporates the QW confinement. The system is coupled to the light field via the interband dipole matrix-element d_{cv} in Eq. (2.25), showing that the light field either creates or destroys pairs of electrons and holes (missing valence-band electrons).

To compute the semiclassical optical properties of a material system, we have to solve Maxwell's equations. Assuming a light field that propagates normal to the QW plane, we can write the wave equation for the one-dimensional propagation as

$$
\left[\frac{\partial^2}{\partial z^2} + \frac{n^2(z)}{c^2}\frac{\partial^2}{\partial t^2}\right] E = +\mu_0 \frac{\partial^2}{\partial t^2} P. \tag{2.27}
$$

Here, E is the electromagnetic field, z is the space coordinate normal to the surface of the QW, t denotes the time, and μ_0 is a constant prefactor depending on the system of units. The response of the material has been divided into a resonant part, treated dynamically in terms of the macroscopic optical polarization P, and the nonresonant part lumped into the (background) refractive index n.

We expand the optical polarization P into a Bloch basis [22]

$$
P = \sum_{\mathbf{k}_\parallel} d_{cv} P_{\mathbf{k}_\parallel} + \text{c.c.}, \tag{2.28}
$$

where $P_{\mathbf{k}_\parallel}$ is the microscopic polarization. The carrier occupation probabilities $f^{e,h}_{\mathbf{k}_\parallel}$ and the microscopic polarization $P_{\mathbf{k}_\parallel}$ constitute the diagonal and off-diagonal

elements of the reduced single-particle density matrix ϱ,

$$
\varrho = \begin{pmatrix} \langle a^\dagger_{c,\mathbf{k}_\parallel} a_{c,\mathbf{k}_\parallel}\rangle & \langle a^\dagger_{v,\mathbf{k}_\parallel} a_{c,\mathbf{k}_\parallel}\rangle \\ \langle a^\dagger_{c,\mathbf{k}_\parallel} a_{v,\mathbf{k}_\parallel}\rangle & \langle a_{v,\mathbf{k}_\parallel} a^\dagger_{v,\mathbf{k}_\parallel}\rangle \end{pmatrix} = \begin{pmatrix} f^e_{\mathbf{k}_\parallel} & P_{\mathbf{k}_\parallel} \\ P^*_{\mathbf{k}_\parallel} & f^h_{\mathbf{k}_\parallel} \end{pmatrix}. \tag{2.29}
$$

We calculate the equations of motion using the Heisenberg equation

$$
i\hbar\frac{\partial}{\partial t}\varrho = [\varrho, H]. \tag{2.30}
$$

Working out the commutators in Eq. (2.30), we obtain the semiconductor Bloch equations (SBE) [10, 22, 31]

$$
\begin{aligned}
\left[i\hbar\frac{\partial}{\partial t} - \varepsilon_{k_\parallel}(t)\right] P_{\mathbf{k}_\parallel}(t) &= -\left[1 - f^e_{\mathbf{k}_\parallel}(t) - f^h_{\mathbf{k}_\parallel}(t)\right]\Omega_{\mathbf{k}_\parallel}(t) + \Gamma^{v,c}_{\mathbf{k}_\parallel} \\
\frac{\partial}{\partial t} f^a_{\mathbf{k}_\parallel}(t) &= -\frac{2}{\hbar}\,\mathrm{Im}\left[\Omega_{\mathbf{k}_\parallel}(t) P^*_k(t)\right] + \Gamma^{c,c}_{\mathbf{k}_\parallel}
\end{aligned}
\tag{2.31}
$$

where the Hartree–Fock terms are shown explicitly and the contributions beyond Hartree–Fock are denoted by $\Gamma^{\lambda,\lambda'}_{\mathbf{k}_\parallel}$. In Eq. (2.31),

$$
\Omega_{\mathbf{k}_\parallel}(t) = d_{cv} E(t) + \sum_{\mathbf{k}'_\parallel\neq\mathbf{k}_\parallel} V_{|\mathbf{k}_\parallel-\mathbf{k}'_\parallel|}\, P_{\mathbf{k}'_\parallel}(t) \tag{2.32}
$$

is the renormalized field (Rabi energy) and

$$
\varepsilon_k(t) = \varepsilon^c_k - \varepsilon^v_k - \sum_{\mathbf{k}'_\parallel\neq\mathbf{k}_\parallel} V_{|\mathbf{k}_\parallel-\mathbf{k}'_\parallel|}\left[f^e_{\mathbf{k}'_\parallel}(t) + f^h_{\mathbf{k}'_\parallel}(t)\right] \tag{2.33}
$$

is the renormalized transition energy.

At the Hartree–Fock level, the SBE contain neither dephasing of the polarization nor screening of the interaction potential nor relaxation of the carrier distributions. To include these effects, we have to go beyond the Hartree–Fock approximation and specify the correlation contributions $\Gamma^{\lambda,\lambda'}_{\mathbf{k}_\parallel}$.

2.2.4.2 Excitonic Resonances and Populations

The linear optical response can be computed analytically. For an unexcited semiconductor system, that is, all polarizations and occupations vanish before the system is excited, we can linearize the polarization equation in the interaction with the external field. After a Fourier transform to real space, we obtain

$$
\left[i\hbar\frac{\partial}{\partial t} + \frac{\hbar^2\nabla^2_{\mathbf{r}_\parallel}}{2m_r} - V(\mathbf{r}_\parallel)\right] P(\mathbf{r}_\parallel, t) = -d_{cv}\, E(t)\, \delta(\mathbf{r}_\parallel), \tag{2.34}
$$

where m_r is the reduced electron–hole mass and $\mathbf{r}_\parallel$ is a position within the QW plane.

The homogeneous part of Eq. (2.34) leads to the Wannier equation

$$\left[\frac{\hbar^2\nabla^2_{\mathbf{r}_{||}}}{2m_r} - V(\mathbf{r}_{||})\right]\phi_\nu(\mathbf{r}_{||}) = E_\nu\phi_\nu(\mathbf{r}_{||}). \tag{2.35}$$

It is mathematically identical to the Schrödinger equation for the relative motion in the hydrogen problem. The solutions of the Wannier equation determine both the bound and the inonized exciton states. From the solution of the inhomogeneous Eq. (2.34), we obtain the electron–hole pair susceptibility, which yields the Elliott formula [28] for the linear semiconductor susceptibility

$$\chi(\omega) = 2|d_{cv}|^2 \sum_\lambda \frac{|\phi_\lambda(r=0)|^2}{E_\lambda - \hbar\omega - i\gamma}. \tag{2.36}$$

Here, we wrote only the resonant contribution and introduced γ as phenomenological background dephasing of the polarization. The Elliott formula shows that absorption resonances occur at the frequencies $\omega = E_\lambda/\hbar$. An example of such an excitonic spectrum is plotted in Figure 2.5b.

It is interesting to note that $\chi(\omega)$ displays excitonic resonances even though it describes the linear response of the system. In this limit, the analysis at the single-particle level, that is, the Hartree–Fock approximation, is exact. In fact, one can even find the many-body wave function [10] in the form of a Slater determinant. Hence, the appearance of excitonic resonances in the polarization and therefore in $\chi(\omega)$ cannot imply the presence of bound pair populations, that is, true excitons, since no populations are generated in the linear regime. One therefore refers to the polarization resonances either as "excitonic polarization" or as "coherent excitons." Here, each electronic excitation is in a superposition state between the valence and the conduction bands.

To describe true excitons as well as carrier screening, dephasing, or relaxation contributions, we must extend the theory beyond the Hartree–Fock level and derive equations for the correlations. Systematic and microscopically consistent approximations can be obtained by using the cluster expansion approach [10]. In general, the correlation terms $\Gamma^{\lambda,\lambda'}$ introduce microscopic couplings to the two-particle Coulomb and carrier–phonon correlations,

$$\Gamma^{\lambda,\lambda'}_{\mathbf{k}_{||}} \equiv \sum_{\nu,\mathbf{k}'_{||},\mathbf{q}_{||}\neq 0} V_{\mathbf{q}_{||}}\left[c^{\mathbf{q}_{||},\mathbf{k}'_{||},\mathbf{k}_{||}}_{\lambda,\nu;\nu,\lambda'} - \left(c^{\mathbf{q}_{||},\mathbf{k}'_{||},\mathbf{k}_{||}}_{\lambda',\nu;\nu,\lambda}\right)^*\right] + \Gamma^{\lambda,\lambda'}_{\mathbf{k}_{||},\text{phonon}}, \tag{2.37}$$

where we used the abbreviation

$$c^{\mathbf{q}_{||},\mathbf{k}'_{||},\mathbf{k}_{||}}_{\lambda,\nu;\nu',\lambda'} \equiv \Delta\left\langle a^\dagger_{\lambda,\mathbf{k}_{||}} a^\dagger_{\nu,\mathbf{k}'_{||}} a_{\nu',\mathbf{k}'_{||}+\mathbf{q}_{||}} a_{\lambda',\mathbf{k}_{||}-\mathbf{q}_{||}}\right\rangle. \tag{2.38}$$

True excitons follow from

$$c^{\mathbf{q}_{||},\mathbf{k}'_{||},\mathbf{k}_{||}}_{X} \equiv c^{\mathbf{q}_{||},\mathbf{k}'_{||},\mathbf{k}_{||}}_{c,\nu;c,\nu} = \Delta\left\langle a^\dagger_{c,\mathbf{k}_{||}} a^\dagger_{\nu,\mathbf{k}'_{||}} a_{c,\mathbf{k}'_{||}+\mathbf{q}_{||}} a_{\nu,\mathbf{k}_{||}-\mathbf{q}_{||}}\right\rangle \tag{2.39}$$

because it describes pair-wise correlations among different electrons and holes.

When the nonlinear absorption is studied, the presence of both coherent and true excitons as well as f^e, f^h, and $c_{\lambda,\nu;\nu',\lambda'}$ can significantly modify the probe response. All these contributions appear in the sources for the $\Gamma^{\lambda,\lambda'}_{\mathbf{k}_{||}}$ and $\Gamma^{\lambda,\lambda'}_{\mathbf{k}_{||},\text{phonon}}$ contributions in Eq. (2.37). As one effect, they introduce excitation-induced dephasing that yields spectral broadening of the absorption resonances due to many-body scattering among the excited charge carriers (see Figure 2.5b and Ref. [10] for more details).

To identify coherent and/or true excitons in an excited semiconductor QW, quantitative optical measurements under resonant excitation conditions have recently been performed [32]. For the analysis, the optical response was calculated for more than a 100 000 different electronic many-body states, including two-particle correlations. A detailed comparison between the quantitative experiments and the theory shows that the absorptive nonlinearities depend so sensitively on the many-body configuration that the role of coherent polarization, exciton, and electron–hole plasma contributions can be identified with great confidence.

For a fixed overall carrier density, Figure 2.6a demonstrates how the percentage of carriers bound into excitonic pairs modifies the absorption resonance of a weak probe beam. We see that the presence of true excitons is signified by a resonance narrowing because these excitons – as charge neutral particles – yield a reduced Coulomb scattering relative to the scattering from separate electrons and holes. In a case where the probed system already contains coherent excitons, there is the possibility to transfer energy between the excitonic and the probe polarization. This mechanism can yield significant excitonic gain, as shown in Figure 2.6b. The experimental verification of these effects is presented in Ref. [32].

2.2.4.3 Terahertz Spectroscopy of Exciton Populations

A well-established method to detect small concentrations of a particular species of atoms or molecules is to use an optical probe that is sensitive to transitions between the eigenstates of the respective species. If the characteristic absorption resonances are observed in the probe spectrum, the atoms or molecules must be present, and

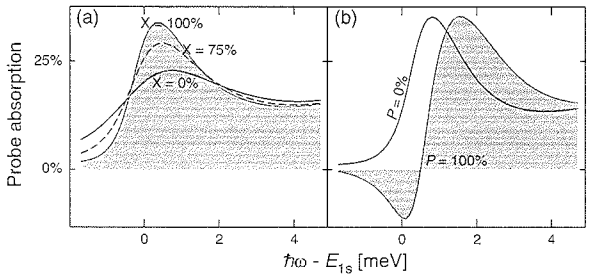

Figure 2.6 (a) Probe absorption spectra for a GaAs/AlGaAs semiconductor quantum well for the fixed carrier density (4×10^{10} cm^{-2}) and different exciton population fractions X. (b) Probe absorption spectra without (solid line) and with (shaded area) coherent excitons, assuming a constant carrier density of (3×10^{10} cm^{-2}).

through proper normalization of the respective oscillator strength one can deduce their relative concentration.

In order to apply this concept to the identification of excitonic populations in typical III–V or II–VI semiconductors, one needs terahertz (THz) fields since these can be resonant with transitions from the exciton's 1s to 2p state [33, 34]. The energy corresponding to the THz regime is way below the fundamental band gap of most direct-gap semiconductors. Hence, THz fields do not generate electron–hole interband excitations in those systems. Instead, they lead to intraband transitions, that is, to transitions between different many-body states.

If the system is in the completely incoherent, quasi-stationary regime, we can find an analytic expression for the linear THz susceptibility [10]. In that case, we obtain the THz susceptibility as

$$\chi_{\mathrm{THz}}(\omega) \propto \sum_{\lambda} (S_{\lambda}(\omega) - [S_{\lambda}(-\omega)]^{*}) N_{\lambda}^{\mathrm{ex}}, \tag{2.40}$$

$$S_{\lambda}(\omega) = \sum_{\beta} \frac{|D_{\lambda,\beta}|^2}{E_{\beta} - E_{\lambda} - \hbar\omega - i\kappa_{\lambda}}, \tag{2.41}$$

where the number of excitons in the state λ is defined as

$$N_{\lambda}^{\mathrm{ex}} = \sum_{\mathbf{q}_{||}} N_{\lambda}^{\mathrm{ex}}(\mathbf{q}_{||}) = \sum_{\mathbf{k}_{||},\mathbf{k}'_{||},\mathbf{q}_{||}} \phi_{\lambda}^{*}(k)\phi_{\lambda}(k') c_{X}^{\mathbf{q}_{||},\mathbf{k}'_{||},\mathbf{k}_{||}} \tag{2.42}$$

and $D_{\lambda,\beta}$ is the excitonic dipole matrix-element between the states λ and β. The form of Eq. (2.41) is typical of an atomic absorption spectrum when different atomic levels are populated according to $N_{\lambda}^{\mathrm{ex}}$.

Our theory shows that the THz response follows from the entire distributions since Eq. (2.42) contains a sum over all center-of-mass momenta $\mathbf{q}_{||}$. The THz absorption can therefore directly identify truly incoherent exciton populations in all center-of-mass momentum states, that is, both bright and dark excitons.

To illustrate the emergence of excitonic population signatures, we present in Figure 2.7 a series of computed THz absorption spectra for a situation where a short-pulse continuum excitation generates initially unbound electron–hole pairs. At the early times after the carrier generation, the THz spectrum in Figure 2.7a is very broad and has no resonances. This shape is characteristic of an electron–hole plasma. Figure 2.7b shows the development of a small peak around the excitonic $1s-2p$ transition energy. This peak grows into a pronounced resonance approximately 1 ns after the excitation, signifying the buildup of an incoherent exciton population. The asymetric shape of this resonance is a consequence of transitions between the lowest and all the energetically higher exciton states.

2.2.4.4 Excitonic Signatures in the Photoluminescence

In many situations, excitonic features can also be observed in the spontaneous emission, that is, the photoluminescence (PL) of a pre-excited system. Under incoherent conditions, the presence of an emission signal is a clear indication of radiatively decaying electron–hole pair populations. However, without a detailed microscopic

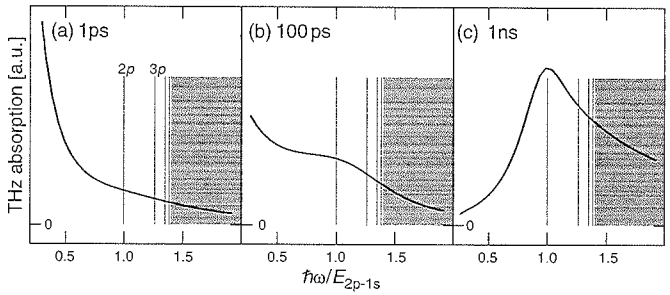

Figure 2.7 Computed THz absorption spectra for differnt delay times after the short-pulse interband excitation of a semiconductor quantum well. (a) The plasma-like spectrum after 1 ps, (b) a resonance develops around the energy corresponding to the intraexcitonic 1s-2p transition, and (c) pronounced excitonic resonance. The lines indicate the energies of the energetically higher excitonic states and the shaded area shows the ionization continuum.

analysis it is not obvious how much one can deduce about the state of the population, that is, about the possible presence of incoherent excitons and their distribution.

Since the process of light emission via spontaneous electron–hole recombination is an intrinsically quantum mechanical effect, we have to quantize the light field. For this purpose, we introduce bosonic creation and annihilation operators $B_{\mathbf{p}}^{\dagger}$ and $B_{\mathbf{p}}$ where the index $\mathbf{p}$ refers to a specific light mode with momentum $\mathbf{p}$ and energy $\hbar\omega_{\mathrm{p}} = \hbar c|\mathrm{p}|$.

Extending the semiclassical light–matter coupling Hamiltonian (2.25) into the full quantum optical regime, we can again derive an equation hierarchy that contains the quantum optical in addition to the Coulomb coupling effects already present in the SBE. The resulting equations yield the semiconductor luminescence equations (SLE) [10].

Under quasi-stationary weak excitation conditions, one can simplify the SLE to obtain an expression for the photoluminescence spectrum that is given as the steady-state photon flux,

$$I_{\mathrm{PL}}(\omega) \propto \mathrm{Im}\left[\sum_{\lambda} \frac{|\phi_{\lambda}(r=0)|^2 N_{\lambda}}{E_{\lambda} - \hbar\omega - i\delta_{\lambda}}\right], \tag{2.43}$$

where

$$N_{\lambda} = \sum_{\mathbf{k}_{||}} |\phi_{\lambda}(\mathbf{k}_{||})|^2 f_{\mathbf{k}_{||}}^{\mathrm{e}} f_{\mathbf{k}_{||}}^{\mathrm{h}} + N_{\lambda}^{\mathrm{ex}}\left(\mathbf{q}_{||} = 0\right). \tag{2.44}$$

We see that the carrier contributions are proportional to (i) the product of the electron and hole distributions and (ii) the optically active exciton population with center-of-mass momentum $\mathbf{q}_{||} = 0$, both of which contribute additively to the PL.

When we compare Eqs. (2.43) and (2.36), we note strong similarities. In particular, the frequency dependence of both equations is governed by the same denominator, giving rise to excitonic resonances. Hence, we see that the appearance of these resonances is independent of the detailed structure of the population factor. Since the

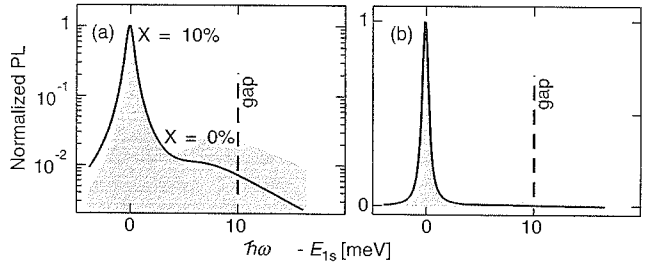

Figure 2.8 Photoluminescence spectrum for a situation without excitonic populations (X = 0%, shaded area) and for a situation where 10% of the electron–hole pairs are bound into excitons (solid line). The results are presented (a) on a logarithmic and (b) on a linear scale. The carrier density is 2×10^9 cm^{-2} and the system temperature is 20 K.

electron–hole plasma and exciton population terms appear additively in N_λ, both contributions can lead to luminescence and therefore also to emission at the excitonic resonances.

Figure 2.8 shows the computed luminescence for a situation without exciton population (gray shaded area) and a configuration where 10% of the electron–hole pairs are bound into excitons (solid line). Panels (a) and (b) present the same data on a logarithmic and linear scale, respectively. We see a prominent peak around the 1s exciton energy in all cases demonstrating the fact that the mere presence of this resonance does not signify excitonic populations in the system. However, the presence of true excitons modifies the ratio between the emission at the 1s resonance relative to the emission from the higher states, that is, 2s all the way to the continuum. A careful evaluation of this ratio makes it possible to determine the actual exciton population in the optically active states [35].

Altogether, we see that excitons and electron–hole pair excitations influence many aspects of the optical semiconductor properties. Excitonic signatures are also relevant in surface systems; see, for example, Ref. [36] and Section 2.4.3.4. In Ref. [37] the SBE have been applied to analyze these features in optical spectra; however, many more experimental and theoretical investigations on surface systems are needed before a comparable level of understanding can be achieved as in the low-dimensional semiconductor systems.

2.2.5
Polarons: Electron–Phonon Coupling in Polar and Ionic Solids

Conducting electrons in solids interact with phonons (quantized modes of vibration occurring in the crystal lattice). As a result of this interaction, a polarization of the lattice acts back on the electron that may be transformed into a quasi-particle called *polaron*, an electron accompanied by a cloud of phonons, that is, an electron coupled to phonons.

In the case of conduction bands of polar semiconductors and ionic solids that have their minimum at the Γ point and have an isotropic effective mass, and assuming that

phonons are dispersionless, the electron–phonon interaction can be described by the so-called Frohlich Hamiltonian [38]:

$$H = \frac{p^2}{2m} + \hbar\omega_0 \sum_{\mathbf{q}} a_{\mathbf{q}}^\dagger a_{\mathbf{q}} + H_{\text{el-ph}}, \tag{2.45}$$

where

$$H_{\text{el-ph}} = \sum_{\mathbf{q}} \left(M_{\mathbf{q}} a_{\mathbf{k}} e^{i\mathbf{k}\cdot\mathbf{r}} + M_{\mathbf{q}}^* a_{\mathbf{k}}^\dagger e^{-i\mathbf{k}\cdot\mathbf{r}} \right). \tag{2.46}$$

Here, $\mathbf{r}$ and $\mathbf{p}$ represent the conjugate coordinates of the electron (with mass m), $a_{\mathbf{q}}^\dagger$ ($a_{\mathbf{q}}$) are creation (annihilation) operators for a phonon with wave vector $\mathbf{q}$ and energy $\hbar\omega_0$, and $M_{\mathbf{q}}$ represents a coupling constant of the form

$$M_{\mathbf{q}}^2 = \frac{4\pi\alpha\hbar(\hbar\omega_0)^{3/2}}{V(2m)^{1/2}} \frac{1}{q^2}. \tag{2.47}$$

The q^{-2} dependence derives from the 3D Fourier transform of the (bare) Coulomb potential $\propto 1/r$ of the polar semiconductor or ionic crystal. V is a normalization volume and α represents the dimensionless polaron constant. For electrons that are linearly coupled to a system of optical phonons in a polar solid, one finds [39]

$$\alpha = \frac{e^2}{\hbar} \left(\frac{m}{2\hbar\omega_0} \right)^{1/2} \left(\frac{1}{\varepsilon_\infty} - \frac{1}{\varepsilon_0} \right), \tag{2.48}$$

where ε_∞ represents the optical high-frequency dielectric constant (the square of the refractive index) and ε_0 is the static dielectric constant (which includes optical, polar, and electron–electron contributions). Typical values of the Frohlich polaron constant of Eq. (2.48) are in the range 0.01–10 (see, for example, Ref. [40]).

A polaron is characterized mainly by its self-energy (the difference between the actual polaron energy and the energy of the corresponding uncoupled electron) and the effective mass. When the electron–phonon coupling is weak (α small), many-body perturbation theory can be used to find contributions to the polaron self-energy from Feynman diagrams containing one or more phonons. On the mass shell (i.e., by replacing the actual polaron energy by the energy of the corresponding uncoupled electron) and for zero momentum of the electron, one finds [41]

$$\Sigma = -\hbar\omega_0 \left[\alpha + 0.0159\alpha^2 + 0.008765\alpha^3 + O(\alpha^3) \right]. \tag{2.49}$$

For the effective mass, as obtained from an expansion of the polaron self-energy with respect to small momenta of the electron, one finds [41]

$$m^* = m\left[1 - 16\alpha + 0.02263\alpha^2 + O(\alpha^3)\right]. \tag{2.50}$$

When the electron–phonon coupling is strong (α large), one can follow the variational Gaussian wave function approach introduced by Landau and Pekar [42]. Alternatively, assuming that the electron is localized with a Gaussian wave function, the self-energy can be expanded as a power series in $1/\alpha$ to find [43]

$$\Sigma = -\hbar\omega_0\left[0.1085\alpha^2 + 2.836 + O(1/\alpha^2)\right]. \tag{2.51}$$

Feynman introduced a variational method based on path integrals, which has been found to be accurate for all values of the polaron coupling α [44]. A comparison between Eqs. (2.49) and (2.51) and between these equations and the Feynman calculations indicates that for the Frohlich Hamiltonian of Eqs. (2.45) and (2.46) the correct self-energy is given by the weak coupling result of Eq. (2.49) for values up to $\alpha \leq 5$ and by the strong coupling result of Eq. (2.51) for values $\alpha \geq 5$. Furthermore, a variational estimation of the actual size of the Gaussian wave function describing the electron leads to the conclusion that for $\alpha > 5$ or 6 polarons are expected to become localized within the size of the atomic unit shell, which is in contrast with the continuum Frohlich Hamiltonian of Eqs. (2.45) and (2.46) that assumes a continuum theory for the ions and a free particle motion for the unperturbed electron. These strongly localized polarons are the so-called small polarons. Small-polaron theories are based on the use of a Hamiltonian that includes the periodicity of the solid and the assumption that the size of the polaron corresponds to atomic dimensions (see, for example, Ref. [39]).

Electrons that are confined in two dimensions (2D), as occurs in the case of electrons at surface states or semiconductor heterostructures [45], also interact with phonons propagating along the 2D system. This coupling yields polarons in two dimensions, that is, 2D polarons, which can be described by a Frohlich Hamiltonian of the form of Eqs. (2.45) and (2.46) but with the electron–phonon coupling M_q of Eq. (2.47) replaced by [46]

$$\left(M_q^{2D}\right)^2 = \frac{2\pi\alpha^{2D}\hbar(\hbar\omega_0)^{3/2}}{A(2m)^{1/2}}\frac{1}{q}, \tag{2.52}$$

where A represents a normalization area. In particular, for image state electrons that are attracted to the surface of an ionic crystal by its image potential

$$V_{im}(z) = \frac{e^2}{4}\frac{\varepsilon_s - 1}{\varepsilon_s + 1}\frac{1}{z} \tag{2.53}$$

and are repeled from the interior of the solid, one finds the following value for the polaron coupling constant [46]:

$$\alpha^{2D} = \frac{e^2}{\hbar}\left(\frac{m}{2\hbar\omega_0}\right)^{1/2}(E_0 - E_\infty), \tag{2.54}$$

where $E_0 = (\varepsilon_0 - 1)/(\varepsilon_0 + 1)$ and $E_\infty = (\varepsilon_\infty - 1)/(\varepsilon_\infty + 1)$. In this case, image state electrons couple to surface phonons of energy $\hbar\omega_0$, with

$$\omega_0^2 = 12(\omega_L^2 + \omega_T^2), \tag{2.55}$$

where ω_L and ω_T are the frequencies of the bulk longitudinal and transverse phonons, respectively.

The self-energy and the effective mass of 2D polarons can be obtained from the Frohlich Hamiltonian of Eqs. (2.45) and (2.46) with the 2D electron–phonon coupling

of Eq. (2.52). In the weak coupling limit and for zero momentum of the electron, one finds the 2D polaron self-energy to be given by the following expression [47]:

$$\Sigma^{2D} = -\hbar\omega_0^{2D}\left[\frac{\pi}{2}\alpha^2 + 0.06397\alpha^2 + O(\alpha^3)\right]. \tag{2.56}$$

For the effective mass, one finds [48]

$$(m^*)^{2D} = m\left[1 + \frac{\pi}{8}\alpha + 0.1272348\alpha^2 + O(\alpha^3)\right]. \tag{2.57}$$

2.3 Collective Excitations

2.3.1 Plasmons: Electron Density Oscillations

In a pioneering study, Pines and Bohm [49] pointed out that the long-range nature of the Coulomb interaction between valence electrons in metals yields collective plasma oscillations similar to the classical electron density oscillations that had been observed by Tonks and Langmuir in electrical discharges in gases [50]. A simple classical model can be used in order to illustrate the collective nature of the motion of a free electron gas. Let us replace the positive ions by a uniform background of positive charge, and let us suppose that a charge imbalance is established in the plasma by displacing a slab of charge of thickness d by a small distance x ($x \ll d$) (see, for example, Ref. [51]). Hence, the slab behaves like a capacitor in which a constant electric field $\mathbf{E}$ is set up acting to restore charge neutrality. The magnitude of the field is simply

$$E = -4\pi n_0 e x, \tag{2.58}$$

since the surface charge density on either end of the condenser is simply $n_0 e x$, with n_0 being the unperturbed electron density. The equation of motion of an electron moving under the influence of this field is then

$$m\ddot{x} = -4\pi n_0 e^2 x, \tag{2.59}$$

with the result that electrons will undergo a simple harmonic oscillation at a frequency given by the following expression:

$$\omega_p = \left(\frac{4\pi n_0 e^2}{m}\right)^{1/2}. \tag{2.60}$$

Typical values of the density of valence electrons in metals are on the order of the Avogadro's number (more than 10 orders of magnitude larger than the density of electrons and positive charges in gaseous discharges). Hence, while in the case of gaseous plasmas the Fermi–Dirac distribution goes over to the Maxwell–Boltzmann distributions, quantum statistics must be employed for valence electrons in metals,

that is, the free electron gas at low (and room) temperatures and metallic densities can be regarded as a quantum plasma. The energy $\hbar\omega_p$ is the minimum value of the energy required to excite a simple harmonic oscillator of characteristic frequency ω_p, that is, a *plasmon*. Typical values of the plasmon energy ($\hbar\omega_p$) at metallic densities are in the range $2-20\,eV$. Plasmons are observed directly through energy losses in multiples of $\hbar\omega_p$ when electrons are fired through metallic films [52].

Plasma oscillations in a *uniform* free electron gas can also be described through the knowledge of a frequency-dependent dielectric function. Consider the electric and displacement fields of elementary electrostatics in the absence of external sources. They are known to satisfy the following equations:

$$\nabla \cdot \mathbf{D} = 0 \tag{2.61}$$

and

$$\nabla \cdot \mathbf{E} = 4\pi e\varrho, \tag{2.62}$$

where $\varrho(\mathbf{r}, t)$ represents a polarization charge density. At this point, we take the Fourier transform in space and time of Eqs. (2.61) and (2.62), we assume that the electronic response of the free electron gas is proportional to the applied field $\mathbf{D}$, that is,

$$\mathbf{E}(\mathbf{q}, \omega) = \frac{\mathbf{D}(\mathbf{q}, \omega)}{\varepsilon(\mathbf{q}, \omega)}, \tag{2.63}$$

where $\varepsilon(\mathbf{q}, \omega)$ is a frequency and wave vector-dependent dielectric function, and one finds

$$\varepsilon(\mathbf{q}, \omega)\, i\mathbf{q} \cdot \mathbf{E}(\mathbf{q}, \omega) = 0 \tag{2.64}$$

and

$$i\mathbf{q} \cdot \mathbf{E}(\mathbf{q}, \omega) = 4\pi e\varrho(\mathbf{q}, \omega). \tag{2.65}$$

One trivial solution of Eqs. (2.64) and (2.65) is

$$\mathbf{q} \cdot \mathbf{E}(\mathbf{q}, \omega) = \varrho(\mathbf{q}, \omega) = 0, \tag{2.66}$$

which corresponds to no net charge density or electric field present in the electron gas. However, for frequencies ω such that

$$\varepsilon(\mathbf{q}, \omega) = 0, \tag{2.67}$$

one may have a nonvanishing value of $\mathbf{E}(\mathbf{q}, \omega)$ and $\varrho(\mathbf{q}, \omega)$. This means that for frequencies such that the dielectric function $\varepsilon(\mathbf{q}, \omega)$ vanishes one has a free oscillation of the charge density with no external field. Hence, Eq. (2.67) represents the condition for the existence of plasma oscillations at frequency ω, which correspond to a net longitudinal electric field in the plasma.

In the limit of very long wavelengths ($\mathbf{q} \to 0$), the actual dielectric function of a *uniform* free electron gas coincides with the so-called Drude dielectric function (see, for example, Ref. [1]):

$$\varepsilon(0, \omega) = 1 - \frac{\omega_p^2}{\omega^2}, \tag{2.68}$$

with ω_p being given by Eq. (2.60). Hence, in the long-wavelength limit plasma oscillations exist at the frequency ω_p of Eq. (2.60), which was derived (see Eqs. (2.58)–(2.60)) in an approximation (neglecting altogether the random motion of the electrons) that is justified in the limit of very long-wavelength oscillations.

2.3.1.1 Surface Plasmons

In the presence of a boundary, there is a new collective oscillation (that propagates along the interface), which for a planar surface is the so-called surface plasmon predicted by Ritchie [53, 54]. Let us consider a classical model consisting of two semiinfinite nonmagnetic media with local (frequency-dependent) dielectric functions ε_1 and ε_2 separated by a planar interface at $z = 0$. The full set of Maxwell's equations in the absence of external sources can be expressed as follows [55]:

$$\nabla \times \mathbf{H}_i = \varepsilon_i \frac{1}{c}\frac{\partial}{\partial t}\mathbf{E}_i, \tag{2.69}$$

$$\nabla \times \mathbf{E}_i = -\frac{1}{c}\frac{\partial}{\partial t}\mathbf{H}_i, \tag{2.70}$$

$$\nabla\,(\varepsilon_i \mathbf{E}_i) = 0, \tag{2.71}$$

and

$$\nabla\,\mathbf{H}_i = 0, \tag{2.72}$$

where the index i describes the media: $i = 1$ at $z < 0$ and $i = 2$ at $z > 0$.

For an ideal surface, if waves are to be formed that propagate along the interface there must necessarily be a component of the electric field normal to the surface. Hence, one seeks conditions under which a traveling wave with the magnetic field $\mathbf{H}$ parallel to the interface may propagate along the surface ($z = 0$), with the fields tailing off into the positive ($z > 0$) and negative ($z < 0$) directions. From Eqs. (2.69)–(2.72), one finds the following system of equations:

$$\frac{\kappa_1}{\varepsilon_1} H_{1_y} + \frac{\kappa_2}{\varepsilon_2} H_{2_y} = 0 \tag{2.73}$$

and

$$H_{1_y} - H_{2_y} = 0, \tag{2.74}$$

which has a solution only if the determinant is zero, that is,

$$\frac{\varepsilon_1}{\kappa_1} + \frac{\varepsilon_2}{\kappa_2} = 0, \tag{2.75}$$

where

$$\kappa_i = \sqrt{q^2 - \varepsilon_i \frac{\omega^2}{c^2}}, \tag{2.76}$$

where q is the magnitude of a 2D wave vector in the plane of the surface. Equation (2.75) represents the condition for the existence of surface–plasmon polaritons. For a metal–dielectric interface with the dielectric characterized by ε_2, the solution $\omega(q)$ of Eq. (2.75) has slope equal to $c/\sqrt{\varepsilon_2}$ at point $q = 0$ and is a monotonic increasing function of q, which is always smaller than $cq/\sqrt{\varepsilon_2}$ and for large q is asymptotic to the value given by the solution of

$$\varepsilon_1 + \varepsilon_2 = 0. \tag{2.77}$$

This is the *nonretarded* surface plasmon condition (Eq. (2.75) with $\kappa_1 = \kappa_2 = q$), which is valid in the nonretarded regime in which the phase velocity ω/q is much smaller than the speed of light. In the case of a Drude semiinfinite metal in vacuum, with ε_1 given by Eq. (2.68) and $\varepsilon_2 = 1$, the nonretarded surface plasmon condition of Eq. (2.77) is fulfilled at the so-called surface plasmon frequency $\omega_s = \omega_p/\sqrt{2}$. For a recent review on surface plasmons and surface plasmon polaritons, see Ref. [12].

2.3.1.2 Acoustic Surface Plasmons

A variety of metal surfaces, such as Be(0001) and the (111) surfaces of the noble metals Cu, Ag, and Au, are known to support a partially occupied band of Shockley surface states within a wide energy gap around the Fermi level (see, for example, Ref. [56]). Since these states are strongly localized near the surface and disperse with momentum parallel to the surface, they form a quasi-2D surface state band with a 2D Fermi energy ε_F^{2D} equal to the surface state binding energy at $\bar{\Gamma}$ point.

In the absence of the 3D substrate, a Shockley surface state would support a 2D collective oscillation, the energy of the corresponding plasmon being given by [45]

$$\omega_{2D} = \left(\frac{2\pi n^{2D} e^2 q}{m}\right)^{1/2}, \tag{2.78}$$

with n^{2D} being the 2D density of occupied surface states, that is,

$$n^{2D} = \frac{\varepsilon_F^{2D} m}{\pi\hbar^2}. \tag{2.79}$$

Equation (2.78) shows that at very long wavelengths plasmons in a 2D electron gas have low energies; however, they do not affect electron–hole and phonon dynamics near the Fermi level, due to their square-root dependence on the wave vector. Much more effective than ordinary 2D plasmons in mediating, for example, superconductivity, would be the so-called acoustic plasmons with sound-like long-wavelength dispersion.

Recently, it has been shown that in the presence of the 3D substrate the dynamical screening at the surface provides a mechanism for the existence of a *new* acoustic collective mode, the so-called *acoustic surface plasmon*, whose energy exhibits a linear dependence on the 2D wave number [57–59]:

$$\omega_{\text{acoustic}} \sim v_F^{2D} q, \tag{2.80}$$

where v_F^{2D} represents the 2D Fermi velocity ($v_F^{2D} = \hbar\sqrt{2\pi n^{2D}}/m$). This *novel* surface plasmon mode has been observed at the (0001) surface of Be, showing a linear energy dispersion that is in very good agreement with Eq. (2.80) and first-principles calculations [60].

2.3.2 Magnons: Elementary Excitations in Ferromagnetic Materials

The notion of *spin waves* is one of the fundamental concepts in the physics of magnetism. In this section, we will focus on ferromagnetic systems. At low temperatures, the ferromagnetic system can be in good approximation considered as the gas of noninteracting bosonic quasi-particles, the so-called *magnons*, which are the quanta of the spin-wave excitations.

In modern applications, where the magnetization dynamics plays a very important role, the spin waves can be employed to transfer information between different parts of nanoscale devices. In most applications dealing with magnetization switching, it is crucial that the magnetic state disturbed by an external stimulus attenuates sufficiently fast to the equilibrium state. Therefore, the damping is an important aspect of spin dynamics. The spectrum of spin-wave excitations governs essentially the thermodynamics of ferromagnets. The interaction of magnons with other quasi-particles like electrons and phonons enriches the physics of condensed matter systems.

This section provides an introduction to the physics of spin waves and demonstrates how the concept of spin waves arises in different physical models. Moreover, we will present the results of the most recent studies of spin-wave dispersion and attenuation to acquaint the reader with current state-of-the-art investigations.

One can point out two limiting cases in the spin dynamics of ferromagnetic systems. One limit is represented by the *Heisenberg model*. Here, one supposes that the atoms in the condensed matter systems, similar to isolated atoms, can be characterized by the magnetic moments, which are well-defined atomic quantities. The energetics are governed by the effective interaction between the moments. The exchange parameters describe the energy associated with the relative change in the moments' directions. The values of the moments are constants of the model. Although the Heisenberg Hamiltonian can be justified under certain assumptions starting with the consideration of the Hamiltonian of interacting electrons, the electronic degrees of freedom are "integrated out" and do not enter the Hamiltonian.

The second limit consists in metallic (itinerant) magnets. One of the adequate approaches to study magnetic excitations in this case is the *linear-response density functional theory* [61]. This approach is based on the calculation of the transverse magnetic susceptibility within the parameter-free calculational scheme. The electron system enters these calculations through detailed information on the energies and wave functions of the electronic states.

The wave functions in metals are delocalized and the states are spread over the whole system. However, the real condensed matter systems are microscopically strongly nonuniform and the electronic states are, in general, very far from simple

plane waves. This is particularly true for the 3d electron states of the 3d transition atoms; they feature electronic density that is large within the atomic volumes and much lower in the interstitial regions between the atomic spheres. The large electron density leads to an increase in the exchange–correlation potential at corresponding points and results in strong magnetism of the itinerant electron system. It makes the spin polarization of the electron states energetically advantageous and leads to the nonzero magnetization of the system. The strong intraatomic exchange–correlation potential makes the introduction of the concept of atomic moments useful also in the case of itinerant electron systems. However, this quantity is by no means identical to the rigid atomic moment of the Heisenberg theory.

Next, we consider how spin waves appear in different physical models. We not only show the robustness of the concept of the spin wave with respect to the physical model but also demonstrate important differences between the two limiting descriptions outlined above.

2.3.2.1 Spin Waves in the Heisenberg Model

We begin with the Heisenberg model of classical atomic spins. The localized moment picture associates a spin moment S with each atom. The energetics of the magnet is described by the Heisenberg Hamiltonian

$$H = -\sum_{ij} J_{ij}\mathbf{S}_i \cdot \mathbf{S}_j, \tag{2.81}$$

where J_{ij} are the parameters of the effective interaction between the atomic moments of atoms i and j. A positive sign of the exchange parameters makes the parallel (ferromagnetic) orientation of the atomic moments the energetically preferable ground state.

The precessional dynamics of the atomic moments is described by the Landau–Lifshitz torque equation

$$\frac{\mathrm{d}\mathbf{S}_i}{\mathrm{d}t} = -\mathbf{S}_i \times \mathbf{h}_i \tag{2.82}$$

The effective field $\mathbf{h}_i$ acting on the moment of the ith atom is given by

$$\mathbf{h}_i = 2\sum_j J_{ij}\mathbf{S}_j. \tag{2.83}$$

By introducing Eq. (2.83) in the Landau–Lifshitz equation (2.81), we obtain the equation for the dynamic variables $\mathbf{S}_i(t)$. We will assume that the deviations of the atomic moments from the ground state's z-direction is small and will keep only terms of first order in the deviation angle. In this approximation, the z component of the spins remains equal to S and the dynamics of the x and y components is described by the equations

$$\frac{\mathrm{d}S_{ix}}{\mathrm{d}t} = -2S\sum_j J_{ij}(S_{iy} - S_{jy}) \tag{2.84}$$

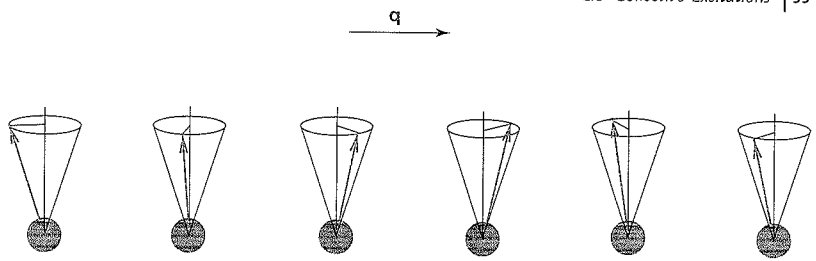

Figure 2.9 Schematic picture of the magnetic configuration corresponding to a spin wave with wave vector $\mathbf{q}$. (Please find a color version of this figure on the color plates.)

$$\frac{\mathrm{d}S_{iy}}{\mathrm{d}t} = 2S\sum_j J_{ij}(S_{ix} - S_{jx}) \tag{2.85}$$

We will look for the solution of Eqs. (2.84) and (2.85) in the form

$$\mathbf{S}_i(t) = S(\sin\theta\cos(\mathbf{qR}_i + \omega t),\ \sin\theta\sin(\mathbf{qR}_i + \omega t), \cos\theta), \tag{2.86}$$

where $\mathbf{R}_i$ is the position of atom i, $\mathbf{q}$ and ω are the wave vector and frequency of the spin wave, respectively, and angle θ gives the deviation of the atomic moments from the z-direction. This magnetic configuration is depicted in Figure 2.9. It is easily proven by direct substitution that expression (2.86) is in first order with respect to the angle θ, the solution of Eqs. (2.84) and (2.85) for the frequencies determined by

$$\omega_{\mathbf{q}} = 2S(J(0) - J(\mathbf{q})), \tag{2.87}$$

where

$$J(\mathbf{q}) = \sum_j J_{0j}\exp(i\mathbf{qR}_j). \tag{2.88}$$

Thus, we obtain spin-wave precessional eigenmodes, with their dispersion given by Eq. (2.87), as the solution of the Landau–Lifshitz equation for small deviations of the atomic spins from the ground-state directions.

It is instructive to evaluate the energy of the magnetic configuration (2.86) with respect to the ground-state energy. By substituting (2.86) in (2.81) and by assuming small values of θ, we obtain

$$\Delta E(\mathbf{q}, \omega) = \frac{\theta^2}{2} SN\omega_{\mathbf{q}}. \tag{2.89}$$

Since $(\theta^2/2)SN$ gives the reduction of the z-projection of the total spin moment, ΔS_z, Eq. (2.89) can be represented in the form

$$\Delta E(\mathbf{q}, \omega) = \Delta S_z\, \omega_{\mathbf{q}}. \tag{2.90}$$

Therefore, the increase in energy is proportional to the change in the total z-projection of S_z. The proportionality coefficient equals the precession frequency found in the solution of the Landau–Lifshitz equation. In other words, the frequency

of the spin wave precession equals exactly the energy of the spin wave configuration for a given momentum $\mathbf{q}$, which corresponds to the change in the z-projection of the total spin moment by 1.

If we recall that the spin is a quantum quantity and can only discreetly change its value by a minimal change equal to 1, $\omega_{\mathbf{q}}$ gives the energy of the lowest possible spin excitation for a given $\mathbf{q}$. This consideration leads to the quantization of the spin wave excitations.

Quantum Heisenberg Hamiltonian In the discussion above, we started with the Hamiltonian of the classical vectors and introduced the quantization of the spin waves in the last part of the treatment.

We obtained perfect agreement between the frequency of the eigen precession following from the Landau–Lifshitz equation and the energy consideration on the basis of Eq. (2.81). It is an important physical question how the properties of excited states will change if the atomic spins are from the beginning treated as quantum mechanical operators.

We consider now the quantum Heisenberg model

$$\hat{H} = -\sum_{ij} J_{ij}\hat{\mathbf{S}}_i\hat{\mathbf{S}}_j. \tag{2.91}$$

Here, $\hat{\mathbf{S}}_i$ is the operator of the spin of the ith atom. All atomic spins are characterized by the quantum number S. The spin states of the ith atom can be characterized by the value of the z-projection

$$\hat{S}_{iz}|S_z>_i = S_z|S_z>_i, \tag{2.92}$$

where $S_z = -S, -S+1, \ldots, S-1, S$ and $|S_z>_i$ is the corresponding eigenspinor of the ith atom.

It can be verified that

$$|0> \;=\; \prod_i |S>_i \tag{2.93}$$

is the lowest energy eigenstate of the operator (2.91) giving the ferromagnetic ground state of the quantum Heisenberg model

$$\hat{H}|0> = -\sum_{ij} J_{ij}S^2|0> . \tag{2.94}$$

The ground-state energy is

$$E_0 = -\sum_{ij} J_{ij}S^2 \tag{2.95}$$

On the basis of the experience gained in the previous section, we will assume that the excited spin wave states of the Hamiltonian (2.91) have the form

$$|\mathbf{q}> = \frac{1}{\sqrt{N}}\sum_i \exp(i\mathbf{q}\mathbf{R}_i)\frac{1}{\sqrt{(2S)}}\hat{S}_{i-}\,|0> \tag{2.96}$$

where operator $\hat{S}_{i-} = \hat{S}_{ix} - i\hat{S}_{iy}$ lowers the value of the z-projection of the spin of the ith atom by one:

$$\hat{S}_{i-}|S_z>_i = \sqrt{(S+S_z)(S+1-S_z)}\,|S_z-1>_i. \tag{2.97}$$

Since in the ground state $S_z = S$, we will need the last equation just for this value of S_z. Therefore, it simplifies to

$$\hat{S}_{i-}|S>_i = \sqrt{2S}\,|S-1>_i. \tag{2.98}$$

By acting with the Hamiltonian (2.91) on the spinor function $|\mathbf{q}>$ given by Eq. (2.96), we obtain

$$\hat{H}|\mathbf{q}> = (E_0+\omega_{\mathbf{q}})|\mathbf{q}> . \tag{2.99}$$

Therefore, $|\mathbf{q}>$ is indeed the eigenstate of the quantum Heisenberg Hamiltonian with the excitation energy $\omega_{\mathbf{q}}$ that corresponds exactly to the energy we obtained by considering the classical Heisenberg Hamiltonian.

By calculating the expectation values of the atomic spins for the state $|\mathbf{q}>$, we arrive again at the spin configuration shown in Figure 2.9.

Thus, we can conclude that the model of local atomic spins gives a robust picture of the spin wave excitations in a Heisenberg ferromagnet. Considering the precessional motion of the spins along with the energetics of the corresponding magnetic states gives exactly the same magnon energies as the eigenstate solutions of the corresponding quantum mechanical equations.

Despite the robustness of the localized moment picture, one should clearly understand its strong limitations in the description of real materials where the electronic states are delocalized over the whole system and the introduction of the atomic spins as dynamical variables is not straightforward. In the next section, we consider a consistent approach to the spin dynamics of itinerant electron systems referring to the similarities of both descriptions and their important differences.

2.3.2.2 Itinerant Electrons

An efficient and reliable approach to deal with magnetic properties of itinerant electron systems is offered by the framework of the density functional theory (DFT). The magnetic ground state is determined as the solution of a self-consistent Kohn–Sham problem where formally noninteracting electrons are placed in the potential that itself depends on the quantum mechanical states of the electrons given by the Kohn–Sham energies $\varepsilon_{n\mathbf{k}\sigma}$ and wave functions $\psi_{n\mathbf{k}\sigma}(\mathbf{r})$. Here, n is the number of electronic bands, $\mathbf{k}$ is the Bloch wave vector of the state, and σ is the spin projection.

We will discuss two different DFT-based approaches to the study of spin waves in itinerant electron magnets. First, we will very briefly introduce the frozen magnon method that basically maps the itinerant electron system on the classical Heisenberg Hamiltonian. Then, we will present in some details a more powerful method to investigate the magnetic excited states in itinerant magnets based on the calculation of the dynamic magnetic susceptibility.

Frozen Magnon Approach The so-called constrained calculations of the DFT [62] combined with the generalized Bloch theorem for spiral magnetic structures [8] allows for performing a direct DFT computation of the energy of the magnetic configurations shown in Figure 2.9. In elemental 3dferromagnets, the energy of these configurations directly provides an estimate of the magnon dispersion. This type of calculation gives reasonably good agreement with experimental spin wave energies for long-wavelength spin waves [63]. For systems with inequivalent magnetic atoms, the calculations become more involved since the deviations of the magnetic moments of inequivalent atoms in a spin wave excitation are different and *a priori* unknown. Therefore, there is no magnetic configuration of the type shown in Figure 2.9 that can be associated with spin waves in complex systems without evaluating the relative deviations between the moments of different atoms. However, also in this case the frozen magnon approach allows us to estimate the energies of the spin wave modes as described, for example, in Ref. [64].

This treatment is close to the consideration performed above, but with the Heisenberg-like exchange parameters determined in an *ab initio* calculation. Similar to the approaches based on the Heisenberg Hamiltonian the frozen magnon calculations are characterized by an infinite lifetime of the spin waves independent of the energy and wave vector of the excitation. In this respect, the calculations fail to capture the strong damping of the spin waves in metallic systems experimentally observed for wave vectors, which are off the Brillouin-zone center.

Calculation of the Dynamic Magnetic Susceptibility A consistent approach to study the spin waves in itinerant electron systems that takes full account of the electronic states is based on the calculation of the magnetic response of the system

$$\mathbf{m}(\mathbf{r},t) = \iint \mathrm{d}\mathbf{r}'\mathrm{d}t'\,\chi\,(\mathbf{r},\mathbf{r}',t-t')\,\mathbf{h}\,(\mathbf{r}',t') \tag{2.100}$$

to the transversal magnetic field

$$\mathbf{h}(\mathbf{r}) = h(\cos(\mathbf{q}\mathbf{r}+\omega t),\sin(\mathbf{q}\mathbf{r}+\omega t),0). \tag{2.101}$$

The presence of the spin wave eigenmodes with given $\mathbf{q}$ and ω leads to an enhancement of the susceptibility for just these parameters of the field. This allows us to identify the spin wave excitations.

The calculation of the dynamic magnetic susceptibility in the framework of the DFT consists of two steps. First, a nonself-consistent response of the itinerant electron system is calculated. It gives a noninteracting susceptibility, also called unenhanced or *Kohn–Sham susceptibility*.

$$\chi_{\mathrm{KS}}(\mathbf{r},\mathbf{r}') = \sum_{\mathbf{k}\Omega_{\mathrm{BZ}}}\sum_{nn'}\left(f^{\uparrow}_{n\mathbf{k}-\mathbf{q}}-f^{\downarrow}_{n'\mathbf{k}}\right) \times \frac{\psi^{\uparrow}_{n\mathbf{k}-\mathbf{q}}(l'\mathbf{r}')\psi^{\uparrow}_{n\mathbf{k}-\mathbf{q}}(l\mathbf{r})^{*}\psi^{\downarrow}_{n'\mathbf{k}}(l\mathbf{r})\psi^{\downarrow}_{n'\mathbf{k}}(l'\mathbf{r}')^{*}}{\omega-\left(\varepsilon^{\downarrow}_{n'\mathbf{k}}-\varepsilon^{\uparrow}_{n\mathbf{k}-\mathbf{q}}\right)+i0^{+}}, \tag{2.102}$$

where $\psi^{\sigma}_{n\mathbf{k}}$ stands for the Bloch state of band n, and $\varepsilon^{\sigma}_{n\mathbf{k}}$ is its Kohn–Sham energy. The response is determined by the available electronic transitions between the occupied ($f=1$) majority spin states ($\uparrow$), with crystal momentum $\mathbf{k}-\mathbf{q}$, and the empty ($f=0$) minority spin states ($\downarrow$) with momentum $\mathbf{k}$. These transitions are called the Stoner excitations. The momenta $\mathbf{k}$ belong to the Brillouin zone of the system.

According to the principles of DFT the induced magnetization results in an effective exchange–correlation field that adds to the external field. The problem requires a self-consistent solution: the magnetization induced by the sum of the external and exchange–correlation fields must produce the same exchange–correlation field. This leads to a collective response of all electronic states in the system and the emergence of spin waves.

The self-consistency condition is mathematically formulated in the form of the Dyson-like equation

$$\chi = \chi_{\mathrm{KS}} + \chi_{\mathrm{KS}} K_{\mathrm{xc}} \chi. \tag{2.103}$$

In concrete calculations, all quantities in Eq. (2.103) are presented by matrices in certain functional basis. The exchange–correlation kernel, K_{xc}, determines the effective Kohn–Sham potential. In the calculations discussed below, the form of

$$K_{\mathrm{xc}}(\mathbf{r}) \sim \frac{B_{\mathrm{xc}}(\mathbf{r})}{m(\mathbf{r})} \tag{2.104}$$

corresponds to the adiabatic local density approximation [61, 65]. In Eq. (2.104), $B_{\mathrm{xc}}(\mathbf{r})$ is the value of the exchange–correlation magnetic field at point $\mathbf{r}$ that is the difference of the spin-up and spin-down potentials at this point, and $m(\mathbf{r})$ is the magnetization.

The solution of Eq. (2.103) is the true *enhanced magnetic susceptibility*. It can be written in the following form:

$$\chi = (1-\chi_{\mathrm{KS}} K_{\mathrm{xc}})^{-1}\chi_{\mathrm{KS}}. \tag{2.105}$$

The spin waves appear as the peaks in the imaginary part of the susceptibility and signify strong absorption of energy by the system. The frequency corresponding to the maximum of the peak, $\omega_0(\mathbf{q})$, is identified as the magnon energy, whereas the full-width at half-maximum (FWHM) of the magnon peak is interpreted as the inverse lifetime Γ of the excitation. The finite lifetime of the spin waves is explained by their hybridization with the continuum of the single-electron Stoner excitations that enter the theory as poles of the Kohn–Sham susceptibility χ_{KS} (Eq. (2.102)). The Stoner transtion correspoding to a given momentum $\mathbf{q}$ and energy ω is schematically presented in Figure 2.10. This attenuation mechanism is commonly referred to as *Landau damping*. The calculations for the elemental ferromagnetic metals, in particular bcc Fe and fcc Ni, show that the decay becomes so strong that the spin wave excitation cannot be considered as well defined.

In the Heisenberg model, the number of spin wave modes is equal to the number of magnetic atoms in the unit cell. The spectral function presenting the energy distribution of the excited states takes in this case the form of a number of delta functions. In the itinerant electron systems, the situation is fundamentally different.

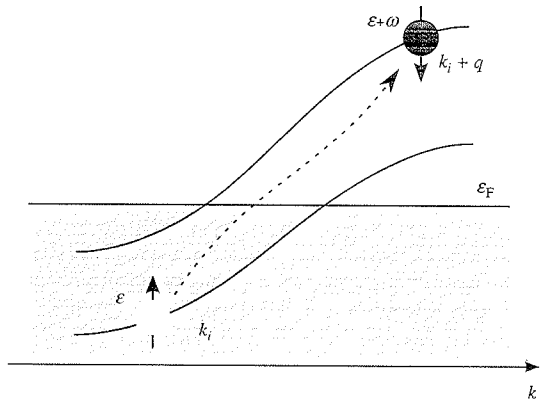

Figure 2.10 Schematic representation of the Stoner excitation. An electron is excited from an occupied majority spin state to an empty minority spin state. The states differ by energy ω and monetum **q**.

The energy position of a spin wave excitation is associated with the root of the real part of the denominator of Eq. (2.105)

$$\det\left(1-\mathrm{Re}\,\chi_{KS}K_{xc}\right)=0 \tag{2.106}$$

Since only the reactive (real) part of the unenhanced susceptibility enters the equation, it can be satisfied for the energy for which no Stoner transitions are available. In this case, the spin wave excitation is represented by a delta function peak in the spectral density of spin-flip excitations and has an infinite lifetime. In other words, the spin wave excitation appears as the eigenstate of the many-electron quantum mechanical problem.

However, if there also exist Stoner transitions at the energy associated with the spin wave state, the imaginary part of the Kohn–Sham susceptibility is nonzero. In this case, the delta function-like feature is replaced by a peak of finite width. The width is determined by the spectral density of the Stoner excitations in the corresponding energy region. This is the manifestation of the Landau damping. Depending on the wave vector and energy of the spin wave excitation, the influence of the Stoner transitions can vary from relatively weak to very strong. This scenario is confirmed by calculations performed for the 3d ferromagnets and by inelastic neutron scattering experiments. As an example, in Figure 2.11 we present the energies and lifetimes of magnons in bulk bcc iron based on the evaluation of the dynamic susceptibility and compare them with experimental neutron scattering data. Apart from the accurate prediction of magnon energies, the susceptibility reveals the experimentally observed sudden decrease in the magnon lifetime as the spin wave band enters the continuum of Stoner excitations.

An important physical question arises: are the spin wave excitations obtained by analyzing the dynamic susceptibility of itinerant electrons related to the precessional motion of the atomic moments in the Heisenberg model? The atomic moments do

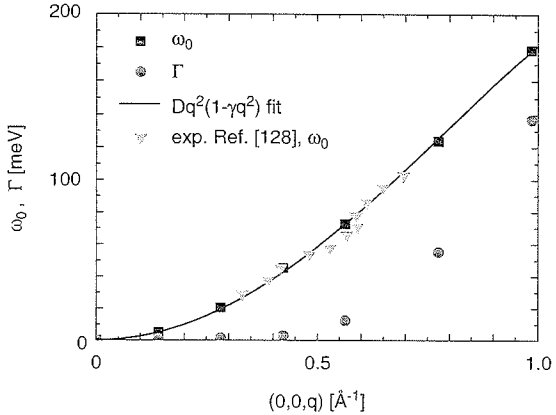

Figure 2.11 Energies (ω_0) and inverse lifetimes Γ of spin waves in bulk bcc Fe for wave vectors parallel to the (001)-direction of the reciprocal space.

not enter the calculation of the magnetic susceptibility directly. Instead, the system is physically described by the itinerant electron energies and wave functions. Nevertheless, the answer about the relevance of the atomic moments in the spin wave formation is positive also in this case. The reason for this is again the strong intraatomic exchange interaction mediated by the exchange–correlation kernel of the Dyson equation. The strong intraatomic exchange interaction has its origin in the strong spatial localization of the 3d states in the atomic spheres. The large electron density at a certain space point **r** results in a large exchange–correlation potential at this point and makes an alignment of the electron spins energetically preferable. Therefore, in the self-consistent precessional motion corresponding to spin waves, the electron spins in the intraatomic regions tend to order parallel to each other at each time instant. On the other hand, the Stoner transitions with the wave vector and energy equal to the wave vector and energy of the spin wave compete against the trend of preserving the atomic moment.

This competition between the formation of the spin wave as a precessional motion of well-defined atomic moments and the disturbance of atomic moments by single-electron Stoner excitations is the important mechanism for spin wave attenuation.

The question of the relevance of the atomic moments for the spin wave excitations in the itinerant electron systems is directly related to the question of the number of magnon modes in the excitation spectrum of the system. In the Heisenberg model, the number of modes is equal to the number of magnetic atoms in the unit cell. In the calculation of the dynamic susceptibility, the information about the system enters through the electronic band structure and, therefore, the number of the degrees of freedom is not restricted by the number of atoms. However, neither the experiment nor the calculations of the magnetic susceptibility detect an increase in the number of spin wave modes with respect to the Heisenberg model with the one exception of fcc-Ni where a number of investigations report the formation of a mode different

from the low-energy acoustic mode. Since the Ni spin moment per atom is the smallest from the 3d elements, it is expected to be less robust than the spin moments of Fe and Co, and the formation of a mode different from the Heisenberg one is most probable for nickel. The question of the presence of the "optical" mode in the spin wave spectrum of Ni is not solved (see, for example, Ref. [66]) and it will most probably remain the topic of detailed research work in the near future.

In systems with several different magnetic atoms in the unit cell, it is of strong interest to address the question whether the number of calculated magnon modes is equal to the number of atoms. Because of the complexity of the calculations of the dynamic susceptibility, there are only a small number of such studies for systems of this type. Here, we briefly consider a recent calculation by Buczek *et al.* [65] for the full Heusler alloy Co_2MnSi.

Because of the attenuation effects described above, peaks characterizing the individual spin wave modes are broadened. In the total susceptibility, these peaks can overlap and a broad common feature may arise that is difficult to analyze. Therefore, it is important to develop methods for the theoretical analysis that give access to individual spin wave modes. This approach is based on the diagonalization of the loss matrix and the analysis of the frequency dependence of its eigenvalues.

An example of the calculated loss tensor spectrum is presented in Figure 2.12, where three clear spin wave peaks can be discerned. The energies and inverse lifetimes of the spin waves along main directions in the Brillouin zone are presented in Figure 2.13a and b. The system has three magnetic atoms per unit cell and features three modes of the spin wave excitations. This shows that the concept of well-defined atomic moments remains useful also in the case of 3d compounds. The width of the lowest mode is zero, which is a consequence of the half-metallic character of the

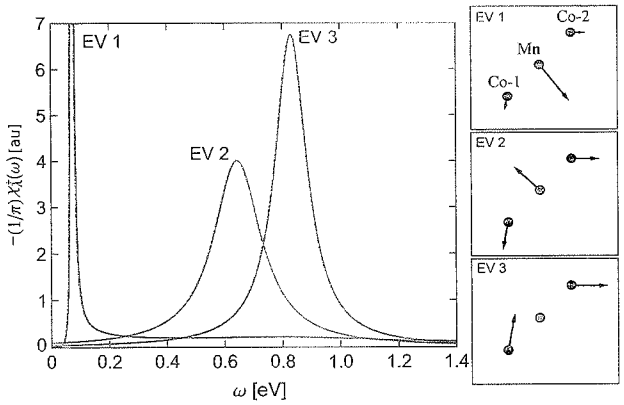

Figure 2.12 Enhanced susceptibility of Co_2MnSi, an example of the spectrum of the loss matrix for $\mathbf{q} = 0.28(1,1,0)2\pi/a$. a stands for the lattice constant. The three largest eigenvalues are shown, and other eigenvalues are of vanishing magnitude. Three clear peaks (EV 1, 2, and 3 corresponding to the labels in Figure 2.13) can be discerned. The panels show corresponding eigenvectors; arrows indicate the deviations of magnetic moments. Reprinted with permission from Ref. [65]. Copyright (2009) by the American Physical Society. (Please find a color version of this figure on the color plates.)

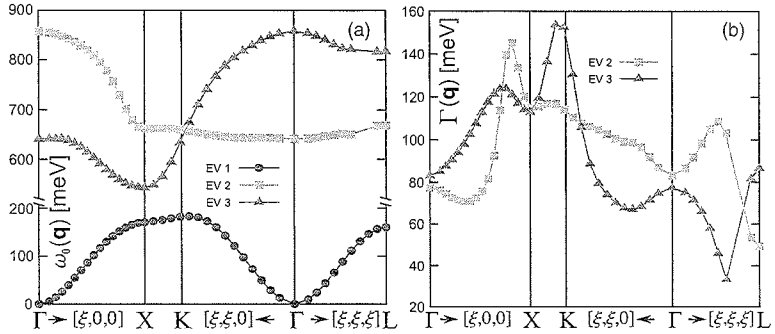

Figure 2.13 Energies (a) and inverse lifetimes Γ (b) of three SW modes in Co_2MnSi. Reprinted with permission from Ref. [65]. Copyright (2009) by the American Physical Society. (Please find a color version of this figure on the color plates.)

electron structure (cf. Figure 2.14). On the contrary, the "optical" modes (EV 2 and 3) appear where the continuum density is not small and have significant width, which depends strongly and nonmonotonously on $\mathbf{q}$. The shapes of the excitations corresponding to the three spin waves are characterized by an almost rigid rotation of the magnetization around the atomic sites and the number of spin wave modes corresponds to the number of magnetic atoms in the primitive unit cell. Therefore, Co_2MnSi – up to the damping – behaves as a typical Heisenberg–Hamiltonian system. In the EV 1 mode, the atomic moments oscillate in phase, roughly given by $e^{i\mathbf{q}\cdot\mathbf{r}_i}$, where $\mathbf{r}_i$ stands for the position of atom i. This justifies the use of the customary term "acoustic." For the optical modes, some of the moments align themselves roughly in the antiphase relation to the others, leading to quite intricate shapes of the excitations. As an example, let us consider the direction ΓK. The almost dispersionless mode EV 2 formed by Co and Mn moments (cf. Figure 2.12) can be regarded as an optical counterpart to EV 1, where Mn moments acquire an additional phase of π. Mode EV 3 involves only Co atoms.

Our last example is an iron film of three monolayer (ML) thickness. In Figure 2.15, we show the calculated spin-flip spectrum of the 3 ML Fe film on Cu(001). There are

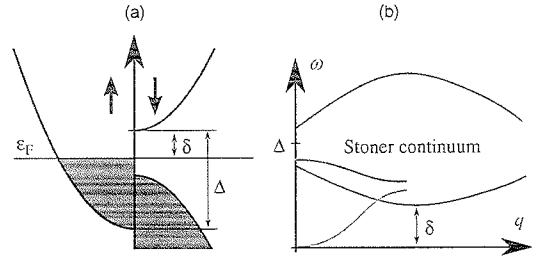

Figure 2.14 Schematic density of electronic states (a) and Stoner excitations (b) in a half metal. Because of the gap in the minority spin channel, there is a finite energy δ necessary to excite a Stoner pair. The energy in Co_2MnSi is on the order of 150 meV. Magnons with energies below this value cannot decay via the Landau mechanism.

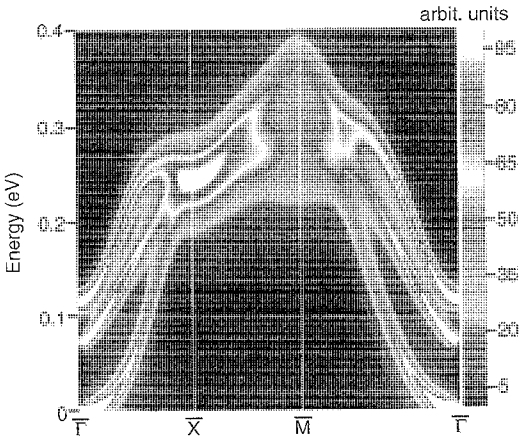

Figure 2.15 Spectral power $\mathrm{Im}\chi(q_{||}, \hbar\omega)$ of spin-flip excitations in three-monolayer iron film on Cu (100) obtained from LRDFT calculations. Reprinted with permission from Ref. [17]. Copyright (2010) by the American Physical Society. (Please find a color version of this figure on the color plates.)

three spin-wave branches: one acoustic branch starting with zero energy and two optical branches with activation energies around 0.1 eV. The characteristic form of the spectrum with the parabolic dispersion of acoustical magnons is a consequence of the exchange interactions in the film that are stronger within than between the atomic planes. Because of the nearly half-metallic character of the film, the number of Stoner states in the spin wave energy region is small and the magnon peaks are well defined. Time-resolved photoemission experiments, discussed in detail in Section 2.4.3.5, show that spin wave emission in this iron film constitutes a significant source of inelastic electron decay.

2.3.2.3 Conclusions

In this chapter, we have shown that in the ferromagnetic Heisenberg model of interacting atomic moments the spin waves can be derived as the eigenmodes of the precessional motion of the atomic moments or as eigenstates of the Heisenberg Hamiltonian. Both classical and quantum treatments give the same dispersion relation between the energy and the wave vector of the spin waves. Thus, the description on the basis of the atomic moment picture appears robust and transparent.

However, in the itinerant electron magnets the primary physical quantities are the energies and wave functions of the itinerant electron states. The consequent approach to the study of the magnetic excitations in itinerant electron systems is the evaluation of the dynamic magnetic susceptibility. We have shown that also in this case the concept of the well-defined atomic moments remains important for the interpretation of the results of the calculations. Although the atomic moments do not enter the theory as dynamic variables, the physical trend to their formation is present and originates from the strong intraatomic exchange–correlation potential.

A very important aspect of the study of the dynamic magnetic susceptibility is the account for the attenuation of the spin waves because of the hybridization with single-particle Stoner excitations. These excitations compete with the trend to the formation of robust atomic moments and lead to the finite lifetime of magnons.

2.4
Experimental Access to Quasi-Particle and Collective Excitations

2.4.1
Coherent Phonons

Electrons and holes exchange energy and momentum with the crystalline lattice by emitting or absorbing phonons (e–ph scattering), and so do phonons among themselves (ph–ph scattering). Phonons involved in these scattering events are *incoherent*. By contrast, illumination of a crystal with an ultrashort optical pulse can impulsively create *coherent* phonons, if the pulse duration is sufficiently short compared to the inverse phonon frequency. Like their incoherent counterpart, coherent phonons can be classified into the optical and acoustic branches.

2.4.1.1 Coherent Optical Phonons

Coherent optical phonons are in principle Raman active modes with wave vector $\mathbf{q} \simeq 0$, which are in phase over a macroscopic area illuminated by the laser pulse. They are observed as periodic modulations in the optical constants and other material properties at Raman phonon frequencies, typically in the THz (10^{12}–10^{13} Hz) range, as shown in Figure 2.16a for diamond.

Theoretical Description of Coherent Optical Phonons In most situations involving coherent optical phonons, a classical description is adequate. The classical equation of motion for a small nuclear displacement Q is that of a driven harmonic oscillator [68]

$$\mu\left[\frac{\partial^2 Q(t)}{\partial t^2} + 2\gamma\frac{\partial Q(t)}{\partial t} + \omega_0^2 Q(t)\right] = F(t), \tag{2.107}$$

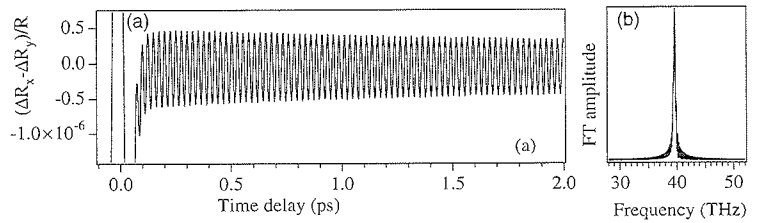

Figure 2.16 (a) Coherent optical phonon observed as a periodic modulation in the reflectivity of a diamond single crystal. (b) Fourier-transformed spectrum of the reflectivity trace in (a). The peak frequency is 39.8 THz (1330 cm^{-1}) See Ref. [67] for further details.

with the reduced lattice mass μ, the phonon damping γ, and the frequency ω_0. Solving the equation of motion gives the trajectory of a damped harmonic oscillator:

$$Q(t) = Q_0 \exp(-\gamma t) \sin(\omega_0 t - \varphi), \tag{2.108}$$

where φ is the initial phase. The trajectory deviates from the harmonic oscillator (2.108), for example, when the time-dependent interaction with photoexcited electron–hole plasma cannot be neglected [69–71].

While the classical model captures the essential physics, on a microscopic level the dynamics of the electrons and phonons should be described in terms of quantum mechanical operators. One way to microscopically describe coherent optical phonons is to do so with a synchronous motion of *many* different modes with locked phases. A finite optical penetration depth in an opaque solid would allow for a finite range of phonon wave vectors $\mathbf{q}$ to be coupled with the incident light and create a wave packet of optical phonons. This picture is convenient to describe coherent lattice oscillations in real space. Scholz *et al.* developed a microscopic theory for Ge [72], in which they wrote the Hamiltonian for electron–phonon coupling as a phonon-assisted hopping between lattice sites. The driving force of coherent phonons in Ge was given by the coherent part of the anisotropic hole hopping between the valence bands.

An alternative description of coherent optical phonons is given as a *single* zero-wave vector mode. This was achieved by Kuznetsov and Stanton [73] by considering deformational electron–phonon coupling, in which only the $\mathbf{q} = 0$ optical phonon mode is directly coupled to the total number of photoexcited electron–hole pairs. A simplified picture for a two-band semiconductor is given by a Hamiltonian

$$\hat{H}_{\mathrm{el}} = \sum_{\mathbf{k},\alpha} \varepsilon_{\alpha\mathbf{k}} c^{\dagger}_{\alpha\mathbf{k}} c_{\alpha\mathbf{k}} + \sum_{\mathbf{q}} \hbar\omega_{\mathbf{q}} b^{\dagger}_{\mathbf{q}} b_{\mathbf{q}} + \sum_{\alpha,\mathbf{k},\mathbf{q}} M_{\mathbf{kq}} \left(b_{\mathbf{q}} + b^{\dagger}_{-\mathbf{q}}\right) c^{\dagger}_{\alpha\mathbf{k}} c_{\alpha\mathbf{k}+\mathbf{q}}, \tag{2.109}$$

where $c, c^{\dagger}$ are the electron second quantization operators in k space, $\varepsilon_{\alpha\mathbf{k}}$ is the energy dispersion in the band $\alpha = \{c, v\}$ (conduction or valence), $\omega_{\mathbf{q}}$, $b^{\dagger}_{\mathbf{q}}$ and $b_{\mathbf{q}}$ are the phonon dispersion and the phonon creation and annihilation operators. The deformational coupling is described by the third term in the Hamiltonian. The coherent amplitude of the $\mathbf{q}$-th phonon mode is defined by the statistical averages of the *single* phonon operators

$$D_{\mathbf{q}} \equiv \langle b_{\mathbf{q}} \rangle + \langle b^{\dagger}_{-\mathbf{q}} \rangle \equiv B_{\mathbf{q}} + B^{*}_{-\mathbf{q}}, \tag{2.110}$$

so that it is proportional to the Fourier component of the displacement given by

$$\langle \hat{u}_{\mathbf{q}} \rangle \equiv \left\langle \frac{1}{V} \int d^3\mathbf{r} \hat{u}(\mathbf{r}) \mathrm{e}^{-i\mathbf{q}\cdot\mathbf{r}} \right\rangle = \sqrt{\frac{\hbar}{2\varrho V \omega_{\mathbf{q}}}} D_{\mathbf{q}}. \tag{2.111}$$

Here, ϱ is the reduced mass density and V is the system's volume. The averages in Eq. (2.110) will vanish when the phonon oscillator is in one of its energy eigenstates. In this case, there is a certain number, $\mathcal{N}_{\mathbf{q}} = \langle b^{\dagger}_{\mathbf{q}} b_{\mathbf{q}} \rangle$, of *incoherent* phonons in the

mode. However, if the wave function of the oscillator is a *coherent* superposition of different eigenstates, the displacement will not average to zero. An extreme case of such a superposition are *coherent states* that are widely used in quantum optics to describe quantum states of the electromagnetic field

$$\Psi^{\mathrm{coh}} = |z\rangle = \sum_{n} \frac{z^n}{\sqrt{n!}} \mathrm{e}^{-z^2/2} |n\rangle. \tag{2.112}$$

For these states, the "fully coherent" phonon amplitude and number can be defined by

$$B^{\mathrm{coh}}_{\mathbf{q}} \equiv \langle z | b_{\mathbf{q}} | z \rangle = z, \tag{2.113}$$

$$\mathcal{N}^{\mathrm{coh}}_{\mathbf{q}} = \langle z | b^{\dagger}_{\mathbf{q}} b_{\mathbf{q}} | z \rangle = |z|^2 = |B_{\mathbf{q}}|^2. \tag{2.114}$$

To have a nonzero amplitude in Eq. (2.110), however, the mode does not have to be in a fully coherent state. In the general case, a mode can have a certain number of both coherent and incoherent phonons

$$\mathcal{N}_{\mathbf{q}} = |B_{\mathbf{q}}|^2 + (\langle b^{\dagger}_{\mathbf{q}} b_{\mathbf{q}} \rangle - \langle b^{\dagger}_{\mathbf{q}} \rangle \langle b_{\mathbf{q}} \rangle) = \mathcal{N}^{\mathrm{coh}}_{\mathbf{q}} + \mathcal{N}^{\mathrm{incoh}}_{\mathbf{q}}. \tag{2.115}$$

The equation of motion for the coherent amplitude is obtained as

$$\frac{\partial^2}{\partial t^2} D_{\mathbf{q}} + \omega^2_{\mathbf{q}} D_{\mathbf{q}} = -2\omega_{\mathbf{q}} \sum_{\alpha,\mathbf{k}} M^{\alpha}_{\mathbf{kq}} n^{\alpha}_{\mathbf{k},\mathbf{k}+\mathbf{q}}, \tag{2.116}$$

where $n^{\alpha}_{\mathbf{k},\mathbf{k}+\mathbf{q}} \equiv \langle c^{\dagger}_{\alpha\mathbf{k}} c_{\alpha\mathbf{k}+\mathbf{q}} \rangle$ is the electronic density matrix, which is directly related to the photoexcited carrier density. Within this picture, the equations of motion for different modes are completely uncoupled. The coherence in the phonon system is the result of simultaneously occurring multiphonon processes within the same mode. For $\mathbf{q} = 0$ and assuming that the electron–phonon coupling constant M does not depend strongly on $\mathbf{k}$, Eq. (2.116) can be simplified to

$$\frac{\partial^2}{\partial t^2} D_0 + \omega^2_0 D_0 = 2\omega_0 \sqrt{\frac{\hbar}{2\omega_0 \varrho V}} [C^v - C^c] N(t) \equiv W N(t), \tag{2.117}$$

with C the deformation potential and N the total number of photoexcited electron–hole pairs. If the decay of N is neglected and N is approximated by a step function of time, Eq. (2.117) can be solved by Fourier transform in the limit $t \to +\infty$:

$$D_0(t) = \frac{W}{\omega^2_0} N_0 [1 - I(\omega_0) \cos \omega_0 t] \tag{2.118}$$

with the normalized pump intensity I. Assuming $\varrho = 5\ \mathrm{g/cm^3}$, $V = 1\ \mathrm{cm^3}$, $\omega_0 = 10$ THz, and $C^v - C^c = 10^9$ eV/cm, this would lead to the coherent lattice displacement of $\sim 3 \times 10^{-4}$ nm, which is 10^{-3} of a typical lattice constant and the number of coherent phonons $\mathcal{N}^{\mathrm{coh}}_0 = 10^{19}\ \mathrm{cm^{-3}}$, for excitation density of $10^{19}\ \mathrm{cm^{-3}}$. Incoherent emission

of $\mathbf{q} = 0$ phonons by photoexcited hot electrons is forbidden by energy and momentum conservation, and thus the quantum mechanical fluctuation of the lattice displacement,

$$\frac{\langle(\hat{u}-\langle u\rangle)^2\rangle}{\langle u\rangle^2} = \frac{2\mathcal{N}^{\text{incoh}}+1}{2\mathcal{N}} \simeq \frac{1}{2\mathcal{N}}, \tag{2.119}$$

is negligible. Therefore, as a result of the optical excitation, the $\mathbf{q} = 0$ phonon mode acquires a macroscopically large number of coherent phonons. The macroscopic occupation of a single $\mathbf{q} = 0$ quantum state would lead to an equivalent of Bose–Einstein condensation [70, 73].

The coherent states in Eq. (2.112) are a set of minimum-uncertainty states as noiseless as the vacuum state. Hu and Nori [74] proposed phonon squeezed states, in which the quantum noise is reduced below the zero-point fluctuation level, based on this single mode picture.

Generation of Coherent Optical Phonons The generation mechanism of the coherent optical phonons can be classified into two limiting cases according to the temporal profile of the driving force $F(t)$ in the equation of motion (2.107).

In transparent materials, impulsive stimulated Raman scattering (ISRS) is the only possible generation mechanism with a single pump pulse. A femtosecond, broadband optical pulse can offer multiple combinations of two photon difference frequencies required for the stimulated Raman process, $\hbar\omega_1 - \hbar\omega_2 = \hbar\omega_0$ (Figure 2.17a). This gives a δ function-like driving force defined by the Raman

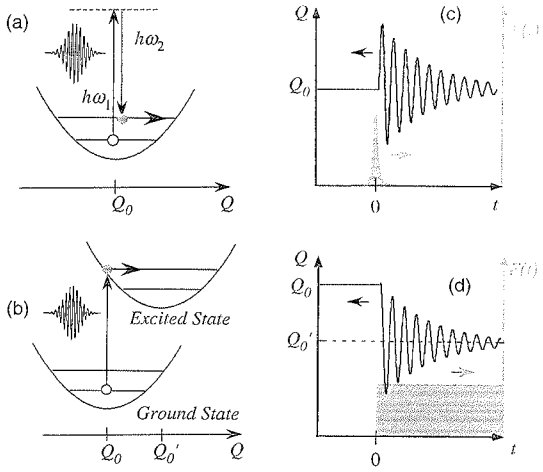

Figure 2.17 Schematic illustration of the two limiting cases for coherent optical phonon generation. (a) nonresonant ISRS. (b) DECP. Graphs (c) and (d) display the time evolution of the driving force (gray areas) and that of the displacement (solid curves) for nonresonant ISRS and DECP, respectively.

tensor R_{jkl} and the time profile of the excitation pulse [75, 76]:

$$F_j^{\text{ISRS}}(t) = R_{jkl}E_kE_l = \left(\frac{\partial\chi}{\partial Q}\right)_{kl} E_kE_l. \tag{2.120}$$

The resulting nuclear oscillation is a sine function of time (i.e., zero amplitude at $t = 0$), as illustrated in Figure 2.17c. In case of a resonant photoexcitation, ISRS can undergo an enhancement in the oscillation amplitude [77] and, for polar phonon modes, the breakdown of the Raman selection rule [78]. In the limit of a vanishing decay rate of the electronic excited state ($\Gamma \to 0$), the driving force can be given by a step function and should lead to an oscillation with a cosine function of time (i.e., maximum amplitude at $t = 0$) [77, 79], as illustrated in Figure 2.17d. For a finite value of Γ, the initial phase of the coherent optical phonons can vary between a sine and a cosine function of time [80].

When the electronic band structure is sensitive to the atomic motion of a particular phonon mode, photoexcition of carriers with ultrashort pulses can shift the vibrational potential surface suddenly and thus offer a step function-like driving force (Figure 2.17c). The resulting nuclear oscillation is a cosine function of time, as illustrated in Figure 2.17d. The displacive excitation of coherent phonons (DECP) was first proposed for the A_{1g} phonon of bismuth [81] and confirmed by a later time-resolved X-ray diffraction measurement [82] as well as a theoretical simulation [83].

At a semiconductor surface, the Fermi-level pinning by intrinsic or extrinsic surface states can lead to the formation of a depletion/accumulation layer. When such a surface is excited with ultrashort optical pulses, photogenerated electrons and holes are swept to opposite directions within 100 fs, as illustrated in Figure 2.18. The polarization buildup by such ultrafast drift-diffusion currents J can offer a step function-like driving force for *polar* phonons [68, 76]

$$F_j^{\text{TDFS}}(t) = -\frac{e^*}{\varepsilon_\infty\varepsilon_0}\int_{-\infty}^{t} \mathrm{d}t' J_j(t'), \tag{2.121}$$

where ε_∞ and ε_0 are the high frequency and the vacuum dielectric constants, respectively. The transient field screening in the depletion layer (transient depletion field screening, TDFS) dominates the generation of coherent LO phonons in III–V and II–V semiconductors, as well as in their heterostructures.

The generation mechanism cannot be determined solely from the initial phase of the coherent oscillation, because resonant ISRS, DECP and TDFS would all result in an oscillation with a cosine function of time. To distinguish the different generation mechanisms experimentally, the dependence of the coherent amplitude on the pump polarization angle, on the applied surface voltage, on the doping level, etc. should be examined carefully [84].

Detection of Coherent Optical Phonons With the recent development of ultrashort radiation and particle sources, a variety of detection techniques are available to investigate ultrafast dynamics of coherent optical phonons of different nature.

Linear optical detection, such as transient reflectivity and transmission measurements, have been the most conventional, standard experimental technique. In a first-order approximation, the coherent nuclear displacement Q induces a

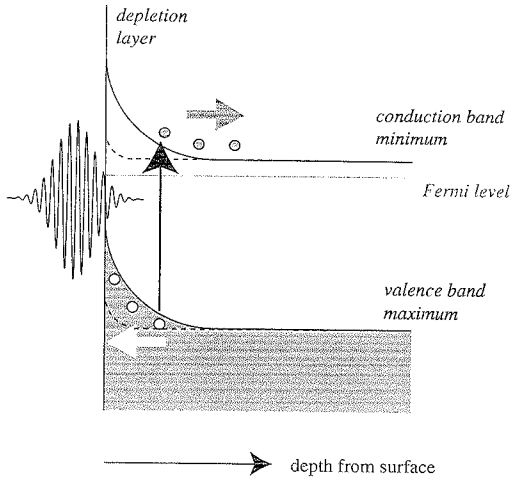

Figure 2.18 Schematic illustration of the TDFS in an n-type semiconductor. The band bending magnitude before and after photoexcitation is plotted by solid and broken curves, respectively. Because of the built-in depletion field, photoexcited holes are swept toward the surface and reach there the maximum density, whereas electrons are swept into the bulk. The ultrafast drift diffusion current screens the depletion field, and thus kick-starts coherent polar phonons.

change in the optical properties (e.g., reflectivity R) through the refractive index n and susceptibility χ [68]

$$\Delta R = \frac{\partial R}{\partial n}\Delta n \approx \frac{\partial R}{\partial \chi}\frac{\partial \chi}{\partial Q}Q(t), \tag{2.122}$$

which makes ΔR to be a quantitative measure for Q. Since $\partial\chi/\partial Q$ is a first-order Raman tensor, only Raman active modes can be observed by linear optical detection, provided that detection geometry and optical polarization satisfy the Raman selection rule. When the probe wavelength is at resonance with the optical absorption of the crystal, however, the breakdown of the Raman selection rule occurs. Dipole-forbidden Raman scatterings can then participate, in addition to allowed Raman scatterings, in the detection process of polar phonon modes [84]. The forbidden and allowed scatterings can be experimentally distinguished by the probe polarization dependence of the coherent amplitudes.

By using a nonlinear optical process such as second harmonic generation (SHG), one can probe coherent surface phonons and adsorbate-related vibrations exclusively [85, 86]. The second harmonic electric field is driven by the nonlinear polarization $P(2\omega)$ at the surface, which can be expanded into the nuclear displacement $Q_{n,q}$ for the n-th phonon mode with wave vector q [85]:

$$P_i(2\omega) = \left[\chi^{(2)}_{ijk}(2\omega) + \sum_{n,q}\left(\partial\chi^{(2)}_{ijk}(2\omega)/\partial Q_{n,q}\right)_0 Q_{n,q}\right] \times E_j(\omega)E_k(\omega). \tag{2.123}$$

The SH intensity is proportional to $|P|^2$ and can be approximated to be a linear function of Q by ignoring the second-order term.

Time-resolved X-ray diffraction (TRXRD) using a visible pump and X-ray probe scheme can directly monitor the structural dynamics of crystals far from the equilibrium. TRXRD can be applied for the detection of coherent optical phonons [87, 88]. However, in contrast to the TRXRD detection of acoustic phonons described in Section 2.4.1.2, the atomic motions associated with optical phonons do not modify the Bragg peak position because they do not change the barycentric positions of the crystal lattice. Instead, coherent optical phonons modify the Bragg peak intensity periodically if the structure factor can be approximated by a linear function of displacement in the vicinity of the equilibrium position [87].

In strongly correlated materials, the nuclear motion of particular phonon modes can couple strongly with the electronic system to affect the electronic conductivity in the THz frequency region. Time-resolved THz spectroscopy [89] can thus simultaneously monitor the coherent lattice and the coupled electron–hole dynamics. Time-resolved photoemission (TRPE) spectroscopy [90, 91] constitutes an alternative technique to detect the coupled phonon–electron dynamics as a periodic modulation in the binding energy of the electronic states.

Decay of Coherent Optical Phonons Coherent optical phonons decay via similar processes as incoherent phonons do, typically with a decay rate γ of 10^{10}–10^{11}s^{-1}. In good-quality crystals and at finite temperature, anharmonic coupling between normal modes provides the main decay path. The lowest order anhamonic term in the crystal potential is the third-order anharmonicity [92]. The corresponding phonon broadening $\gamma^{(3)}_A$ includes both the downconversion term, where the initial ω_0 phonon with wave vector $q \sim 0$ decays into two or more lower energy phonons, and the upconversion term, where the initial phonon is scattered by a thermal phonon into a higher energy phonon. If there is no phonon mode of higher frequency than ω_0, no upconversion mechanism is allowed, and the decay occurs only by the downconversion. Assuming that the high-energy phonon decays into two low-energy phonons such that $\omega_i(\mathbf{q}) + \omega_j(-\mathbf{q}) = \omega_0$, the linewidth can be written as

$$\gamma^{(3)}_A(\omega_0) = \sum_{ij}\gamma_{ij}(\omega_0)[1 + n(\omega_i) + n(\omega_j)]d_{\omega_i+\omega_j}(\omega_0), \tag{2.124}$$

where $n(\omega)$ is the phonon occupation number and γ_{ij} is the average coupling coefficient. The scattering efficiency is proportional to the density of states of the final two-phonon band $d_{\omega_i+\omega_j}(\omega_0)$, and therefore the decay channels involving zone edge phonons give the dominant contributions. Discrimination between the different allowed channels can be realized through their different behavior with temperature. For a high-frequency optical phonon decaying into two isoenergetic acoustic phonons ($\omega_i = \omega_j = \omega_0/2$), for example, the temperature dependence is given by [92, 93]

$$\gamma_A(T) = \gamma_0[1 + 2n(\omega_0/2)] = \gamma_0\left[1 + \frac{2}{\exp(\hbar\omega_0/2k_BT) - 1}\right]. \tag{2.125}$$

Crystalline defects, such as atoms with different isotopic masses and impurity atoms, also contribute to the decay of optical phonons at low temeprature and/or in defective crystals. The rate for the mass disorder-induced scattering γ_I is given by [94]

$$\gamma_I = g_2 \frac{\pi\omega_0^2}{12} N_d(\omega_0), \tag{2.126}$$

where $N_d(\Omega_0)$ is the phonon density of states, and

$$g_2 \equiv \sum_i x_i[\Delta M_i/\bar{M}]^2, \tag{2.127}$$

is a measure of the isotopic disorder, with x_i the concentration of the i-th isotope whose mass differs from the mean atomic mass $\bar{M}$ by the amount ΔM_i. Equation (2.126) can also be applied to describe scattering by single vacancies quantitatively by putting $\Delta M_i = \bar{M}$ and x_i to be the vacancy concentration [95].

In low-dimensional conducting systems, electron–phonon coupling can be the major decay channel for high-frequency optical phonons. For graphite, the decay rate of the E_{2g} mode (Raman G mode) can be computed by [96]

$$\gamma_g = \frac{\pi^2\omega_0\alpha'}{2c}\left[f\left(-\frac{\hbar\omega_0}{2}-\varepsilon_F\right)-f\left(\frac{\hbar\omega_0}{2}-\varepsilon_F\right)\right], \tag{2.128}$$

where c is the speed of light, f is the Fermi–Dirac distribution, and $\alpha' = 4.39 \times 10^{-3}$. Equation (2.128) implies that the shift of the Fermi level ε_F can lead to a *decrease* in the phonon decay rate through breakdown of the adiabatic approximation [96]. Such an anomalous decrease in γ_g can also be realized by the photoexcited nonequilibrium electronic distribution, that is, without affecting the charge neutrality, as was experimentally demonstrated in transient reflectivity measurements of coherent E_{2g} phonons of graphite [71]. Electron–phonon coupling can also dominate the phonon decay in three-dimensional crystals in the presence of an extremely nonequilibrium electronic distribution, leading to a Fano-type lineshape that is indicative of interference effects [97, 98].

Coherent Phonon-Quasiparticle Coupled Modes Like their incoherent counterparts, coherent optical phonons can couple with other quasiparticles and collective excitations in solids to form coherent coupled modes.

In polar semiconductors, LO phonons couple with the collective charge density oscillations to form LO phonon–plasmon coupled (LOPC) modes. The frequency of the LOPC modes can be obtained by solving the equation for the complex dielectric constant [99]

$$\varepsilon(\omega) = \varepsilon_\infty\left[1+\frac{\omega_{LO}^2-\omega_{TO}^2}{\omega_{TO}^2-i\gamma\omega-\omega^2}-\frac{\omega_p^2}{\omega^2+i\Gamma\omega}\right] = 0, \tag{2.129}$$

where ω_{LO} and ω_{TO} are the LO and TO phonon frequencies, γ and Γ, the phonon and plasmon damping rates, respectively. The plasma frequency $\omega_p = \sqrt{ne^2/m^*\varepsilon_0\varepsilon_\infty}$ depends on the carrier density n and the carrier effective mass m^*. For the LOPC

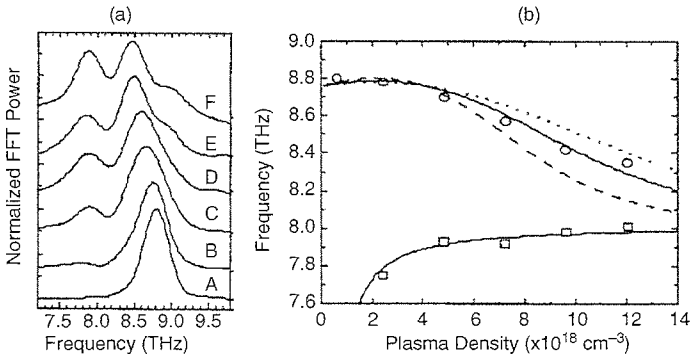

Figure 2.19 (a) Normalized Fourier power spectra for a TRSHG measurement on n-type GaAs. The pump-injected plasma densities are (A) 6×10^{17}, (B) 2.4×10^{18}, (C) 4.8×10^{18}, (D) 7.2×10^{18}, (E) 9.6×10^{18}, and (F) 1.2×10^{19}cm^{-3}. (b) Plot of the measured frequencies of the LO-hole (○) and LO-electron (□) coupling modes as a function of injected plasma density. Curves denote the calculated dielectric response function with different damping constants. Reprinted with permission from Ref. [102]. Copyright (2002), American Institute of Physics.

mode coupled with the *electron* plasma, the frequencies can be reproduced by the undamped ($\gamma = \Gamma_e = 0$) solutions, one of which appears above ω_{LO} (L^+ branch) and the other below ω_{TO} (L^- branch). Both branches of the LOPC mode were observed as coherent oscillations in transient reflectivity measurements on n-doped GaAs [100, 101]. Their frequencies were determined by the sum of doped and photo-injected carrier densities, indicating the coupling of the LO phonon with both the doped and the photo-injected electron plasma.

By contrast, a TRSHG study on similar n-doped GaAs [102] observed a coherent oscillation at a frequency between ω_{LO} and ω_{TO}, in addition to that below ω_{TO}, as shown in Figure 2.19. Because of the surface sensitivity, the SHG detection monitored the depletion layer of n-doped GaAs exclusively. The higher frequency oscillation was attributed to the LO phonon coupled with the photo-injected *hole* plasma, which was swept toward the surface due to the strong built-in field. The observed frequency was reproduced by Eq. (2.129) by assuming a heavy damping for the hole plasma ($\Gamma_h = 25$ THz). The lower frequency oscillation was likewise assigned to the LO phonon coupled with the photo-injected electron plasma, which has drifted toward the bulk.

Phonon–polaritons arise from the coupling of far infrared light to infrared-active phonons in crystals. They offer a good probe for the properties of low-frequency optical phonons, which are crucially related to the ferroelectric phase transition. Coherent phonon–polaritons [103] are generated in ferroelectrics such as $LiTaO_3$ and $LiNbO_3$ by four-wave mixing technique, which employs two pump pulses with wave vectors $\mathbf{k}_1$ and $\mathbf{k}_2$ crossing at the sample and thus creates a transient grating of phonons with wave vector $\mathbf{k}_p = \mathbf{k}_1 - \mathbf{k}_2 \neq 0$. By detecting the diffraction of the delayed probe light at the transient grating, one can monitor the coherent oscillation at the selected vector in the time domain. The light-phonon coupling leads to the formation of two polariton dispersion branches (polariton frequency ω_p as a function of

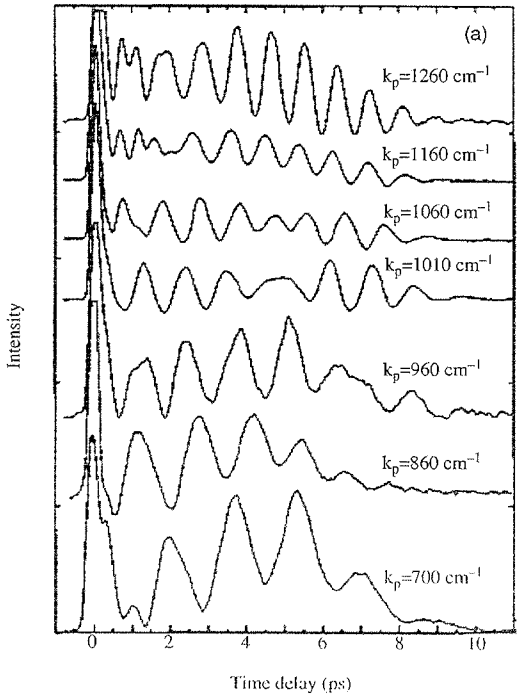

Figure 2.20 Phonon polaritons in $LiTaO_3$ at 300 K for different wave vectors. Reprinted with permission from Ref. [103]. Copyright (1998) by the American Physical Society.

polariton wave vector k_p) that avoid crossing at the resonance frequency. Time-resolved measurements on phonon-polaritons often show strong beating (polariton beats) in particular wave vector regimes, as shown for $LiTaO_3$ in Figure 2.20, due to the avoided crossings at the low-frequency resonances in the polariton dispersion.

In ferromagnetic metals, a coherent phonon–magnon coupled mode can be induced at the surface via spin-flip scattering. Transient reflectivity and TRSHG studies of the Gd(0001) surface observed such an coherently coupled oscillation in the presence of a magnetic field, whereas time-resolved photoemission measurements revealed that the same coherent vibration leads to a periodical shift of the surface-state energy via the exchange coupling between surface state and bulk bands [104].

2.4.1.2 Coherent Acoustic Phonons

Coherent acoustic phonons can be generated by the absorption of a laser pulse at a solid surface in the form of an ultrasonic wave packet with a spatial extent on the order of the penetration depth of the light. Uniaxial stress exceeding tens of MPa develops on a timescale much shorter than the acoustic propagation time across the laser penetration depth. As a result, the strain comprises a broad spectrum with frequencies extended from GHz up to a THz. The propagation of high-frequency (0.1–1 THz

range) acoustic phonons through crystals at low temperature is characterized by both ballistic and diffusive transport. Phonons can live long enough for multiple round-trips in a μm thick film, with typical periods of ns to μs depending on the crystal temperature.

Generation of Coherent Acoustic Phonons At semiconductor and metal surfaces, absorption of a laser pulse leads to an abrupt heating within the optical penetration depth through a variety of mechanisms including the volume deformation potential interaction, optical–phonon emission and subsequent decay, and Auger heating. Both the electron–hole plasma (through the deformation potential) and the heated lattice (through thermal expansion) contribute to a buildup of stress.

We consider a laser pulse of duration <1 ps and energy Q incident on the free surface of a film of thickness d [105]. The total energy deposited per unit volume at a distance z into the film is

$$W(z) = (1-R)\frac{Q}{A\varsigma}e^{-z/\varsigma}, \tag{2.130}$$

where R is the reflectivity, ς is the optical absorption depth ($\varsigma \ll d$), and A is the area illuminated by the light pulse ($\sqrt{A} \gg d, \varsigma$). This heating gives a temperature rise $\Delta T(z) = W(z)/C$, where C is the specific heat per unit volume. This sets up an isotropic thermal stress given by $-3B\beta\Delta T(z)$, where B is the bulk modulus and β is the linear expansion coefficient. The stress σ_{zz} is given by

$$\sigma_{zz}(z,t) = -3B\beta\Delta T(z,t) - B\frac{\partial E_g}{\partial P}\Delta n(z,t) + \varrho v^2 \eta_{zz}(z,t). \tag{2.131}$$

The second term represents the photoexcited electron–hole contribution to the stress, with Δn denoting the photoexcited carrier density, E_g is the band gap, and P is the pressure. The last term is the elastic response of the crystal, with ϱ denoting the mass density, v the longitudinal speed of sound, and η_{zz} the resultant strain. The stress and strain are related to the atomic displacement u_z by

$$\frac{\partial \sigma_{zz}}{\partial z} = \varrho \frac{\partial^2 u_z}{\partial t^2}, \tag{2.132}$$

$$\eta_{zz} = \frac{\partial u_z}{\partial z}. \tag{2.133}$$

The strain $\eta_{zz}(z,t)$ obtained by solving these equations is shown in Figure 2.21a. The solution contains two separate components: a static thermal layer proportional to the instantaneous stress and a bipolar coherent acoustic pulse that travels away from the surface at the speed of sound. The width of this pulse is on the order of twice the absorption length ς. After propagating across the film, the pulse will be reflected at the boundary with the substrate. The acoustic pulse is detected after each round trip in the film as a series of equally spaced pulses, as shown in the right panel of 21.

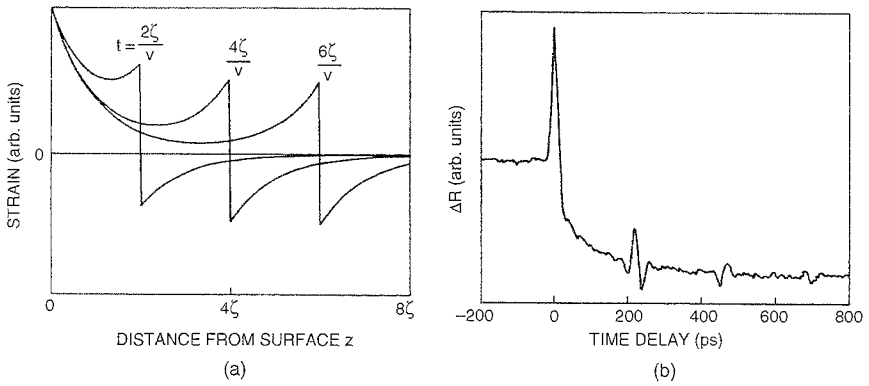

Figure 2.21 (a) Calculated spatial dependence of the elastic strain at different times after the pump pulse has been absorbed. (b) Photoinduced changes in reflectivity of a 2200 Å film of As_2Te_3 on a sapphire substrate. Reprinted with permission from Ref. [105]. Copyright (1986) by the American Physical Society.

The successive echoes in Figure 2.21(b) are inverted with respect to each other. This is consistent with the boundary conditions at the two surfaces of the film: at the free surface the phase changes by π and at the substrate interface there is no phase change because of the higher acoustic impedance of sapphire.

In semiconductor superlattices, the bulk phonon dispersion is backfolded into the mini-Brillouin zone of the artificially periodic heterostructure. The zone folding results in a series of Raman active acoustic phonon branches with $\omega \neq 0$ at wave vectors $q \simeq 0$ [106]. For this reason, the generation of coherent zone-folded acoustic phonons in superlattices is dubbed as ISRS [68, 76], which was described in Section 2.4.1.1.

In transparent materials, the generation and detection of coherent acoustic phonons is based on impulsive stimulated Brillouin scattering (ISBS) in a transient grating scheme [107]. ISBS utilizes two crossing laser pulses to generate counterpropagating acoustic phonons of selected wave vectors through photoelastic effects. The third light pulse, a probe, is diffracted by the interference fringe and detected by a photodetector. The intensity of the diffracted light oscillates according to the propagation of the acoustic phonons that exist as a standing wave.

Detection of Coherent Acoustic Phonons The time-resolved detection of coherent acoustic phonons in transparent solids has been based on the ISBS technique described above [107].

For opaque crystals at low temperature (<10 K), detection of the heat pulse with a bolometer has been a standard technique for relatively slow (> ns) timescales. By spatially scanning the exciting laser spot with respect to the detector, one can visualize the highly anisotropic transport of the acoustic wave (phonon imaging) [108]. With an intense fs laser as a light source, pump–probe optical detections such as transient reflectivity measurements can achieve much faster time resolution, which is required for a very thin film or nanostructured sample, without cooling. Scanning the probe

pulse with respect to the pump pulse on a thin film enables to image the snapshots of surface acoustic wave fronts propagating laterally like ripples [109].

TRXRD in a visible pump and X-ray probe scheme can directly monitor the coherent acoustic phonon dynamics [88, 110]. Acoustic phonons excited by an intense femtosecond laser pulse modulate the translational periodicity of a crystal, which is probed with an X-ray pulse by recording the rocking curve (X-ray reflectivity as a function of incident angle) at different time delays [88, 110]. Time-resolved electron diffraction (TRED) offers a highly surface sensitive technique to monitor coherent acoustic phonons as a periodic shift in the Bragg peak position [111].

Decay of Coherent Acoustic Phonons Mass defect scattering by impurities or isotopes [112] and anharmonic decay [113, 114], together with phonon focusing effects [108], dominate the dynamics of high-frequency phonon transport in nonmetallic solids. In metals, interaction with photoexcited nonequilibrium electrons has also to be taken into account [115].

In high-quality crystals at low temperature (<10 K), scattering occurs mainly at mass defects, which typically are impurities and naturally occurring isotopes. Tamura [112] demonstrated that the scattering rate of acoustic phonons by substitutional isotopic atoms in a Bravais lattice can be written as

$$\gamma_I(\omega) = \frac{\pi}{6} V_0 g_2 \omega^2 D(\omega), \tag{2.134}$$

where V_0 is the volume per atom, D is the phonon density of states per unit volume, and g_2 is a measure of the isotopic disorder given by Eq. (2.127). Equation (2.134) implies that the scattering rate depends only on the frequency of the initial phonon, not its wave vector or polarization. In the long-wavelength limit ($\omega \ll \omega_D$), Eq. (2.134) reduces to [116]

$$\gamma_I = \frac{V_0 g_2 \omega^4}{4\pi v_D^3}, \tag{2.135}$$

with v_D the Debye velocity, which exhibits a ω^4 dependence. For scattering of phonons in the high-frequency dispersive region, a stronger frequency dependence than ω^4 is expected [112].

At finite temperature, anharmonic coupling, in which the initial high-frequency phonon decays spontaneously into two or more lower-frequency phonons, is also important. As the phonons downconvert by spontaneous decay, their mean free path increases dramatically. The anharmonic decay rate of acoustic phonons cannot be expressed in a simple way but varies with propagation direction and phonon polarization [116]. In the regime $\omega \gg k_B T/\hbar$, the lifetime of LA phonons against anharmonic three-phonon processes is very short, whereas TA phonons have anomalously long lifetime. This is because the TA phonons cannot decay spontaneously except through the collinear processes [85]. By contrast, the LA phonons can split spontaneously into two phonons, whose decay rate is be proportional to ω^5 from in weakly dispersive, isotropic crystals [67, 81]. For strongly dispersive, anisotropic crystals, however, the spontaneous decay rate exhibits a stronger frequency dependence

than ω^5 [83]. Calculations indicate that the dominant decay channel for cubic crystals is LA $\rightarrow$ TA + TA, and total dacay rates at 1 THz is from 10^5 to 10^6 s^{-1} [113].

2.4.2
High-Resolution Angle-Resolved Photoemission

2.4.2.1 Photoemission Spectral Function of Quasi-Particles

The formation of quasi-particles in a many-body solid can conveniently be accessed by angle-resolved photoelectron spectroscopy. In the previous section, it has been addressed how quasi-particles can form by means of interaction between electrons on the one hand and excitations, such as, for example, phonons on the other hand. In now turning to photoemission, which probes the occupied states of the solid, one may naively think that it provides an account of the electronic band structure of the solid. However, there is a fundamental caveat: conventional band theory traditionally only accounts for the interaction of electrons with the static ion lattice. Yet, coupling to further microscopic degrees of freedom can alter the electron dynamics and lead to new many-body ground states not foreseen in that picture. A prominent example is the interaction with lattice vibrations (phonons) [19] that enhances the effective electron mass on the corresponding energy scale. A possible consequence is that it may give rise to (conventional) superconductivity. Moreover, the impact on the electrons from interaction with other excitations such as spin excitations in magnetic materials should also exist, yet it is not nearly as well established. This problem has received new attention due to the suggestion that high-temperature superconductivity in cuprate materials may result from electronic coupling to spin fluctuations [117]. Yet another mechanism, which is a notorious problem even for "simple" band structure calculations in an effective one-electron picture, is the existence of electron–electron correlations, which are – per definition – not treated exactly in standard approaches such as density functional theory. Therefore, by exploiting ARPES as an experimental probe, one must expect to get an account of all these interactions simultaneously. Let us consider what will happen (and which corrections will apply) to the picture of noninteracting electrons. Most importantly, interaction of conduction electrons with elementary excitations leads to a *renormalization* of electronic energies, that is, to deviations of their band dispersion from that expected for the noninteracting case. At low binding energies, the electrons become dressed by excitations, thereby forming dressed *quasi-particles* of increased mass (note that here the term "quasi-particle" will be used in conjunction with dressing by bosonic excitations, while strictly the concept of quasi-particles can be applied to all electron states in a many-body electron system [1]). As illustrated in Figure 2.22a, this is reflected in a reduced slope of the electron band which is inversely proportional to the electron mass. Beyond the characteristic energy scale ω_0 of the coupled excitations, the electrons resume their noncoupling band dispersion. Quasi-particle formation due to interaction with phonons as depicted in Figure 2.22b has been reported experimentally by ARPES, and we shall examine examples below [118, 119].

The analogy to electron–phonon coupling would be the coupling to spin waves (magnons) illustrated in Figure 2.22c. The highest spin wave mode to which the

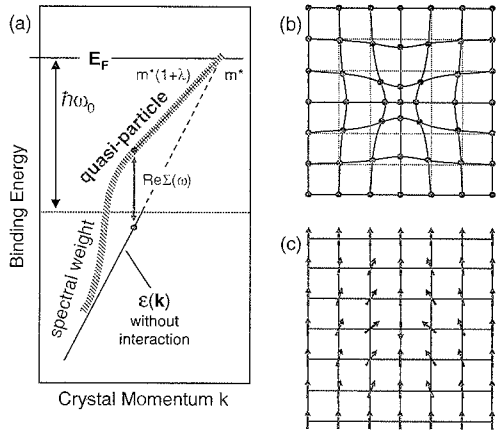

Figure 2.22 Schematic display of quasi-particle formation. (a) The electron is dressed with the excitation (phonon or spin excitation) up to an energy ω_0 below the Fermi energy, leading to a mass enhancement. (b) Electron–phonon coupling implies a distortion of the crystal lattice surrounding the electron. (c) Electron–magnon coupling implies spin scattering mediated by magnetic interactions. (Please find a color version of this figure on the color plates.)

electrons couple accordingly defines the energy ω_0. Unfortunately, similar energy scales of phonon and spin excitations are a serious hindrance for determining relative interaction strengths in the cuprates [120, 121]. In turn, it seems rather insightful to study magnetic metals. For example, spin wave energies in the elemental ferromagnets such as Fe, Co, and Ni are exceptionally high, well exceeding those of phonons and making it thus a good candidate for such studies. A very important property of the ARPES experiment is that it probes the solid (including the many-body interactions) in terms of an *excited* state. In particular, the incoming photon removes an electron from the many-body system, and an excited hole state remains. The spectrum recorded in ARPES, based on a Green's function algorithm (which reflects the response of the many-body system), is given by the so-called *spectral function*. The spectrum obtained in the presence of interactions in the electron system can be written as [122]

$$A(k,\omega) \propto \frac{\mathrm{Im}\,\Sigma(\omega)}{[\hbar\omega - \varepsilon_k - \mathrm{Re}\,\Sigma(\omega)]^2 + [\mathrm{Im}\,\Sigma(\omega)]^2} \tag{2.136}$$

Here, ε_k is the (hypothetical) noninteracting dispersion. The real and the imaginary part of the so-called self-energy $\Sigma(\omega)$ reflect the contribution of the interaction to the spectrum. It is an important consequence that the photoemission spectrum described by $A(k,\omega)$ is no longer a delta function (as it was in the noninteracting case, marking the corresponding band dispersion), yet it is an intensity landscape when plotted upon energy ω and momentum k. $\mathrm{Im}\,\Sigma(\omega)$ incorporates the scattering processes and is given by an integral over the density of states of those bosonic

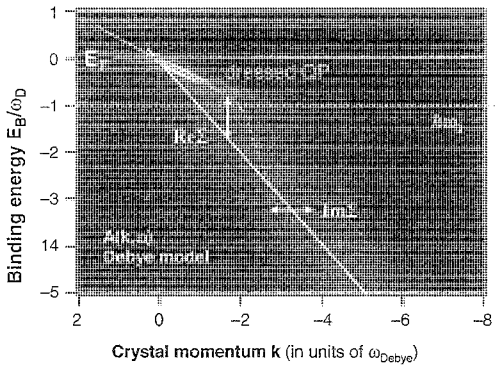

Figure 2.23 Spectral function generated numerically ($T = 20$ K, $T_{debye} = 340$ K, impurity scattering 10 meV). The shift of spectral weight near the Fermi level and a reduced slope become obvious. The self-energy Σ implies a broadening (given by $\mathrm{Im}\Sigma$) and an energy shift (given by $\mathrm{Re}\Sigma$) of the spectrum compared to the noncoupling case. (Please find a color version of this figure on the color plates.)

modes the electron is coupled to. This is, for example, the phonon density of states in the case of electron–phonon coupling:

$$\mathrm{Im}\,\Sigma(\omega) \propto \lambda \int_0^{\omega} \varrho_{\mathrm{Phonon}}(\Omega)\mathrm{d}\Omega \tag{2.137}$$

where λ is the coupling constant. Note that $\mathrm{Im}\,\Sigma(\omega)$ relates to the lifetime of the excited state, as explained in Section 2.2.3 in connection with Eq. (2.12). The phonon density of states can, for example, be described by the Debye model as in Eq. (2.17) for bulk phonons. $\mathrm{Im}\,\Sigma(\omega)$ leads to a *broadening* of the spectral function $A(k,\omega)$. The real part $\mathrm{Re}\,\Sigma(\omega)$ is then obtained from a Kramers–Kronig transformation, similar to relations known from optics. It leads to an *energy shift* of the spectrum. As an example, in Figure 2.23 the spectral function is plotted from a computer simulation for coupling of the electrons to a Debye-type phonon dispersion with a maximum energy of $T_{\mathrm{Debye}} = 340$ K. The coupling constant λ can be extracted from the slope of the dressed quasi-particle band, which is renormalized by $1/(1+\lambda)$.

2.4.2.2 Experimental Considerations for Photoelectron Spectroscopy

Experimentally, studies of electron–phonon and electron–magnon coupling are very commonly performed at synchrotron light sources. Their advantage is twofold. For one, they provide high brightness that allows studies on samples (such as metal surfaces) with limited lifetime before degradation, and second, the tunability of the photon energy allows one to choose rather high energies not available with helium discharge lamps. In particular, in going to photon energies near ≈ 100 eV, the assumption of free-electron final states becomes justified, so that final state effects do not modulate the spectral function $A(k,\omega)$ of the initial state in unwanted manner. The ARPES experiment also usually requires very high energy and angular

resolution, to achieve the best possible account of the spectral function $A(k,\omega)$. With the advent of modern electron analyzers with imaging detectors, energy and angular resolution values on the order of $\approx 5-10$ meV and $0.1°$ have become feasible. In addition, the beamline optics may contribute notably to the finite resolution. A total experimental resolution of $\approx 10-20$ meV seems practical today.

Best observation of self-energy effects in ARPES is achieved on surface states and resonances [119, 122], as will be illustrated in the experimental examples below. The reason is that these states have little or no dispersion in direction perpendicular to the surface. Since photoemission has a finite electron escape depth on the order of 10–20 Å for common photon energies in the range of 20–130 eV, this implies a small broadening of the k-perpendicular component, which in turn might affect or slightly distort the spectral function. Thus, surface states without this influence usually are the best candidates to look even for small renormalization effects. In photoemission from *bulk* states, one has thus to precisely consider the energy broadening of the spectra due to escape depth of the photoelectron. It leads to a broadening of the final state, showing a Lorentzian distribution in $k_\perp$ with a full-width at half-maximum of $k_\perp = w^{-1}$, where w is the mean free path of the electron. This results in a total energy broadening of the spectra with contributions from the hole state and the photoelectron [123]:

$$\Gamma_{\mathrm{tot}} = \Gamma_{\mathrm{h}} + \frac{|v_{\mathrm{h}}|}{|v_{\mathrm{e}}|}|\Gamma_{\mathrm{tot}} \tag{2.138}$$

where $v_{\mathrm{e/h}} = \partial\varepsilon_{\mathrm{e/h}}/\partial k_\perp$ are the velocities of electrons and holes, respectively. Hence, the final state might influence the photoemission spectrum significantly, unless the dispersion v_{h} of the initial state perpendicular to the surface is vanishing. This is fulfilled, for example, for surface states. Yet even for bulk states, the crystal symmetry can be favorably exploited. Selecting the photon energy such that k lies in a *high-symmetry plane* implies an extremum in the band topology. Thus, v_{h} will vanish, leaving Γ_{h} as the desired quasi-particle contribution of interest. This is illustrated in detail in Ref. [124].

2.4.2.3 Quasi-Particles from Electron–Phonon Interaction

An interesting realization of coupling of electron states to phonon modes is achieved at the surface of metals. Not only does this provide good observation conditions for the renormalization but also special vibrational modes solely observed for surface adsorbates can be studied. Studies on free metal surfaces have, for example, been performed on Mo(110) and Be(0001) surfaces [118, 119]. Here, a kink on the phonon energy scale was observed near the Fermi level, as expected according to Figure 2.23. The physics of electron–phonon interaction at surfaces with adsorbate phonons can nicely be studied by using a W(110) substrate, where one can, for example, prepare a monolayer coverage with hydrogen, as illustrated in Figure 2.24a. Its vibrational properties have been studied by scattering methods in the past [125]. Also, the surface states of the clean substrate are well known [126]. On the Fermi surface of H:W(110) on the $\bar{\Gamma}$–$\bar{S}$ line, metallic surface state are well separated from the bulk state. Here, quasi-particle renormalization is observed very clearly, as shown in

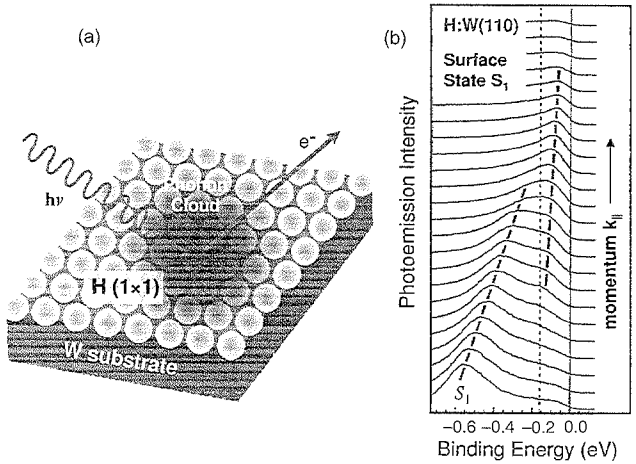

Figure 2.24 The H:W(110) system allows the study of adsorbate vibrations in the presence of interactions with a metallic electron bath. (b) Spectra of the surface state band ($T = 150$ K, $h\nu = 100$ eV). They reflect the electron–phonon coupling in an energy window of ≈ 160 meV that corresponds to the H stretching vibration. (Please find a color version of this figure on the color plates.)

Figure 2.23b. The energy window of ≈ 160 meV in which the renormalization occurs is in excellent agreement with the symmetric stretch vibration of the H atoms. The coupling constant of $\lambda \approx 1.4$ is rather large, and the question arises whether superconductivity might be achieved at low temperatures. Confirmation of the interpretation as due to adsorbate vibrations was obtained by performing an *isotope replacement* experiment of the adsorbate. For this purpose, the adsorption was done with deuterium instead of hydrogen. This reduces the oscillator frequency by a factor of $\sqrt{2}$ as expected, reflecting the mass increase of the adsorbate atoms [127]. These results help to elucidate the aspect of energy dissipation of adsorbates by electronic excitations in metallic substrates, which also has important implications for surface chemistry. Such nonadiabatic processes contribute to the dampening of adsorbate vibrations and thus are essential to controlling surface reaction mechanisms and kinetics.

2.4.2.4 Quasi-Particles from Electron–Magnon Interaction

Surface States of Magnetic Materials A prime candidate to explore the interaction of electrons with spin waves is ferromagnetic iron. Here, the energy scale of the spin waves [128, 129] is approximately one order of magnitude higher than that of the phonons. Furthermore, the recent observation of superconductivity in the nonmagnetic high-pressure phase of Fe has been related to electronic coupling with spin fluctuations [130]. Using high-resolution ARPES of the Fe(110) surface, two metallic surface state bands can be identified that display spectroscopic signatures

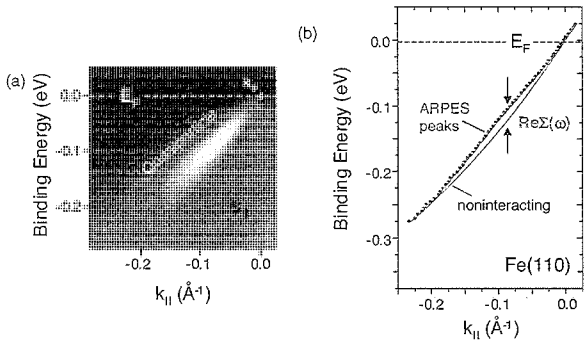

Figure 2.25 (a) ARPES data of the metallic Fe (110) surface state near $\bar{S}$ at $T = 85$ K. It is a surface resonance overlapping with the projection of bulk bands of opposite spin. (b) Peak position extracted from the band map using a fitting procedure (thick dots). The smooth line is a parabolic interpolation for the noninteracting band. A deviation from this band extends over a large energy scale below the Fermi level. Reprinted with permission from Ref. [131]. Copyright (2004) by the American Physical Society. (Please find a color version of this figure on the color plates.)

of quasi-particle renormalization. For ferromagnetic iron, the (110) face exhibits metallic surface states s_1 and s_2 around the $\bar{N}$ and the $\bar{S}$ points of the Brillouin zone, respectively. Both are of minority spin character, as explained in Ref. [131]. Spin interaction becomes possible because they overlap in energy with the surface-projected bulk bands of opposite spin.

The experimental dispersion of these surface states near the Fermi level extends along $\bar{\Gamma}$–$\bar{S}$ for s_1 and along $\bar{\Gamma}$–$\bar{N}$ for s_2. In the raw data of surface state s_1 in Figure 2.25a, the dressed quasi-particle region shows up with high intensity extending beyond 0.1 eV binding energy. The accurate peak position and width are obtained from a fit [119] of the momentum spectra at constant energy shown in Figure 2.25b. One typically uses a convoluted Lorentzian–Gaussian lineshape where the Gaussian part takes care of the experimental broadening. The Lorentzian width is used for the self-energy analysis. The dispersion displays a weak "kink" in the 100–200 meV region below E_F, which bears much resemblance to quasi-particle renormalization effects observed for electron–phonon coupling [118, 119]. The dispersion anomaly becomes obvious when comparing it to the nominally "undressed" dispersion. The undressed band is obtained here by parabolic interpolation between the lowest data points and the experimental Fermi vector, as included in Figure 2.25b. The experimentally determined dispersion is significantly offset from the noncoupling band interpolation. This suggests the interpretation that the observed kinks are indeed caused by many-body effects. The real part of the self-energy $\mathrm{Re}\Sigma(\omega)$ is the *difference* between interpolated and observed band dispersion, as marked in Figrue 2.25b. For both surface bands, it increases toward a maximum around 125 ± 10 meV and then gradually approaches zero again. The imaginary part of the self-energy, $\mathrm{Im}\Sigma(\omega)$, as displayed in Figure 2.26, reflects the scattering processes that increase with increasing binding energy. It is given by the Lorentzian

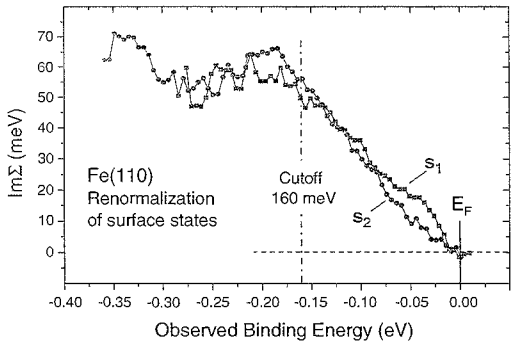

Figure 2.26 Imaginary part of the self-energy of the Fe(110) surface state, determined from the width of the ARPES momentum spectra. The increasing broadening reflects the interaction that the electrons are experiencing. The characteristic energy of $\approx$ 160 meV (which marks the saturation) coincides with known magnon energies.

half-width of the momentum spectra, applying the energy scale of the undressed band. Impurity scattering [119] adds a small offset of 30 meV that one has to subtract. The pronounced increase in $\mathrm{Im}\Sigma(\omega)$ with binding energy saturates at 160 ± 20 meV. The large energy scale clearly rules out electron–phonon coupling as origin. The phonon spectrum of iron has a maximum energy of $\approx$ 30 meV in the bulk [132] and also at the (110) surface [133]. This energy scale may be faintly visible in the data for s_1, yet cannot be considered relevant on a larger binding energy scale. Electron–electron scattering through Coulomb interaction [119] cannot account for characteristic structure either since in iron the total electronic density of states is smooth in the relevant energy region. Thus, we are left to consider coupling of the electrons with magnetic excitations.

Magnons in ferromagnetic Fe are well known from inelastic neutron scattering [128, 129]. Between approximately 100 meV and 200 meV both experiment [129] and theory [134, 135] find an "acoustic" and an "optical" magnon branch, separated by a gap where sharply defined spin waves do not exist. An acoustic spin wave branch has also been inferred from magnetization studies, locating its cutoff at 166 meV [136]. This energy scale is remarkably close to the characteristic energy observed in ARPES. It suggests the interpretation in terms of electron–magnon quasi-particle renormalization. Independent evidence comes from spin-polarized electron energy loss spectroscopy on the Fe(110) surface [137]. A loss structure at 170–200 meV is interpreted as exchange scattering by spin waves. It has been argued that spin waves at larger energies will be dampened by the onset of Stoner excitations [138]. We also note that a study on Co films observed strong electronic interaction only with the acoustic magnon branch [139], in very good agreement with our ARPES data. The compatibility of the ARPES self-energies with an electron–magnon coupling scenario can be tested using a simple model in analogy to electron–phonon coupling. The model uses the magnon density of states for the interaction, as described in Ref. [131]. It must be mentioned that a precise theoretical treatment of modified

quasi-particle spectra due to spin excitations does not exist to date. While several approaches are available to describe magnons per se, as laid out in Section 2.3.2.2, the interaction of hole states with magnons (both of electronic nature) will require an advanced many-body approach. Thus, the bosonic magnon coupling model used here must be considered a simplification, albeit justified *a posteriori* by its effectiveness. The functional form of $\mathrm{Im}\Sigma(\omega)$ and $\mathrm{Re}\Sigma(\omega)$ is well reproduced. Notably, one finds that the peak in $\mathrm{Re}\Sigma(\omega)$ occurs before the maximum mode energy, that is, at 0.79 ω_0, beyond which it decreases asymptotically. The analysis yields a coupling constant of $\lambda = 0.20 \pm 0.04$, indicating a relatively moderate coupling. It may relate to the fact that scattering occurs from spin-down *surface* states into spin-up *bulk* states with a rather small spatial overlap. Alternatively, the electrons may also couple to *surface* magnons. These have been found recently on the very same energy scale ($\approx$ 160 meV) by spin-polarized electron energy loss spectroscopy of the Fe(110) surface [140].

Interaction with Magnons in Bulk Magnetic Metals The question of electron energy renormalization in bulk magnetic materials has important bearing on correlated materials in general. They often exhibit an (anti-)ferromagnetically ordered phase. For access to these many-body interactions, a three-dimensional Fermi liquid in the ferromagnetic state seems a suitable model system. The energy scales for the lattice and spin wave excitations in typical ferromagnets such as Ni differ by approximately an order of magnitude, and hence will affect the quasi-particles at different binding energies [132, 141]. Furthermore, it is established that the valence band states are strongly correlated [142, 143], which is proven by a concomitant photoemission satellite. This allows to directly address the interplay of correlation physics and quasi-particle formation in the presence of distinct spin excitations. Here, we discuss an ARPES study of quasi-particle states in Ni(110) [124]. Despite the ubiquitous problem of perpendicular momentum broadening, suitable observation conditions can be found for *bulk* bands. An electronic self-energy analysis is carried out by comparison with a Gutzwiller calculation that describes quasi-particle renormalization more reliably than state-of-the-art density functional theories [144, 145].

A clean Ni(110) crystal was prepared by repeated Ar sputtering and annealing of a crystal *in situ*. During ARPES, the sample was kept at $T = 10$ K, and to ensure validity of the free electron final-state approximation, a high photon energy of 100 eV was chosen. For the purpose of studying quasi-particle effects in a wide energy range, the minority spin band at the K-point (labeled Σ_2) was selected. The ARPES data in Figure 2.27 show the band of interest, which is unaffected by neighboring states for binding energies up to 800 meV. A reliable method for determining the self-energy Σ (in terms of $\mathrm{Re}\Sigma$ and $\mathrm{Im}\,\Sigma$) is from the peak positions ω and widths Δk of the momentum distribution curves. Then, $\mathrm{Re}\Sigma(\omega) = \varepsilon(k) - \omega$, where $\varepsilon(k)$ is the bare band dispersion, and $\mathrm{Im}\,\Sigma(\omega) = |v(k)|\Delta k$, where $|v(k)|$ is the slope of the bare band and Δk the half-width at half-maximum of the peak [124]. For extraction of the self-energy contribution, a Gutzwiller calculation for Ni was used as reference [146] because in the Gutzwiller theory, electron–electron correlation effects are accounted for in a much better way than in density functional theory calculations. Hence, deviations of the experimental dispersion should result essentially from coupling of

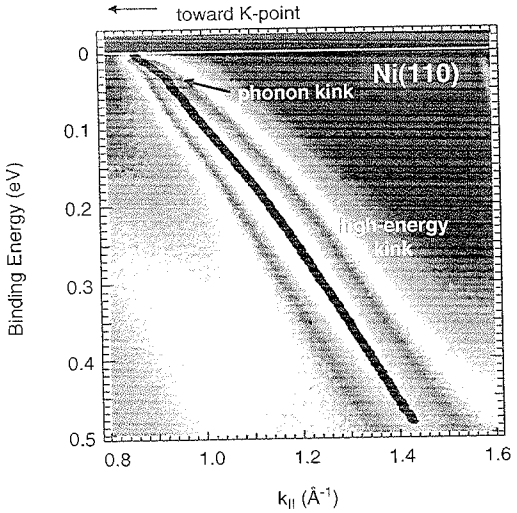

Figure 2.27 ARPES data of Ni(110) recorded at $h\nu = 100$ eV (corresponding to a high-symmetry plane). The band map shows the bulk band near the *K*-point. The momentum distribution curves are fitted to yield the peak positions. At low and high binding energy (as indicated), indications for kinks in the dispersion are discernible, corresponding to the phonon and magnon energy scale, respectively. Reprinted with permission from Ref. [124]. Copyright (2009) by the American Physical Society. (Please find a color version of this figure on the color plates.)

the electrons to bosonic excitations. The results for ReΣ and ImΣ as a function of binding energy are plotted in Figure 2.28a and b, respectively. Comparing experimental data and calculation, a first-mass renormalization can be found around $E_B \approx 30$ meV, which corresponds to the kink expected for electron–phonon coupling [147]. The visibility of this feature proves the high quality of the data. It demonstrates that many-body interactions are indeed observable in bulk bands at high-symmetry planes. A second deviation from the calculation is found in the binding energy region from 250–300 meV. This behavior is reflected by the real part of the self-energy in Figure 2.28a, which is showing a second maximum, corresponding well to the structure of the imaginary part ImΣ in Figure 2.28b. Hence, there is strong indication of a second many-body interaction effect at higher binding energies in both parts of the self-energy. A plausible explanation in a ferromagnet with correlated electrons like Ni is the coupling of the electrons to spin wave excitations.

Magnons in Ni are well known from inelastic neutron scattering, which yields energies up to 250 meV [141]. However, this method is problematic for scattering at large wave vectors, which makes it difficult to obtain data near the zone edges. Therefore, one expects an even larger energy for the maximum of the spin wave spectrum. Cutoff energies obtained by various calculations are 270–370 meV [134, 148, 149]. In an attempt to model the observed characteristics of the self-energy, the

simple relation known from electron–phonon coupling as used above is analogously applied here: $\mathrm{Im}\,\Sigma(\omega) \propto \lambda \int_0^{\omega} \varrho_{\mathrm{bos}}(\Omega)\mathrm{d}\Omega$, where ϱ_{bos} is the boson density of states and λ is the coupling constant. From the linear dispersion for bulk phonons and the quadratic one for bulk magnons, up to their respective cutoffs ω_0, it follows $\varrho_{\mathrm{pho}} \propto \omega^2$ and $\varrho_{\mathrm{mag}} \propto \omega^{1/2}$, respectively. These results can be used to calculate ImΣ contributions from electron–boson interaction with two parameters, the coupling strength λ and the cutoff energy ω_0. The corresponding real parts are calculated directly employing the Kramers–Kronig relation. The results for ReΣ and ImΣ are laid out in Figure 2.28a and b, respectively.

For a complete description of the imaginary part, one has to include the electron–electron scattering contribution, for which a quadratic energy dependence as obtained from Fermi liquid theory is assumed (effects such as impurity scattering and experimental resolution can be accounted for by a constant offset). These contributions add up linearly to the full imaginary part. Note that an electron–electron scattering contribution does not need to be considered explicitly for ReΣ because it is already included in the Gutzwiller reference band. With this model, the main features of both self-energy parts are very well reproduced; see Figures 2.24b and 2.25b. The parameters in the model for the cutoff energies are $\omega_{0,\mathrm{ph}} = 35$ meV and $\omega_{0,\mathrm{mag}} = 340$ meV. The latter is compatible with the available bulk spin wave data. The analysis also yields the coupling constants $\lambda_{\mathrm{ph}} = 0.3$ and $\lambda_{\mathrm{mag}} = 0.19$. The electron–magnon coupling is somewhat weaker than the electron–phonon coupling

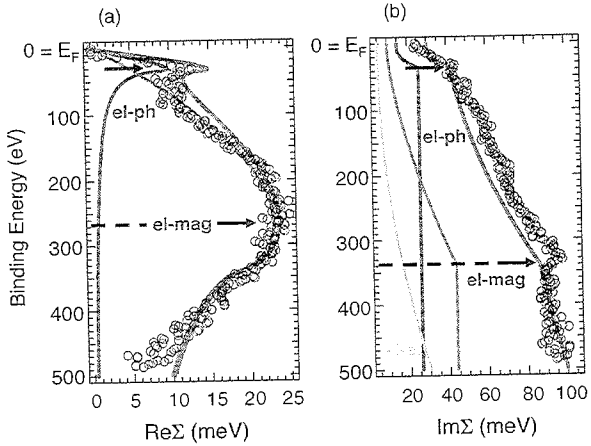

Figure 2.28 Self-energy analysis of the *K*-point band in Ni(110) derived from ARPES. (a) Real part ReΣ and (b) imaginary part ImΣ. In both panels, peaks in the self-energy are seen at energy scales that correspond to the phonons and magnons: in terms of ImΣ, this occurs at ≈ 30 meV and ≈ 340 meV, respectively. Note that in (a) a Gutzwiller reference band is used, which includes the electron correlation effects, so that they are effectively removed from ReΣ. In (b) for ImΣ, electron correlations have to be explicitly considered. The model curves for ReΣ and ImΣ are Kramers–Kronig transformable, consistent with the quasi-particle picture. Reprinted with permission from Ref. [124]. Copyright (2009) by the American Physical Society. (Please find a color version of this figure on the color plates.)

in this particular case. It should be added that the spectral features and magnitudes for $\mathrm{Re}\,\Sigma$ and $\mathrm{Im}\,\Sigma$ obey a Kramers–Kronig relation and *simultaneously* describe the experimental data very closely. This is a stringent criterion for the validity of the electron–magnon coupling picture, and proves that this model can well explain the observed phenomenon.

2.4.2.5 Conclusions and Implications

While electron–phonon coupling is well established and has been reported extensively in the past, including ARPES, electron–magnon coupling studies are rather novel. While first demonstrated for a surface state [131], experiments on bulk magnetic materials show that it is feasible to deduce quasi-particle interactions even in three-dimensional solids, using a technique based on high-symmetry planes. The self-energy extracted with high precision including a Gutzwiller reference satisfies the Kramers–Kronig criterion. It reveals characteristic structure in the quasi-particle dispersion that is well compatible with known spin wave energies. In the context of correlated materials, kinks have also been observed in high-temperature superconductors [121]. It is being discussed whether such kinks are derived from coupling to phonons or to spin fluctuations, while their similar energy scales in those materials make them difficult to separate. Particularly close resemblance to magnetic metals is found in the newly discovered iron-based pnictides [150]. Their parent compounds are metals with an antiferromagnetic spin density wave. A pairing mechanism based on spin fluctuations has been suggested [151]. The ARPES observations on elementary metals strongly suggest that renormalization effects reported to date for the cuprates [120] might relate to coupling to magnetic fluctuations. This implies important consequences for models of high-temperature superconductivity based on spin-mediated pairing. Such interpretation would be in line with a number of theoretical treatments, for example, on cuprates, in which the emergence of kinks has been attributed to the coupling of quasi-particles and bosonic (antiferromagnetic) spin excitations [152–154]. Regarding the detailed microscopic nature of the quasi-particle renormalization relating to spin excitations, a different explanation was suggested recently for strongly correlated electron systems, which does not require electron–boson coupling. In extended model calculations for pure electron–electron interaction, it was found that two well-separated regimes of quasi-particle renormalization can result [155]. While near the Fermi level well-defined quasi-particles exist according to Fermi liquid theory, at higher energies the self-energy changes abruptly, resulting in reduced quasi-particle lifetimes. In the transition between these situations, a dispersion anomaly is expected to emerge [155]. In this picture, kinks appear due to the frequency dependence of the local self-energy within the dynamical mean field theory. The results in Ref. [155] allow an estimate of the binding energy at which the kink would be expected. For the parameters of the Ni bandstructure, a coarse approximation yields $\approx$ 330 meV [10], which is in the same range as the observed kink energy in $\mathrm{Re}\Sigma$ of 270 meV. However, that kink scenario [155] was developed for a paramagnetic single-band model in infinite dimensions with strong quasi-particle renormalization. In contrast, Nickel is a ferromagnetic multiband system with only moderate renormalization of quasi-particle masses.

Therefore, it remains open whether or not the approach in Ref. [155] is of relevance for the kinks observed in Nickel. Yet, intriguingly, probably the boundary between coupling to a well-defined spin excitation on the one hand and coupling between electrons on the other hand might not sharply be drawn. This does not question the existence of well-behaved magnons seen in scattering experiments [141], but rather pertains to the nature of the quasi-particle. The interaction model of Byczuk *et al.* [155] may be seen as a different methodical ansatz for the same quasi-particle phenomenon. In extending this approach, a recent theoretical study [156] argues that this kink formation can, in fact, be viewed as resulting from emerging *internal* collective excitations – which are addressed as spin excitations or magnons by the experimentalists.

2.4.3 Time-Resolved Photoelectron Spectroscopy

In this section, we briefly discuss what can be learned from time-resolved photoelectron spectroscopy about the excitation and the decay of quasi-particles. For these purposes, we will focus on a few model cases studying the lifetime of photoexcited electrons, electron–phonon coupling, surface exciton formation, and magnon emission. There are a number of elaborate reviews considering time-resolved photoemission spectroscopy and quasi-particle dynamics (see, for example, Refs [4, 9]). For further reading, we also refer the reader to Volume 1 of this series.

2.4.3.1 Experiment

As illustrated in Figure 2.29a and b, there are two major schemes applied in time-resolved photoemission.

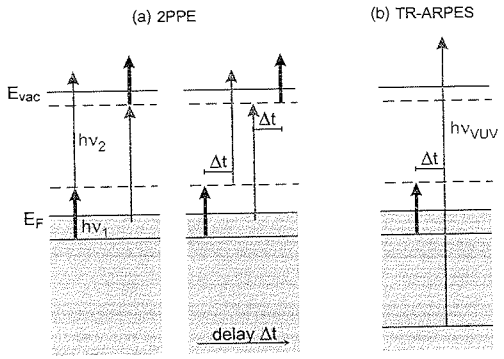

Figure 2.29 Excitation scheme of (a) bichromatic time-resolved two-photon photoemission (2PPE) spectroscopy and (b) time- and angle-resolved photoemission spectroscopy (TR-ARPES). Varying the delay Δt between pump and probe pulses allows us to follow the dynamics of excited states and ensembles, and thereby the creation of quasi-particles and collective excitations.

Two-Photon Photoemission In what is usually called two-photon photoemission, two femtosecond laser pulses with photon energies below the work function (metal) or ionization potential (semiconductor) are applied to populate and probe unoccupied states between the Fermi level E_F (metal) or valence band maximum (VBM) (semiconductor) and the vacuum level E_{vac}. Laser pulses with photon energies in the visible to ultraviolet (UV) range ($\approx$ 2–6 eV) are sufficient to span this energy range for various materials. In bichromatic two-photon photoemission, different photon energies $h\nu_1$ and $h\nu_2$ are used. Thereby, direct photoemission is largely suppressed and laser pulse intensities I can be made sufficiently high to optimize the count rate $\propto I_1 \cdot I_2$ without running into space charge problems.

Common laser sources are tunable Ti:sapphire oscillators (730–870 nm, that is, $h\nu = 1.69-1.42$ eV) or regenerative amplifiers with 80 MHz or 300 kHz repetition rates, respectively. While the fundamental of an oscillator is either frequency doubled ($2h\nu$) or tripled ($3h\nu$), the higher output power of amplifier setups allows us to widely tune the photon energy via optical parametric amplification at the cost of the lower repetition rate [157]. Typical pulse energies range between 0.1 nJ and 1 µJ at pulse durations of 20–100 fs focused on spots of 50–200 µm diameter. To detect the photoelectrons, either electrostatic hemispherical analyzers or time-of-flight spectrometers (typical repetition rates $\leq$ 1 MHz) are used. For both types of analyzers, multidimensional detectors have been developed, which record arrays of energies and emission angles. As the kinetic energy of the photoemitted electron is only a few electron volts, special diligence has to be applied to obtain reliable energy versus angle maps and to derive band dispersions $E(k_{||})$. The momentum parallel to the surface $k_{||}$ is conserved in the 2PPE process. In a time-resolved measurement, such maps are recorded as a function of the pump–probe delay. In the simplest case, we observe a buildup of the population and its exponential decay. From the latter, we obtain the lifetime of a specific surface state, for example, at $E(k_{||} = 0)$.

Time- and Angle-Resolved Photoemission Spectroscopy When photon energies above the ionization energy are employed, the technique is usually termed time-resolved and angle-resolved photoemission spectroscopy (TR-ARPES) [158, 159]. Sources are either the fourth harmonic of a Ti:saphire laser system ($4h\nu$) [104], picosecond pulses of synchrotron radiation or femtosecond pulses of a free electron laser, both synchronized to a laser pump pulse [160–162], or higher harmonics generated by focusing mJ-pulses on a rare-gas target [158, 163–165]. In contrast to 2PPE experiments, in TR-ARPES the pump pulse is usually used to create a hot electron population and the response of the system to this rather massive perturbation is followed by photoemission spectroscopy. Vacuum ultraviolet light pulses (VUV) allow us to map the valence bands throughout the Brillouin zone or to probe at least shallow core levels. Space charge problems may either occur due to the intense pump pulse or due to the direct photoemission (for a detailed discussion, see Ref. [166, 167]). With TR-ARPES, laser-induced phase transitions have been studied, which reveal collective excitations, such as coherent phonons [91, 168, 169], and the coupling among quasi-particles, for example, electrons, phonons, and magnons belonging to the interacting heat baths of a ferromagnet [104, 170, 171].

2.4.3.2 Electron Lifetimes

In metals it is primarily a consequence of the electron–electron interaction that photoexcited carriers, that is, electrons and holes, have a finite lifetime. Here, we must distinguish between the lifetime of an individual state and the relaxation time of a photoexcited electron population, also referred to as *hot* electrons. *Ab initio* theories calculate the self-energy of a single state. On Cu(001) the image potential states constitute a well-defined Rydberg-like series of unoccupied states with binding energies converging toward the vacuum level $E-E_{vac} = 0.85\ \text{eV}\ (n+a)^{-2}, n = 1, 2, \ldots$ As these states are localized in front of the surface, they exhibit a lifetime much longer than bulk states at comparable energies above E_F. Time-resolved 2PPE measurements reveal that after being populated with an ultrashort laser pulse the image potential states on Cu(001) show an exponential decay of the intensity over four orders of magnitude [172, 173]. There is now excellent agreement between experimentally determined lifetimes and the *ab initio* calculations described in Ref. [9]. For Cu(001) decay is dominated by electron–electron scattering. Phonon emission contributes negligibly to the decay of the image potential states since the bulk penetration of these states and thus the coupling to the lattice is small [9, 174, 175].

The decay of an excited electron or photohole is accompanied by excitation of a secondary electron–hole pair to conserve energy and momentum in inelastic electron–electron scattering. In the time-resolved 2PPE experiment, the count rate in a certain energy and momentum window is recorded as a function of the delay between the pump and the probe pulses. If a photoexcited state gets repopulated from higher excited states or by secondary electrons, the lifetime of the individual state is no longer measured but the population dynamics of the hot electron population. This can be nicely illustrated by 2PPE measurements of the population dynamics of the first image potential state in iron shown in Figure 2.30. When the photon energy of the UV pump pulse is just sufficient to excite the $n = 1$ state from occupied states at E_F ($3h\nu = 4.43$ eV, Figure 2.30a), the measured lifetime of the minority and majority components is $\tau_\downarrow = 11 \pm 2$ fs and $\tau_\uparrow = 16 \pm 2$ fs. These spin-dependent lifetimes are attributed to the spin-dependent density of states in the ferromagnetic iron film [176–179]. The spin resolution in the measurement will become important for discussing magnon emission in Section 2.4.3.5. At higher photon energies ($3h\nu = 4.85$ eV, Figure 2.31b), the pump pulse excites electrons along the parabolically dispersing image potential band up to E_{vac}, and intraband decay leads to a repopulation of the band bottom. As a consequence, the apparent spin-dependent lifetimes of the $n = 1$ image potential state at $k_{||} = 0$ increase to $\tau_\uparrow = 19 \pm 2$ fs and $\tau_\downarrow = 17 \pm 2$ fs. Intraband scattering involves the excitation of a secondary electron–hole pair close to the Fermi level (cf. Figure 2.31) and opens a significant decay channel for electrons above the bottom of the image potential-state band [180].

A related situation is found for the decay of hot electrons in bulk copper [182]. Figure 2.31a summarizes measured relaxation times and calculated lifetimes for Cu (001) and Cu(111) as a function of the excitation energy $E-E_F$ above the Fermi level. For these monochromatic 2PPE measurements, the surface workfunction was lowered by Cs adsorption. The experimental data sets were recorded for photon

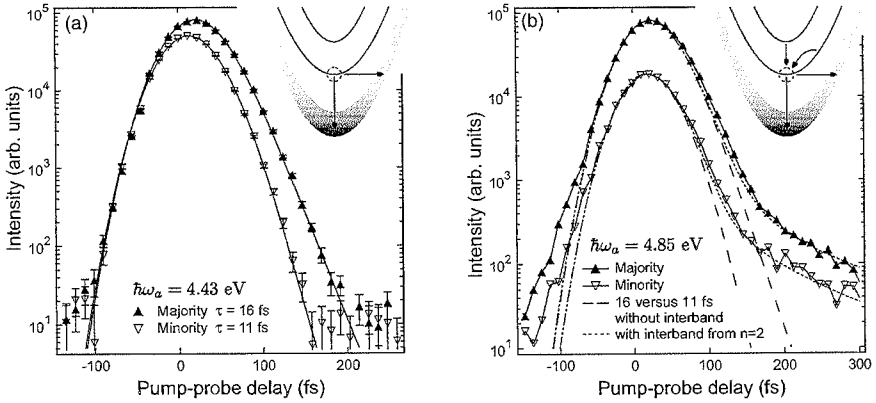

Figure 2.30 Time- and spin-resolved measurements of the $n = 1$ image potential-state lifetime for a 3 ML iron film deposited at room temperature on Cu(001). (a) A UV pump pulse with a photon energy of 4.43 eV populates only the band bottom. (b) For the higher photon energy of 4.85 eV, the image state band is excited up to E_{vac}. In the latter case, inter- and intraband decay leads to a repopulation of the band bottom and apparently longer lifetimes at $k_{||} = 0$. Reprinted with permission from Ref. [181].

energies of about 3.0–3.4 eV [183–185] and 1.63 eV [185] and show differing data in the overlapping energy range. By tuning the photon energy, later experiments revealed, for an intermediate-state energy of $E-E_F = 1.65$ eV, relaxation times of 13, 67, and 42 fs for $h\nu = 3.81$, 3.4 and 3.6 eV, respectively [186]. This difference can be explained by considering the schematic band structure of copper in Figure 2.31b. The processes A and B illustrate sp-intraband transitions (Drude absorption), including phonon or defect scattering, and the much stronger direct transitions from d- to sp-bands. In the latter process, d-band holes are photogenerated and their decay leads to secondary electrons. Due to the high probability of direct transitions B, d-band holes and thus secondary electrons are generated in large numbers. Taking into account the longer relaxation time and localization of the d-band holes [186, 187] substantiates the dependence of the relaxation time on the photon energy; the Auger-like decay of d-band holes (process C in Figure 2.31b) with maximum energy $E_F-h\nu$ leads to a delayed repopulation of states above the Fermi level with a maximum energy of $E_F + h\nu$.

Typical Fermi velocities in metals are on the order of 10^6 m/s [189]. In the case of copper, electrons at the Fermi level have a velocity on the order of 15 Å/fs [190]. Therefore, ballistic transport of the delocalized sp-electrons will contribute to their relaxation time. Since the group velocity and the orientation of the surface-projected band gaps depend on the crystal direction, relaxation times are expected to vary with surface orientation. Small changes in the relaxation time have been demonstrated, for example, for the copper crystal faces (100), (110), and (111); they do, however, not correlate with the Fermi velocity [183].

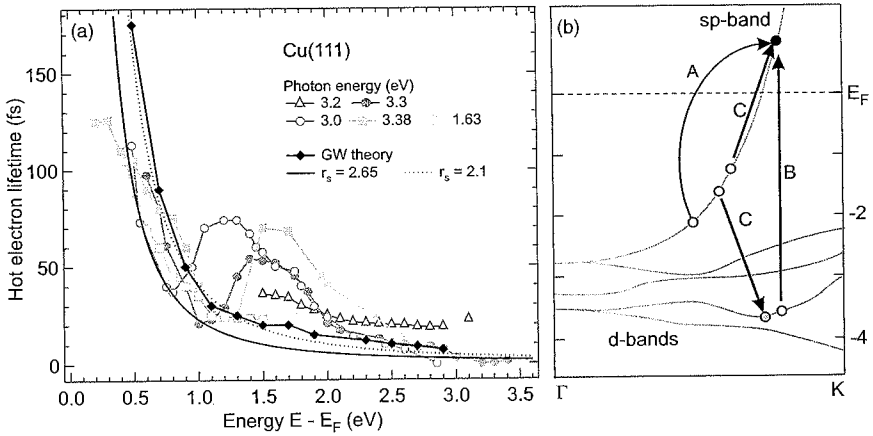

Figure 2.31 (a) Lifetimes of hot electrons in copper as a function of the excitation energy $E-E_F$. All data were taken with pump and probe pulses of the same photon energy $h\nu_1 = h\nu_2 = h\nu$. To lower the surface workfunction alkali metals, such as K and Cs, were adsorbed. Open triangles (Ref. [183]), $h\nu = 3.2$ eV; filled circles (Ref. [184]), Cu(111) $h\nu = 3.3$ eV; open circles (Ref. [184]), Cu(111) $h\nu = 3.0$ eV; filled squares (Ref. [185]), Cu(100) $h\nu = 3.38$ eV; open squares (Ref. [185]), Cu(100) $h\nu = 1.63$ eV; solid diamond (Refs [182, 188]), Cu(111) LMTO GW calculation; and solid and dashed line (Eq. (2.140)) for $r_s = 2.65$ and 2.1. (b) Schematic bulk band structure of copper and various excitation pathways. (A) Drude intraband absorption, (B) interband absorption, and (C) sp-band refilling via Auger decay of long-lived d-holes.

In conclusion, measured electron relaxation times do not represent the pure electronic lifetimes, although the energy-dependent hot electron lifetime for inelastic e–e scattering is the dominant quantity in the relaxation dynamics. This is confirmed by the reasonable agreement of the experimental results obtained for $h\nu = 1.63$ eV with *ab initio* GW calculations for a plane wave [191] or a linear muffin-tin orbital (LMTO) basis set [188] (diamonds in Figure 2.31a). The GW calculations are far from the lifetimes $\tau(E)$ obtained using the free electron gas theory.

$$\tau(E) = 263 \cdot r_s^{-5/2}(E-E_F)^{-2} \tag{2.139}$$

$$n_0 = \frac{3}{4\pi}(r_s a_0)^{-3}. \tag{2.140}$$

Here, a_0 is the Bohr radius and n_0 is the electron density. Good agreement can be obtained only for the radius $r_s = 2.1$ (dashed line in Figure 2.31a) that differs significantly from the value $r_s = 2.65$ obtained from the number of copper s electrons and the lattice parameter (solid line) [182]. The shorter relaxation times observed at low excitation energies are attributed to transport processes, which are not included in the calculations [186, 188]. Besides transport processes, *ab initio* calculations generally neglect secondary electrons, which are always excited in inelastic electron–electron scattering and lead to a repopulation of states above E_F [179].

2.4.3.3 Electron–Phonon Coupling

So far, we have compared the measured relaxation rate of photoexcited electrons and their calculated lifetime. We learned that even at low excitation densities, that is, in the regime of single excitation events, electron decay is influenced by repopulation and transport. 2PPE measures the lifetime only for individual states, such as surface states, and only with a proper choice of the excitation energy. In addition, transport into the bulk is disabled for a state localized at the surface.

The study of the decay of excited electron ensembles, that is, the regime of high excitation density, was pioneered by Bokor and coworkers [192, 193]. For metals it can be investigated by monitoring the electron distribution function above and below the Fermi edge as a function of the pump–probe delay [193, 194]. In a semiconductor, the transient population, for example, near the conduction band minimum of silicon, is recorded [195–197].

Let us assume a constant density of states in the vicinity of the Fermi level. A schematic of the electron density $n(E)$ after laser excitation is sketched in Figure 2.32. Optical absorption repopulates states in the energy interval $[E_F - h\nu, E_F + h\nu]$. During the excitation with the femtosecond laser pulse, the electron distribution is strongly nonthermal. Electron–electron scattering leads to thermalization of the electron gas after which its density can be modeled by a Fermi distribution $f(E, T_e) = (\exp(E - E_F)/(k_B T_e) + 1)^{-1}$ at an elevated electronic temperature T_e. In a metal, this equilibration within the electronic system takes about 100 fs. In semiconductors, carrier–carrier scattering depends on the excitation density and becomes important at a density of about 10^{17} cm^{-3}, where similar timescales are observed [197, 198].

The excess energy in the electron system decays by interaction with the lattice through phonon emission. In a magnetic sample, the spin system adds an additional heat bath and dissipation channel. Both electrons and phonons can couple to magnons and thereby create a wealth of coherent and incoherent quasi-particle and collective excitations. Depending on the excited and probed sample volume, transport processes may also add to the decay of T_e measured in photoemission.

To illustrate the above discussion for a metal and a semiconductor, we next highlight recent studies of gadolinium from Bovensiepen (see Ref. [104] and references therein) and of silicon from Ichibayashi and Tanimura [197].

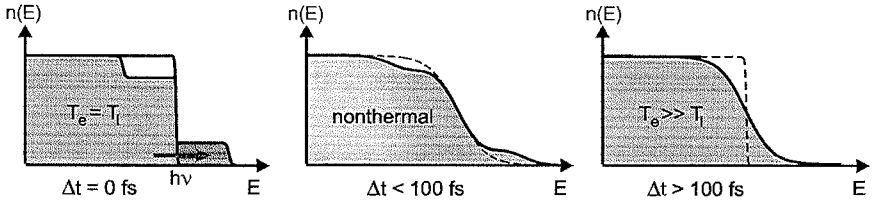

Figure 2.32 Schematic of the electron distribution $n(E)$ as a function of energy E after laser excitation. Ultrafast thermalization occurs via electron–electron scattering. Some 100 fs after laser excitation, the electron distribution is described by a Fermi function with an electron temperature T_e of a few thousand Kelvin, while the lattice temperature T_l is close to the initial temperature.

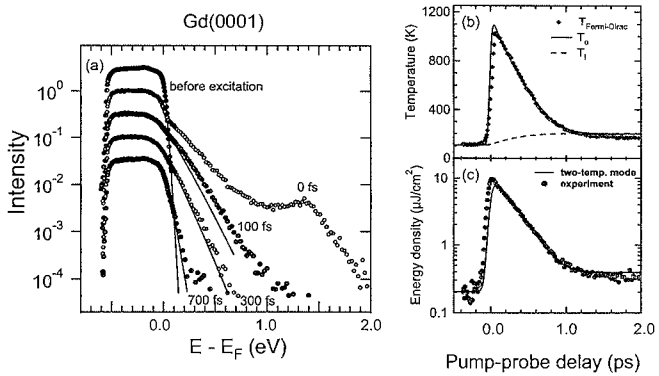

Figure 2.33 (a) Spectra of hot electrons at the Gd(0001) surface recorded for different pump–probe delays. The black lines are fits assuming a constant DOS and a Fermi–Dirac distribution with electron temperature T_e. (b) Transient temperature and (c) energy density of the electronic system. The adsorbed fluence is 0.25 mJ cm^{-2}. Solid lines show simulations based on the two-temperature model. Reprinted with permission from Ref. [104]. Copyright (2007) by the Institue of Physics.

Figure 2.33a depicts the transient electron population close to the Fermi level for a 10 nm Gd(0001) film grown epitaxially on W(110) (work function 3.4–3.7 eV). The sample was excited by an IR pump pulse ($h\nu = 1.5$ eV, 55 fs FWHM duration) with a fluence of 0.25 mJ/cm^2 and probed by the frequency-doubled signal of an OPA ($h\nu = 4.2$ eV, sub-50 fs pulse duration).

In the vicinity of the Fermi level, the gadolinium bulk DOS is nearly constant and the photoelectron signal is described by a Fermi–Dirac distribution. At zero delay $\Delta t = 0$ fs, the electron distribution is nonthermal and electron–electron scattering leads to excitation energies exceeding the pump pulse photon energy. After 100 fs the distribution is thermalized. The transient temperature of the electron gas (circles in Figure 2.33b) is extracted by fitting a Fermi–Dirac distribution to the photoemission data in Figure 2.33a. It is well described by the two-temperature model introduced by Anisimov *et al.* [199] for the case of laser excitation.

$$\begin{aligned} C_e(T_e)\frac{\partial T_e}{\partial t} &= S(z,t) - H(T_e, T_l) + \frac{\partial}{\partial z}\left(\kappa \frac{\partial T_e}{\partial z}\right) \\ C_l(T_l)\frac{\partial T_l}{\partial t} &= H(T_e, T_l) \end{aligned} \tag{2.141}$$

These equations model the interaction of electrons and lattice with their specific heat capacities $C_e = \gamma T_e$ and C_l. The Debye model was used to include the temperature dependence of the lattice-specific heat. Since γ is small, T_e rises to 1000 K (at the moderate fluence of 0.25 mJ/cm^2) before the lattice grows warm $C_l \gg C_e$. The electronic part of the thermal conductivity κ describes the diffusive transport of energy assuming a linear temperature dependence $\kappa = \kappa_0(T_e/T_l)$ [200].

S is the absorbed energy density per time. Its temporal and spatial profiles are determined by the pump pulse and the optical penetration depth.

The quasi-particle interaction between electrons (momentum k' and k) and phonons (momentum $\pm q = (k'-k) \pm G$) is hidden in the term $H(T_e, T_l)$ that describes the energy transfer rate between the electron and the lattice subsystems (phonon emission and absorption, see Eq. (2.13) in Section 2.2.3).

$$H(T_e, T_l) = -\frac{2}{(2\pi)^3}\sum_q \hbar\omega_q \int d^3k' W_{kk'}\delta(E_k - E_{k'} - \hbar\omega_q) \times[(n_q+1)f_{k'}(1-f_k) + n_q f_k(1-f_{k'})]. \quad (2.142)$$

Here, n_q and f_k are the Bose–Einstein and Fermi–Dirac distribution functions of phonons and electrons, respectively. The energy transfer rate H has been calculated assuming one phonon emission and absorption of acoustic phonons in the Debye model ($\omega \propto q$) [201, 202].

$$H(T_e, T_l) = g(T_e) - g(T_l)$$
$$g(T) = 4g_\infty \Theta_D \left(\frac{T}{\Theta_D}\right)^5 \int_0^{\Theta_D/T} dx \frac{x^4}{e^x - 1} \quad (2.143)$$

The electron–phonon coupling constant g_∞ and the Debye temperature Θ_D depend on the material. Solving Eq. (2.14) yields the solid lines in Figure 2.33b. The femtosecond pump pulse heats a small fraction of the electrons to a temperature of about 1100 K. Within 1 ps the electron and lattice temperatures equilibrate and the (lattice) temperature increases from 110 to 170 K. The 1–2 ps is typical for the equilibration time between a laser excited electron distribution and the lattice. The hot electrons (and holes) can induce desorption [203], chemical reactions [204], or configuration switching [205] in molecules adsorbed at the surface. They also drive ultrafast laser-induced demagnetization [206, 207] and magnetic switching [208] in thin-film ferromagnets.

There is an obvious difference between hot electron relaxation in semiconductors and metals. When the photon energy of the pump pulse is smaller than twice the gap energy, electrons excited to the conduction band (CB) cannot decay into empty CB states and excite a secondary electron across the gap. Electron–hole recombination (Auger-like decay) scales with the third power of the excited density n [209]: $dn/dt = -(C_e + C_h)n^3$. For bulk silicon the measured Auger-decay constants are $C_e(C_h) = 2.8(0.99) \times 10^{-31}\,cm^6/s$ [210]. For densities of $n = 10^{17}\,cm^{-3}$ electron–electron scattering among the excited carriers becomes important [198]. However, at this density the effective decay constant amounts to $(C_e + C_h)^{-1}n^{-2} = 260\,\mu s$. Therefore, energy relaxation and population decay are dominated by electron–phonon scattering and defect – as well as surface –recombination [211]. Figure 2.34a shows 2PPE spectra of Si(111) 7 × 7 as a function of pump–probe delay. The intensity distribution near the silicon CBM is highlighted in the inset. Since the photo-generated carrier density of $10^{18}\,cm^{-3}$ is much less than the effective CB-DOS, the band shape was simulated by a Boltzmann distribution function with an

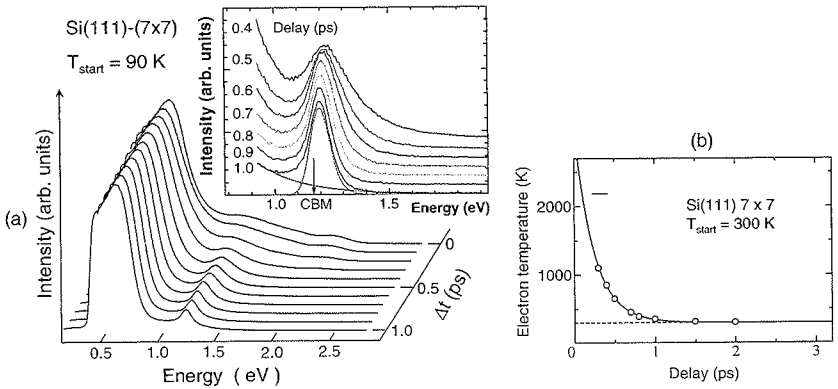

Figure 2.34 (a) Series of 2PPE spectra measured for Si(111) 7 × 7 for s-polarized 2.21 eV pump pulses (fluence ≈ 0.5 mJ cm^{-2}) and p-polarized 4.95 eV probe pulses. The inset shows the temporal evolution of the CB peak in an expanded scale from 0.4 to 1 ps delay. (b) The electron temperature at the CBM as a function of pump–probe delay. The solid curve is the fit of a single exponential decay component and a constant value of 296 K. The time constant is 240 fs. Reprinted with permission from Ref. [197]. Copyright (2009) by the American Physical Society. (Please find a color version of this figure on the color plates.)

effective electron temperature T_e, convolved with a 70 meV instrument resolution [197]. The decrease of T_e is shown in Figure 2.34b. The electron temperature can be described by an exponential curve with a time constant of $\tau_{e-p} = 240 \pm 20$ fs. This value fits nicely to the relaxation dynamics observed in previous all-optical studies [212]. On changing the sample temperature from 296 to 90 K, the time constant becomes 310 ± 10 fs. As the electron–phonon interaction scales with $2n_q + 1$ (Eq. (2.142)), the temperature dependence of τ_{e-p} reveals scattering with optical phonons of silicon with $\hbar\omega_q \approx 50$ meV. The 2PPE data demonstrate that the energy relaxation of hot electrons in silicon occurs via deformation potential scattering with optical phonons. This process leads to an equilibration of electron and lattice temperature on the timescale of 1 ps, comparable to gadolinium.

In Section 2.4.1, coherent phonons have been extensively discussed. Evidently coherent vibrations couple to the electronic system. A periodic variation in the bond distance leads to an oscillation in the binding energy, which can be followed in a pump–probe photoemission experiment with appropriate energy resolution. This allowed for the identification of phonon modes that are particularly important in phonon–magnon coupling [213] and for separating the relevant modes in charge density wave systems [91, 169].

2.4.3.4 Surface Exciton Formation

In the following paragraphs, surface exciton formation and its signature in 2PPE are described by monitoring the carrier dynamics at the silicon (100)-surface [211, 214]. The signatures of coherent and incoherent excitons in terahertz spectroscopy and photoluminescence studies of III–IV quantum well structures have been discussed

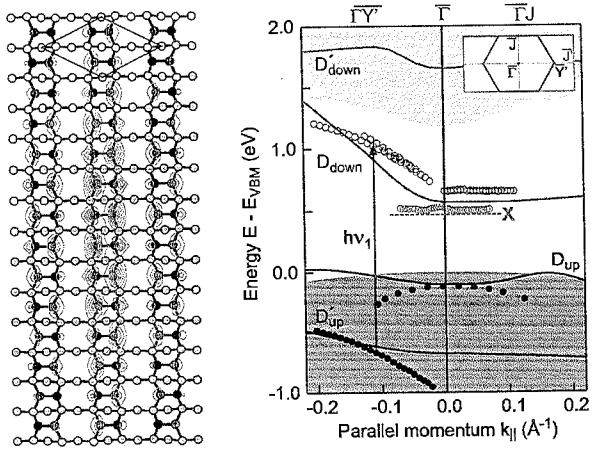

Figure 2.35 (a) The $c(4 \times 2)$ reconstruction of the Si(100) surface. Dimers are arranged in rows along the $[0\bar{1}1]$-direction and are alternately tilted along and perpendicular to the rows. The unit cell (solid rhombus) of the $c(4 \times 2)$ stacking comprises two dimers. The surface exciton is visualized by the contour plot of the probability density of the electron bound to the hole, located in the center of the depicted area. Reprinted with permission from Ref. [214]. Copyright (2005) by Springer. (b) Measured (symbols) and calculated (solid lines, shaded areas) surface-projected band structure of the Si(100) $c(4 \times 2)$ surface. $\overline{\Gamma Y'}$ and $\overline{\Gamma J}$ correspond to the directions along and perpendicular to the dimer rows. The presence of two dimers per unit cell leads to two occupied (D_{up} and D'_{up}) and two unoccupied (D_{down} and D'_{down}) dangling bond bands. X is the signature of a surface exciton in the single-particle band structure. The silicon valence and conduction bands are indicated by the gray-filled areas. Reprinted with permission from Ref. [211]. Copyright (2004) by the American Physical Society. (Please find a color version of this figure on the color plates.)

in Section 2.2.4. For a review on excitons in molecular layers, the reader is referred to Chapter 15 of Volume 1 of this series.

Figure 2.35a depicts the $c(4 \times 2)$ ground-state reconstruction of the Si(100) surface [215]. The lower coordinated atoms at the surface rebond to buckled dimers. They are arranged in rows along the $[0\bar{1}1]$-direction and alternately tilted (black D_{up} and dark gray D_{down} atoms) along and perpendicular to the rows. This structure is observed below 200 K in low-energy electron diffraction (LEED) [216] and predominates in scanning tunneling topographs [217]. Thermal activation of the dimer-rocking mode destroys long-range order [217] and a (2×1) LEED pattern is observed above 200 K.

The half-filled dangling bond states of the dimer split and form the occupied and unoccupied surface bands D_{up} and D_{down}. In Figure 2.35b, a GW-calculation of the surface quasi-particle band structure (solid lines, shaded areas) is compared with the band dispersion (symbols) obtained from 2PPE [211, 214]. The band structure calculation implements many-body exchange and correlation effects among the

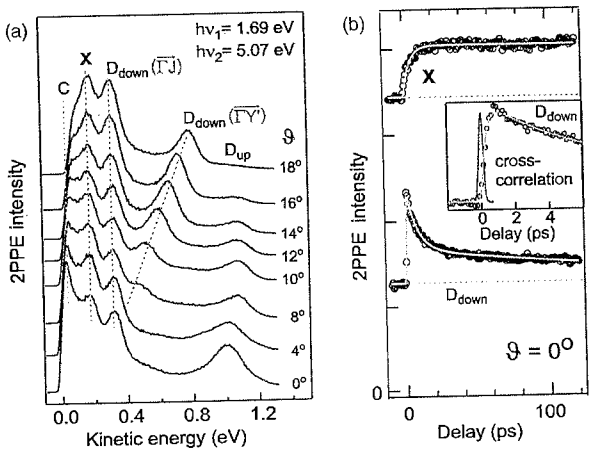

Figure 2.36 (a) Angle-resolved 2PPE spectra of the Si(100) $c(4 \times 2)$ surface recorded at 90 K for in time overlapping pump and probe pulses. (b) Time-resolved 2PPE measurements. Photon energies of the pump and probe pulses are $h\nu_1 = 1.69$ eV and $h\nu_2 = 5.07$ eV. Measurements at $\bar{\Gamma}$ ($\vartheta = 0°$) recorded with the electron analyzer tuned to the peak maxima of X and the D_{down} state. The inset highlights the dynamics of the D_{down} population on an enlarged timescale. Reprinted with permission from Ref. [214]. Copyright (2005) by Springer.

electrons in terms of the dynamical self-energy (see Section 2.2.1) [218–220]. The final and intermediate states of 2PPE (hole in D_{up} and excited electron in D_{down}) are accurately described and the silicon bulk and surface band gaps are reproduced within 100 meV. A set of angle-resolved 2PPE spectra for in-time overlapping pump ($h\nu = 1.69$ eV) and probe pulses ($h\nu = 5.07$ eV) is shown in Figure 2.36a. The assignment of the D_{down} state is based on the pronounced dispersion along the dimer chain ($\overline{\Gamma Y'}$) and the flat band perpendicular to it ($\overline{\Gamma J}$) (see Figure 2.35b). While the measured and calculated binding energies of the occupied D_{up} dangling bond band agree very well, the dispersion does not. This disagreement was confirmed by subsequent experiments and calculations [221, 222] and remains an open question.

Up to now we have assigned the transitions expected for single-particle excitations. Besides the dangling bond bands the spectra in Figure 2.36a reveal additional intensity at the low-energy cutoff C and a nearly nondispersing peak X about 130 meV below the D_{down} band. Both X and C correspond to long-lived surface excitations in the band gap, which are usually attributed to (nearby) surface defects [223]. Adsorption of activated hydrogen or sputtering–annealing cycles support this assignment for tail C, but not for peak X. The latter parallels the behavior of the D_{down} state, that is, gradually loses intensity with H-exposure and degrading surface quality.

Including the interaction between electrons and holes in the many-body theory [224] suggests that X corresponds to emission of an electron from a bound surface exciton state formed between a hole in the D_{up} band and an electron in the D_{down} band. To understand the signature of an excitonic state in 2PPE spectra, we consider

energy conservation. Prior to the photoemission event, the total energy of the system amounts to

$$\begin{aligned} E_{\text{tot}} &= E_0 + \Omega^X + h\nu \\ &\simeq E_0 + E_{\text{gap}}^{\text{surf}} - E_{\text{bind}}^X + h\nu \end{aligned}, \tag{2.144}$$

where E_0 is the ground-state energy and Ω^X is the energy required to form the exciton. After the photoemission event, the total energy reads

$$E_{\text{tot}} = E_0 + E_{\text{kin}} - \langle E_{\text{hole}} \rangle, \tag{2.145}$$

where E_{kin} and $\langle E_{\text{hole}} \rangle$ are the kinetic energy of the photoemitted electron and the average dispersion of the final state hole, respectively. Energy conservation finally yields

$$\begin{aligned} E_{\text{kin}} &= \langle E_{\text{hole}} \rangle + \Omega^X + h\nu \\ &\simeq \langle E_{\text{hole}} \rangle + E_{\text{gap}}^{\text{surf}} - E_{\text{bind}}^X + h\nu \\ &= E_{\text{D}_{\text{down}}} - E_{\text{bind}}^X + h\nu. \end{aligned} \tag{2.146}$$

Since Ω^X and $h\nu$ are fixed, 2PPE measures the initial state, that is, the photohole $E_{\text{kin}} \propto \langle E_{\text{hole}} \rangle$. Thus, the flat dispersion of X reflects mainly the dispersion of the D_{up} dangling bond band, but not the degree of localization of the exciton. Consequently, the dispersion of peak X is flat in all directions, in clear contrast to the strong dispersion of the D_{down} band along the dimer chain. We note that peak X is a single quasi-particle feature and only the shift between X and D_{down} at $\bar{\Gamma}$ corresponds to the binding energy of the surface exciton E_{bind}^X. The calculated binding energy of 100 meV is in good agreement with the measured difference of 130 meV between X and D_{down}. Besides the Si(100) $c(4 \times 2)$ surface reconstruction, Figure 2.35a represents the calculated probability density (contour plot) of an electron in the presence of a hole fixed at the center of the depicted area. The electron's wave function is delocalized along the center dimer row. This quasi one-dimensional localization at the surface is in accord with the large binding energy of the surface exciton.

Before closing this section, we address the dynamics of exciton formation at the Si(100) surface. Referring to the discussion in Section 2.2.4, we note that 2PPE directly probes the (incoherent) population dynamics of the intermediate state. Figure 2.36b compares time-resolved measurements recorded at the bottom of the D_{down} band and at peak X. The maximum population of D_{down} occurs after 1.5 ps. Electrons excited to the D_{down} band decay via phonon emission to the band bottom. This intraband decay leads to a delayed rise of the population at the band bottom. The subsequent dynamics reveals a double-exponential decay of the D_{down} signal with time constants of 7.5 ± 3.5 and 220 ± 30 ps, respectively. Compatible with the shorter time constant, exciton formation (buildup of X) occurs in 5 ± 2.5 ps. The increase in signal X in this time span is almost equal to the decrease in the D_{down} signal (Figure 2.36b). Therefore, nearly all excited electrons, which reach the bottom of the D_{down} band are finally trapped in state X; exciton formation is the dominant surface decay channel. The excitation energy of X amounts to about 0.5 eV, which is

much smaller than the photon energy of 1.69 eV of the initial excitation step. Thus, before an exciton can form, excited electrons and excited holes need to relax via phonon emission toward the band edges. Energy relaxation within surface bands occurs within 1.5 ps via phonon emission. Carrier relaxation involves an energy difference of 130 meV and thus requires simultaneous emission of at least two phonons. This can explain why X is observed only after a relaxation time of about 5 ps. The 220 ps decay constant of the D_{down} signal cannot originate from depopulation of the D_{down} band, but must reflect the decay constant of a reservoir, from where the D_{down} band is repopulated. Electrons excited to unoccupied bulk bands by the infrared laser pulse rapidly relax to the CBM. From there bulk electrons scatter to the D_{down} surface band [211]. The 220 ps decay constant can thus be attributed to the lifetime of the bulk electrons in the CBM. Since peak X does not decay on the picosecond timescale accessed here, the excitonic state must have a lifetime of at least nanoseconds. Peak X and its dynamics have been confirmed by two independent studies [221, 222].

2.4.3.5 Magnon Emission

Thermally excited spin waves are the fundamental excitation of ferromagnets, lowering the magnetization by $2\mu_B$. These collective excitations have been described in detail in Section 2.3.2. Here, we concentrate on magnon emission upon inelastic electron scattering in the itinerant ferromagnet iron. Understanding the generation of such a collective excitation in nonthermal equilibrium is important for developing a microscopic picture of relaxation processes in ferromagnets. The signature of magnons has been found in spin-polarized electron energy loss spectroscopy [139, 225], high-resolution photoemission spectra (Section 2.4.2.4 [131]) and inelastic tunneling spectroscopy [226]. However, these measurements do not address the fundamental problem of the time required to generate a magnon. Based on the small energy of magnons, that is, the dispersion relation $\omega \propto q^2$, spin wave emission is commonly viewed as a slow process, occurring within picoseconds [227].

In the following, the spin-dependent lifetime of the first image potential state at the surface of a ferromagnetic thin iron film on Cu(100) is discussed. It is demonstrated that intraband decay (scattering along the $n = 1$ parabola) is twice as strong for minority spin electrons as compared to their majority counterpart. This can be explained only by magnon emission, which must significantly contribute to inelastic decay on a femtosecond timescale.

The $n = 1$ image potential band was probed by energy-, angle-, and (most important) spin-resolved 2PPE [17]. Details of the experimental apparatus and the spin detector can be found in Refs [228, 229]. Measuring the energy as a function of the momentum parallel to the surface $E(k_{||})$ yields the first and second image potential-state bands ($n = 1, 2$), which show a two-dimensional parabolic dispersion as depicted in Figure 2.37a. Their exchange splitting is a signature of the ferromagnetic order in the iron film at the measurement temperature of 90 K ($T/T_C = 0.24$), where T_C is the Curie temperature [178, 230]. The lifetime τ of electrons photoexcited to the first image potential-state bands is obtained by shifting the time delay between the UV pump and the IR probe pulses. The three possible electronic decay channels

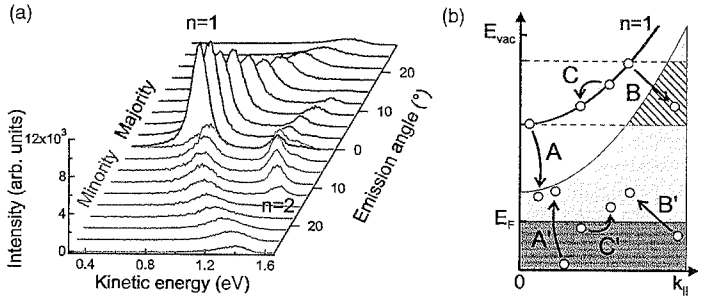

Figure 2.37 (a) Dispersing $n = 1, 2$ image potential-state bands as a function of emission angle parallel to the surface. Majority and minority spin channels are exchange split (data taken from Ref. [17]). (b) The three inelastic decay processes A, B, and C of the $n = 1$ image potential state in the gap of the surface-projected bulk bands (shaded area). In the inelastic decay process, energy and momentum are conserved via electron–hole pair creation A′, B′, and C′.

are sketched in Figure 2.37b. Inelastic decay into empty bulk states is indicated by process A. In this inelastic scattering process, momentum and energy are conserved by an electron–hole pair excited in the iron film A′. For the iron film, the d-bands in the majority spin channel are almost fully occupied, while the d-states in the minority spin channel form an only partially occupied band, exchange split from the majority bands by about 2.5 eV [17]. This spin-dependent density of d-states determines the difference in majority and minority decay rates [176, 177] at the bottom of the image potential-state bands (processes A and A′ in Figure 2.37b).

As illustrated in Figure 2.38a, with increasing energy E above the band minimum E_0, both decay rates increase linearly. However, the minority spin slope is twice as steep as the slope for majority spin electrons ($d\Gamma^{\downarrow}/dE = 0.25 \pm 0.04$ (eV fs)$^{-1}$ versus $d\Gamma^{\uparrow}/dE = 0.12 \pm 0.02$ (eV fs)$^{-1}$).

The increase in the decay rate is due to interband scattering (process B in Figure 2.37b) and intraband scattering (process C) [175, 180]. Energy and momentum are conserved by electron–hole pair creation (processes B′ and C′). The electrons gain additional phase space for decay, which comprises the sp-bands at energies $E > E_0$ (hatched area in Figure 2.37b) and the two-dimensional image potential band (constant density of states). Since the additional phase space for decay is only weakly spin dependent, it *cannot* explain the large difference observed in the slope $d\Gamma/dE$ between minority and majority electrons. This strong spin dependence must therefore stem from spin-flip processes.

A direct spin-flip transition requires strong spin orbit coupling and is therefore inefficient. However, in the exchange spin-flip processes indicated in the Feynman diagrams of Figure 2.37b and c, the primary electron does not change its spin angular momentum but excites substrate electron–hole pairs in the opposite spin channel. Since Stoner excitations have characteristic energies on the order of the exchange splitting of 2.5 eV, they will not play a role in the decay processes B and C with energy transfers below 0.5 eV. In this energy range, magnons play a dominant role in the

lifetime of minority electrons [231]. The magnon spectrum of the 3 ML iron film on Cu(100) is shown in Figure 2.15 and discussed in detail in Section 2.3.2.2. It starts at zero energy and contains two additional branches. With increasing energy of the electron above the band bottom $E > E_0$, these *optical* magnon branches can be excited. At the low temperature of our experiment, magnon absorption by electrons is negligible. We conclude that only for minority spin electrons intraband scattering occurs via magnon emission since the angular momentum of an emitted magnon (reduction by $2\,\mu_B$) is compensated by a flip of a minority to a majority spin electron (increase by $2\,\mu_B$). This process corresponds to magnon emission and leads to an increase in the available phase space for decay. It explains the larger slope $d\Gamma/dE$ for minority compared to majority electrons (Figure 2.38a). As the lifetime of the $n = 1$ minority image potential state on iron is only 11 fs, magnon emission must take place on this timescale and is therefore an ultrafast process contrary to the accepted opinion [227].

2.4.3.6 Magnon–Phonon Interaction

In a ferromagnet, the spin system can be considered as the third heat bath interacting with hot electron and lattice subsystems after laser excitation [206]. The emission of magnons, as described in the last section, does not lead to a change in the total

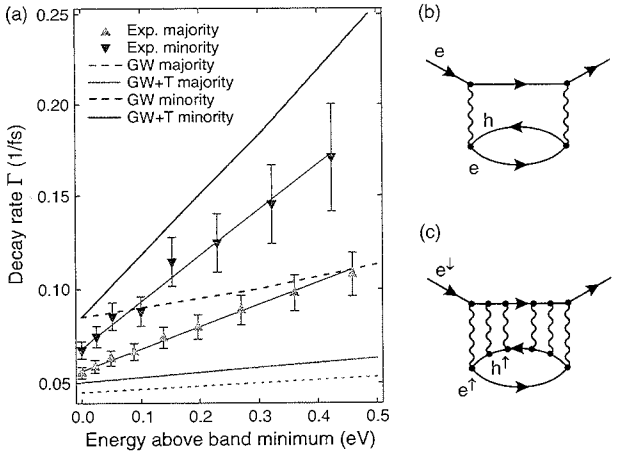

Figure 2.38 (a) Decay rate $1/\tau$ of the $n = 1$ image potential state on the iron film in the majority and minority spin band for increasing energy above the band minimum. The measured decay rates (symbols) are compared with the decay rates of bulk electrons calculated in the GW (dashed lines) and GW + T matrix (solid lines) formalisms. Reprinted with permission from Ref. [17]. Copyright (2010) by the American Physical Society. (b) Feynman diagram for a Stoner excitation, that is, the contribution of electron–hole pair creation in the spin majority channel to the self-energy of a minority spin electron. (c) Magnon emission as a collective excitation can be described as multiple scattering between the primary electron and the hole of an electron–hole pair in the opposite spin channel. Reprinted with permission from Ref. [181].

magnetic momentum *per se*. Admittedly, a change in the magnetization requires angular momentum transfer, for example, to the lattice (Einstein–de Haas effect). This is likewise true for ultrafast laser-driven demagnetization [206, 207] and magnetic switching [208]. To study the spin–lattice interaction, gadolinium is a very suitable model system. In this prototypical Heisenberg ferromagnet (see Section 2.3.2.1), the magnetic moment per atom of $\mu = 7.55\,\mu_B$ is mainly localized at the half-filled 4f core shell ($7.0\,\mu_B$). Below $T_C \simeq 293$ K [232], ferromagnetic order occurs by indirect exchange interaction (Ruderman–Kittel–Kasuya–Yosida) mediated by the spin-polarized $(5d6s)^3$ valence electrons. Since the 4f shell is half-filled, its angular momentum is zero (neglecting core valence hybridization) and the spin-orbit-mediated interaction between the localized 4f magnetic moment and the lattice is weak, as was already established by the pioneering work of Vaterlaus *et al.* [233].

This magnon–phonon coupling in gadolinium was further analyzed in a TR-ARPES experiment at the synchrotron facility BESSY II (Helmholtz-Zentrum Berlin) [170]. A 100 Å thick Gd(0001) film grown epitaxially on W(110) was magnetized with the easy axis in-plane. Figure 2.39a shows angle-resolved Gd 4f core-level spectra recorded at a photon energy of 60 eV with a sample temperature of 120 K. The magnetic linear dichroism (MLD), that is, the contrast between the spectra recorded for reversed magnetization $M\uparrow$ and $M\downarrow$ (see Figure 2.39b), is a measure of the film magnetization. This is proven by the temperature dependence of the MLD,

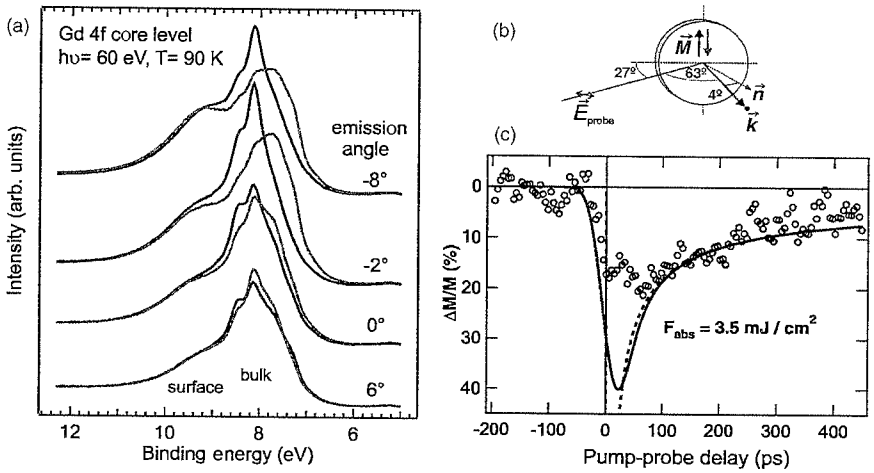

Figure 2.39 (a) Linear magnetic dichroism of the 4f photoemission line (surface and bulk components) of Gd(0001) (adapted from Ref. [234]). (b) Sketch of the measurement geometry. Spectra are recorded close to normal emission (0°) for opposite directions of the in-plane magnetization ($M\uparrow$ and $M\downarrow$). (c) Transient, relative change in the magnetization: measured 4f dichroism (open circles), calculated from lattice temperature and magnetization (dashed line), and convolved with a Gaussian of 50 ps FWHM duration (solid line). Reprinted with permission from Ref. [170]. Copyright (2008) by the American Physical Society. (Please find a color version of this figure on the color plates.)

which was shown to follow the spontaneous magnetization $M(T_l)/M(0)$ [170]. In the TR-ARPES experiment, the Gd electronic system is pumped by an IR laser pulse (synchronized to the BESSY master clock [160]) and the 4f magnetization is probed by the time-delayed synchrotron pulse (50 ps pulse duration). The resulting transient magnetization $M(\Delta t)$ is shown in Figure 2.39c (open circles). A 20 % drop is followed by a recovery of M within 1 ns. A calculation of $M(\Delta t)$ from the transient lattice temperature T_l (see Section 2.4.3.3, Figure 2.33b) and the temperature-dependent magnetization $M(T_l)$ [170, 232] gives the transient magnetization under the assumption that thermal equilibrium is established at all delays. This thermal scenario of $M(\Delta t)$ is plotted in Figure 2.39c by the dashed line. As the lattice reaches a temperature close to T_C at 1.5 ps after the pump pulse, the magnetization drops by 80%. To account for the time resolution governed by the X-ray pulse duration, this temperature dependence is convolved with a Gaussian of 50 ps FWHM and depicted by the solid line in Figure 2.4. Starting at about 80 ps, the measured 4f MLD and the calculated magnetization agree nicely, which substantiates our modeling of $T_l(\Delta t)$. However, the measured drop in the magnetization at earlier times is smaller than expected from the thermal modeling (solid line) by a factor of 2. This confirms that equilibrium between the Gd spin system and the lattice is not established in this time regime. The 4f spin lattice relaxation thus takes much longer than the electron lattice equilibration (1–2 ps). This result was confirmed in a recent X-ray magnetic circular dichroism experiment at the BESSY femtoslicing facility of the Helmholtz-Zentrum Berlin that establishes a spin lattice relaxation time of 40 ps [171].

2.5 Summary

The physical properties of a solid-state system are determined not only by its geometrical and electronic structure. Various elementary excitations also have a crucial role to play. Every response of a solid to external stimuli involves the creation and annihilation of quasi-particles and/or collective excitations. These excitations and their mutual interactions are responsible for most of the fundamental properties of the matter, such as heat and electronic transport, and the optical and magnetic responses. Moreover, the delicate coupling among quasi-particles rules the physics and functionality of correlated systems and can stabilize distinct phases. It is, therefore, of utmost importance to understand the dynamics of elementary excitations, that is, the timescale on which quasi-particle excitations build up and decay.

In this chapter, we have presented an overview of elementary excitations in solids and at solid surfaces and interfaces. Thereby, we have introduced the following quasi-particle and collective excitations: electrons, phonons, excitons, polarons, plasmons, and magnons. We outlined the theoretical concepts to describe their creation and annihilation and discussed various couplings among these excitations. Recent calculations and experiments are highlighted to give an impression of the state of the art of the field.

Neither from a theoretical nor from an experimental viewpoint are the problems presented in this chapter solved. One of the most prominent examples is the pairing

mechanism in high-temperature superconductors, which is still under active debate. For an *ab initio* calculation of the elementary excitations in a solid, we need detailed information on the electronic structure and states, which may by itself become a substantial theoretical problem. This knowledge is then fed into various schemes to calculate the dynamic response. Obviously, we need to know the electronic structure of a material quite accurately to arrive at a reliable description of its dynamics. This problem becomes even more complex in layered structures, and at surfaces and interfaces, where the response function changes quite abruptly and novel one- and two-dimensional electronic states can appear. Since quasi-particle excitations and couplings are often enhanced in low-dimensional systems, the study of surfaces and nanostructures remains a formidable challenge for the future.

References

1 Ashcroft, N. and Mermin, N. (1976) *Solid State Physics*, Saunders.
2 Fürst, C., Leitenstorfer, A., Laubereau, A., and Zimmermann, R. (1997) *Phys. Rev. Lett.*, **78**, 3733.
3 Betz, M., Göger, G., Laubereau, A., Gartner, P., Bányai, L., Haug, H., Ortner, K., Becker, C.R., and Leitenstorfer, A. (2001) *Phys. Rev. Lett.*, **86**, 4684.
4 Petek, H. and Ogawa, S. (1997) *Prog. Surf. Sci.*, **56**, 239.
5 Kittel, C. (1963) *Quantum Theory of Solids*, John Wiley & Sons, New York.
6 Madelung, O. (1978) *Introduction to Solid State Theory*, Springer, Berlin.
7 Czycholl, G. (2000) *Theoretische Festkörperphysik*, Springer, Berlin.
8 Sandratskii, L. (1998) *Adv. Phys.*, **47**, 91.
9 Echenique, P., Berndt, R., Chulkov, E., Fauster, T., Goldmann, A., and Höfer, U. (2004) *Surf. Sci. Rep.*, **52**, 219.
10 Kira, M. and Koch, S.W. (2006) *Prog. Quantum Electron.*, **30**, 155.
11 Pitarke, J.M., Zhukov, V.P., Keyling, R., Chulkov, E.V., and Echenique, P.M. (2004) *ChemPhysChem*, **4**, 1284.
12 Pitarke, J., Silkin, V., Chulkov, E., and Echenique, P. (2007) *Rep. Prog. Phys.*, **70**, 1.
13 Hüfner, S. (1995) *Photoelectron Spectroscopy: Principles and Applications*, Springer Series in Solid-state Science, vol. 82, Springer.
14 Abrikosov, A.A., Gorkov, L.R., and Dzyaloshinski, I.E. (1963) *Methods of Quantum Field Theory in Statistical Physics*, Prentice-Hall, Englewood Cliffs.
15 Chulkov, E.V., Borisov, A.G., Gauyacq, J.P., Sanchez-Portal, D., Silkin, V.M., Zhukov, V.P., and Echenique, P.M. (2006) *Chem. Rev.*, **106**, 4160.
16 Hofmann, P., Sklyadneva, I., Rienks, E., and Chulkov, E. (2009) *New J. Phys.*, **11**, 125005.
17 Schmidt, A.B., Pickel, M., Donath, M., Buczek, P., Ernst, A., Zhukov, V.P., Echenique, P.M., Chulkov, E.V., and Weinelt, M. (2010) *Phys. Rev. Lett.*, **105**, 197401.
18 García-Lekue, A., Pitarke, J.M., Chulkov, E.V., Liebsch, A., and Echenique, P.M. (2002) *Phys. Rev. Lett.*, **89**, 96.
19 Grimvall, G. (1981) *The Electron–Phonon Interaction in Metals, Selected Topics in Solid State Physics* (ed. E. Wohlfarth), vol. 16, North-Holland, New York.
20 Eliashberg, G. (1960) *Sov. Phys. JETP*, **11**, 696.
21 Sklyadneva, I., Chulkov, E., and Echenique, P. (2008) *J. Phys. Condens. Matter*, **20**, 165203.
22 Haug, H. and Koch, S.W. (2009) *Quantum Theory of the Optical and Electronic Properties of Semiconductors*, 5th edn, World Scientific Publ., Singapore.
23 Klingshirn, C. (2005) *Semiconductor Optics*, 2nd edn, Springer, Berlin.

24 Schäfer, W. and Wegener, M. (2002) *Semiconductor Optics and Transport Phenomena*, 1st edn, Springer, Berlin.
25 Zimmermann, R. (1987) *Many-Particle Theory of Highly Excited Semiconductors*, Teubner, Leipzig.
26 Frenkel, J. (1931) *Phys. Rev.*, 37, 1276.
27 Wannier, G.H. (1937) *Phys. Rev.*, 52, 191.
28 Elliott, R. (1963) Theory of excitons, in *Polarons and Excitons* (eds C. Kuper and G. Whitefield), Oliver and Boyd, Edinburgh, pp. 269–293.
29 Knox, R.S. (1963) Theory of excitons, in *Solid State Physics Suppl. 5*, (eds F. Seitz and D. Turnbull), Academic Press, New York.
30 Dexter, D.I. and Knox, R.S. (1981) *Excitons*, John Wiley & Sons, Inc., New York.
31 Lindberg, M. and Koch, S.W. (1988) *Phys. Rev. B*, **38**, 3342.
32 Smith, R., Wahlstrand, J., Funk, A., Mirin, R., Cundiff, S., Steiner, J., Schäfer, M., Kira, M., and Koch, S. (2010) *Phys. Rev. Lett.*, **104**, 247401.
33 Groeneveld, R.M. and Grischkowsky, D. (1994) *J. Opt. Soc. Am. B*, 11, 2502.
34 Kira, M., Hoyer, W., Stroucken, T., and Koch, S.W. (2001) *Phys. Rev. Lett.*, 87, 176401.
35 Chatterjee, S., Ell, C., Mosor, S., Khitrova, G., Gibbs, H.M., Hoyer, W., Kira, M., Koch, S.W., Prineas, J.P., and Stolz, H. (2004) *Phys. Rev. Lett.*, **92**, 067402.
36 Chiaradia, P., Cricenti, A., Selci, S., and Chiarotti, G. (1984) *Phys. Rev. Lett.*, 52, 1145–1147.
37 Reichelt, M., Meier, T., Koch, S.W., and Rohlfing, M. (2003) *Phys. Rev. B*, **68**, 045330.
38 Frohlich, H. (1954) *Adv. Phys.*, 3, 325.
39 Mahan, G. (1990) *Many-Particle Physics*, Plenum.
40 Devreese, J. (2005) Polarons, in *Encyclopedia of Physics* (eds R. Lerner and G. Trigg), Wiley-VCH Verlag GmbH, Weinheim, pp. 2004–2027.
41 Sheng, P. and Dow, J. (1971) *Phys. Rev. B*, 4, 1343.
42 Landau, L. and Pekar, S. (1948) *Z. Eksp. Teor. Fiz.*, **18**, 419.
43 Miyake, S. (1976) *J. Phys. Soc. Jpn.*, **41**, 747.
44 Feynman, R. (1955) *Phys. Rev.*, **97**, 660.
45 Ando, T., Fowler, A., and Stern, F. (1982) *Rev. Mod. Phys.*, 54, 437.
46 Sak, J. (1972) *Phys. Rev. B*, 6, 3981.
47 Xiaoguang, W., Peeters, F., and Devreese, J. (1985) *Phys. Rev. B*, **31**, 3420.
48 Peeters, F., Xiaoguang, W., and Devreese, J. (1988) *Phys. Rev. B*, **37**, 933.
49 Pines, D. and Bohm, D. (1952) *Phys. Rev.*, 85, 338.
50 Tonks, L. and Langmuir, I. (1929) *Phys. Rev.*, 33, 195.
51 Pines, D. and Noziéres, P. (1990) *The Theory of Quantum Liquids*, Addison-Wesley.
52 Raether, H. (1980) *Excitation of Plasmons and Interband Transitions by Electron*, Springer Tracts in Modern Physics, vol. 88, Springer.
53 Ritchie, R. (1957) *Phys. Rev.*, **106**, 874.
54 Raether, H. (1988) *Surface Plasmons on Smooth and Rough Surfaces and on Gratings*, Springer Tracts in Modern Physics, vol. 111, Springer.
55 Jacksonn, J. (1999) *Classical Electrodynamics*, John Wiley & Sons, Inc., New York.
56 Inglesfield, J. (1982) *Rep. Prog. Phys.*, **45**, 223.
57 Silkin, V., Lekue, A.G., Pitarke, J.M., Chulkov, E.V., Zaremba, E., and Echenique, P.M. (2004) *Europhys. Lett.*, **66**, 260.
58 Pitarke, J., Nazarov, V.U., Silkin, V.M., Chulkov, E., Zaremba, E., and Echenique, P. (2005) *Phys. Rev. B*, **70**, 205403.
59 Silkin, V., Pitarke, J.M., Chulkov, E., and Echenique, P.M. (2005) *Phys. Rev. B*, **72**, 115435.
60 Diaconescu, B., Pohl, K., Vattuone, L., Savio, L., Silkin, V.M., Hofmann, P.H., Pitarke, J.M., Chulkov, E., Echenique, P.M., Farias, D., and Rocca, M. (2007) *Nature*, **448**, 57.
61 Gross, E.K.U. and Kohn, W. (1985) *Phys. Rev. Lett.*, **55**, 2850.
62 Dederichs, P.H., Blügel, S., Zeller, R., and Akai, H. (1984) *Phys. Rev. Lett.*, **53**, 2512.

63 Halilov, S.V., Eschrig, H., Perlov, A.Y., and Oppeneer, P.M. (1998) *Phys. Rev. B*, 58, 293.

64 Şaşığlu, E., Sandratskii, L.M., Bruno, P., and Galanakis, I. (2005) *Phys. Rev. B*, 72, 184415.

65 Buczek, P., Ernst, A., Bruno, P., and Sandratskii, L.M. (2009) *Phys. Rev. Lett.*, **102**, 247206.

66 Şaşığlu, E., Schindlmayr, A., Friedrich, C., Freimuth, F., and Blügel, S. (2010) *Phys. Rev. B*, **81**, 054434.

67 Ishioka, K., Hase, M., Kitajima, M., and Petek, H. (2006) *Appl. Phys. Lett.*, **89**, 231916.

68 Dekorsy, T., Cho, G.C., and Kurz, H. (2000) Coherent phonons in condensed media, in *Light Scattering in Solids VIII* (eds M. Cardona and G. Güntherodt), Springer, Berlin, pp. 169–209.

69 Hase, M., Kitajima, M., Nakashima, S., and Mizoguchi, K. (2002) *Phys. Rev. Lett.*, 88, 067401.

70 Misochko, O., Hase, M., Ishioka, K., and Kitajima, M. (2004) *Phys. Rev. Lett.*, **92**, 197401.

71 Ishioka, K., Hase, M., Kitajima, M., Wirtz, L., Rubio, A., and Petek, H. (2008) *Phys. Rev. B*, 77, 121402R.

72 Scholz, R., Pfeifer, T., and Kurz, H. (1993) *Phys. Rev. B*, 47, 16229.

73 Kuznetsov, A. and Stanton, C. (1994) *Phys. Rev. Lett.*, 73, 3243.

74 Hu, X. and Nori, F. (1996) *Phys. Rev. B*, 53, 2419.

75 Dhar, L., Rogers, J., and Nelson, K. (1994) *Chem. Rev.*, **94**, 157.

76 Först, M. and Dekorsy, T. (2007) Coherent phonons in bulk and low-dimensional semiconductors, in *Coherent Vibrational Dynamics* (eds S.D. Silvestri, G. Cerullo, and G. Lanzani), CRC press, Boca Raton, pp. 129–172.

77 Stevens, T., Kuhl, J., and Merlin, R. (2002) *Phys. Rev. B*, 65, 144304.

78 Yee, K.J., Lim, Y.S., Dekorsy, T., and Kim, D.S. (2001) *Phys. Rev. Lett.*, 86, 1630.

79 Garrett, G., Albrecht, T., Whitaker, J., and Merlin, R. (1996) *Phys. Rev. Lett.*, 77, 3661.

80 Riffe, D.M. and Sabbah, A.J. (2007) *Phys. Rev. B*, 76, 085207.

81 Zeiger, H., Vidal, J., Cheng, T., Ippen, E., Dresselhaus, G., and Dresselhaus, M. (1992) *Phys. Rev. B*, **45**, 768.

82 Sokolowski-Tinten, K., Blome, C., Blums, J., Cavalleri, A., Dietrich, C., Tarasevitch, A., Uschmann, I., Förster, E., Kammler, M., Horn von Hoegen, M., and von der Linde, D. (2003) *Nature*, **422**, 287.

83 Zijlstra, E., Tatarinova, L., and Garcia, M. (2006) *Phys. Rev. B*, **74**, 220301.

84 Ishioka, K., Basak, A.K., and Petek H. (2011) *Phys. Rev. B*, 84, 235202.

85 Chang, Y.M., Xu, L., and Tom, H.W.K. (2000) *Chem. Phys.*, **251**, 283.

86 Matsumoto, Y. and Watanabe, K. (2006) *Chem. Rev.*, 106, 4234.

87 Sokolowski-Tinten, K., and von der Linde, D. (2004) *J. Phys. Condens. Matter*, **16**, R1517.

88 Reis, D.A. and Lindenberg, A.M. (2007) Ultrafast X-ray scattering in solids, in *Light Scattering in Solids IX* (eds M. Cardona and R. Merlin), Springer, Berlin, pp. 371–422.

89 Kübler, C., Ehrke, H., Huber, R., Lopez, R., Halabica, A., Haglund, R.F., and Leitenstorfer, A. (2007) *Phys. Rev. Lett.*, **99**, 116401.

90 Perfetti, L., Loukakos, P., Lisowski, M., Bovensiepen, U., Berger, H., Biermann, S., Cornaglia, P., Georges, A., and Wolf, M. (2006) *Phys. Rev. Lett.*, 97, 067402.

91 Schmitt, F., Kirchmann, P.S., Bovensiepen, U., Moore, R.G., Rettig, L., Krenz, M., Chu, J.H., Ru, N., Perfetti, L., Lu, D.H., Wolf, M., Fisher, I.R., and Shen, Z.X. (2008) *Science*, **321**, 1649.

92 Vallee, F. (1994) *Phys. Rev. B*, 49 (4), 2460.

93 Hase, M., Mizoguchi, K., Harima, H., Nakashima, S., and Sakai, K. (1998) *Phys. Rev. B*, 58, 5448.

94 Zhang, J.M., Giehler, M., Göbel, A., Ruf, T., Cardona, M., Haller, E.E., and Itoh, K. (1998) *Phys. Rev. B*, 57, 1348.

95 Ishioka, K., Hase, M., Ushida, K., and Kitajima, M. (2002) *Physica B*, **316–317**, 296.

96 Pisana, S., Lazzeri, M., Casiraghi, C., Novoselov, K., Geim, A., Ferrari, A., and Mauri, F. (2007) *Nat. Mater.*, 6, 198.

97 Lee, J.D., Inoue, J., and Hase, M. (2006) *Phys. Rev. Lett.*, 97, 157405.

98 Misochko, O., Ishioka, K., Hase, M., and Kitajima, M. (2007) *J. Phys.: Condens. Matter*, **19**, 156227.

99 Fukasawa, R. and Perkowitz, S. (1996) *Jpn. J. Appl. Phys.*, 35, 132.

100 Cho, G., Dekorsy, T., Bakker, H., Hövel, R., and Kurz, H. (1996) *Phys. Rev. Lett.*, 77, 4062.

101 Hase, M., Nakashima, S.i., Mizoguchi, K., Harima, H., and Sakai, K. (1999) *Phys. Rev. B*, **60**, 16526.

102 Chang, Y.M. (2002) *Appl. Phys. Lett.*, **80**, 2487.

103 Bakker, H., Hunsche, S., and Kurz, H. (1998) *Rev. Mod. Phys.*, **70**, 523.

104 Bovensiepen, U. (2007) *J. Phys. Condens.: Matter*, **19**, 083201.

105 Thomsen, C., Grahn, H.T., Maris, H.J., and Tauc, J. (1986) *Phys. Rev. B*, 34, 4129.

106 Yamamoto, A., Mishina, T., Masumoto, Y., and Nakayama, M. (1994) *Phys. Rev. Lett.*, **73**, 740.

107 Nelson, K., Miller, R., Lutz, D., and Fayer, M. (1982) *J. Appl. Phys.*, **53** (2), 1144.

108 Wolfe, J.P. (1998) *Imaging Phonons*, Cambridge University Press, Cambridge.

109 Wright, O.B., Matsuda, O., and Sugawara, Y. (2005) *Jpn. J. Appl. Phys.*, **44**, 4292.

110 Cavalleri, A. and Schoenlein, R.W. (2004) Femtosecond X-rays and structural dynamics in condensed matter, in *Ultrafast Dynamical Processes in Semiconductors* (ed. K.T. Tsen), Springer, Berlin, pp. 309–337.

111 Nie, S., Wang, X., Park, H., Clinite, R., and Cao, J. (2006) *Phys. Rev. Lett*, **96**, 025901.

112 Tamura, S. (1983) *Phys. Rev. B*, 27 (2), 858.

113 Tamura, S. (1985) *Phys. Rev. B*, **31** (4), 2574.

114 Okubo, K. and Tamura, S. (1983) *Phys. Rev. B*, **28** (8), 4847.

115 Tas, G. and Maris, H. (1994) *Phys. Rev. B*, 49 (21), 15046.

116 Maris, H. (1990) *Phys. Rev. B*, **41** (14), 9736.

117 Monthoux, P. and Pines, D. (1992) *Phys. Rev. Lett.*, 69, 961.

118 Hengsberger, M., Purdie, D., Segovia, P., Garnier, M., and Baer, Y. (1999) *Phys. Rev. Lett.*, **83**, 592.

119 Valla, T., Fedorov, A.V., Johnson, P.D., and Hulbert, S.L. (1999) *Phys. Rev. Lett.*, 83, 2085.

120 Eschrig, M. and Norman, M.R. (2000) *Phys. Rev. Lett.*, **85**, 3261.

121 Lanzara, A., Bogdanov, P.V., Zhou, X.J., Kellar, S.A., Feng, D.L., Lu, E.D., Yoshida, T., Eisaki, H., Fujimori, A., Kishio, K., Shimoyama, J.I., Noda, T., Uchida, S., Hussain, Z., and Shen, Z.X. (2001) *Nature*, **412**, 510.

122 Kevan, S.D. (ed.) (1992) *Angle-Resolved Photoemission*, Elsevier, Amsterdam.

123 Knapp, J.A., Himpsel, F.J., and Eastman, D.E. (1979) *Phys. Rev. B*, **19**, 4952.

124 Hofmann, A., Cui, X.Y., Schäfer, J., Meyer, S., Höpfner, P., Blumenstein, C., Paul, M., Patthey, L., Rotenberg, E., Bünemann, J., Gebhard, F., Ohm, T., Weber, W., and Claessen, R. (2009) *Phys. Rev. Lett.*, **102**, 187204.

125 Hulpke, E. and Lüdecke, J. (1992) *Phys. Rev. Lett.*, 68, 2846.

126 Rotenberg, E. and Kevan, S.D. (1998) *Phys. Rev. Lett.*, **80**, 2905.

127 Rotenberg, E., Schaefer, J., and Kevan, S.D. (2000) *Phys. Rev. Lett.*, 84, 2925.

128 Mook, H.A. and Nicklow, R.M. (1973) *Phys. Rev. B*, 7, 336.

129 Paul, D.M., Mitchell, P.W., Mook, H.A., and Steigenberger, U. (1988) *Phys. Rev. B*, 38, 580.

130 Jarlborg, T. (2003) *Physica C*, 385, 513.

131 Schäfer, J., Schrupp, D., Rotenberg, E., Rossnagel, K., Koh, H., Blaha, P., and Claessen, R. (2004) *Phys. Rev. Lett.*, **92**, 097205.

132 Dal Corso, A. and de Gironcoli, S. (2000) *Phys. Rev. B*, 62, 273.

133 Benedek, G., Toennies, J.P., and Zhang, G. (1992) *Phys. Rev. Lett.*, 68, 2644.

134 Karlsson, K. and Aryasetiawan, F. (2000) *Phys. Rev. B*, 62, 3006.

135 Blackman, J.A., Morgan, T., and Cooke, J.F. (1985) *Phys. Rev. Lett.*, 55, 2814.

136 Ododo, J.C. and Anyakoha, M.W. (1983) *J. Phys. F Metal Phys.*, **13**, 2335.

137 Plihal, M., Mills, D.L., and Kirschner, J. (1999) *Phys. Rev. Lett.*, **82**, 2579.

138 Edwards, D.M. and Hertz, J.A. (1973) *J. Phys. F*, **3**, 2191.

139 Vollmer, R., Etzkorn, M., Anil Kumar, P., Ibach, H., and Kirschner, J. (2003) *Phys. Rev. Lett.*, **91**, 147201.

140 Tang, W.X., Zhang, Y., Tudosa, I., Prokop, J., Etzkorn, M., and Kirschner, J. (2007) *Phys. Rev. Lett.*, **99**, 087202.

141 Mook, H.A. and Paul, D.M. (1985) *Phys. Rev. Lett.*, **54**, 227.

142 Magnuson, M., Nilsson, A., Weinelt, M., and Mårtensson, N. (1999) *Phys. Rev. B*, **60**, 2436.

143 Eberhardt, W. and Plummer, E.W. (1980) *Phys. Rev. B*, **21**, 3245.

144 Bünemann, J., Weber, W., and Gebhard, F. (1998) *Phys. Rev. B*, **57**, 6896.

145 Bünemann, J., Gebhard, F., Ohm, T., Weiser, S., and Weber, W. (2008) *Phys. Rev. Lett.*, **101**, 236404.

146 Bünemann, J., Gebhard, F., Ohm, T., Umstätter, R., Weiser, S., Weber, W., Claessen, R., Ehm, D., Harasawa, A., Kakizaki, A., Kimura, A., Nicolay, G., Shin, S., and Strocov, V.N. (2003) *Europhys. Lett.*, **61**, 667.

147 Higashiguchi, M., Shimada, K., Nishiura, K., Cui, X., Namatame, H., and Taniguchi, M. (2005) *Phys. Rev. B*, **72**, 214438.

148 Halilov, S.V., Eschrig, H., Perlov, A.Y., and Oppeneer, P.M. (1998) *Phys. Rev. B*, **58**, 293.

149 Brown, R.H., Nicholson, D.M.C., Wang, X., and Schulthess, T.C. (1999) *J. App. Phys.*, **85**, 4830.

150 Takumi Watanabe, Y.K., Hirano, M., and Hosono, H. (2008) *J. Am. Chem. Soc.*, **130**, 3296.

151 Mazin, I.I., Singh, D.J., Johannes, M.D., and Du, M.H. (2008) *Phys. Rev. Lett.*, **101**, 057003.

152 Macridin, A., Jarrell, M., Maier, T., and Scalapino, D.J. (2007) *Phys. Rev. Lett.*, **99**, 237001.

153 Tan, F., Wan, Y., and Wang, Q.H. (2007) *Phys. Rev. B*, **76**, 054505.

154 Kakehashi, Y. and Fulde, P. (2005) *J. Phys. Soc. Jpn.*, **74**, 2397.

155 Byczuk, K., Kollar, M., Held, K., Yang, Y.F., Nekrasov, I.A., Pruschke, T., and Vollhardt, D. (2007) *Nat. Phys.*, **3**, 168.

156 Raas, C., Grete, P., and Uhrig, G.S. (2009) *Phys. Rev. Lett.*, **102**, 076406.

157 Reed, M.K., Steiner-Shepard, M.K., Armas, M.S., and Negus, D.K. (1995) *J. Opt. Soc. Am. B*, **11**, 2229.

158 Mathias, S., Bauer, M., Aeschlimann, M., Miaja-Avila, L., Kapteyn, H.C., and Murnane, M.M. (2010) Time-resolved photoelectron spectroscopy at surfaces using femtosecond XUV pulses, in *Dynamics at Solid State Surfaces and Interfaces Volume 1: Current Developments* (eds U. Bovensiepen, H. Petek, and M. Wolf), Wiley-VCH Verlag GmbH, Berlin, pp. 501–536.

159 Kirchmann, P.S., Perfetti, L., Wolf, M., and Bovensiepen, U. (2010) Femtosecond time- and angle-resolved photoemission as a real-time probe of cooperative effects in correlated electron materials, in *Dynamics at Solid State Surfaces and Interfaces Volume 1: Current Developments* (eds U. Bovensiepen, H. Petek, and M. Wolf), Wiley-VCH Verlag GmbH, Berlin, pp. 475–498.

160 Gießel, T., Bröcker, D., Schmidt, P., and Widdra, W. (2003) *Rev. Sci. Instrum.*, **74**, 4620.

161 Cavalieri, A.L., Fritz, D.M., Lee, S.H., Bucksbaum, P.H., Reis, D.A., Rudati, J., Mills, D.M., Fuoss, P.H., Stephenson, G.B., Kao, C.C., Siddons, D.P., Lowney, D.P., MacPhee, A.G., Weinstein, D., Falcone, R.W., Pahl, R., Als-Nielsen, J., Blome, C., Düsterer, S., Ischebeck, R., Schlarb, H., Schulte-Schrepping, H., Tschentscher, T., Schneider, J., Hignette, O., Sette, F., Sokolowski-Tinten, K., Chapman, H.N., Lee, R.W., Hansen, T.N., Synnergren, O., Larsson, J., Techert, S., Sheppard, J., Wark, J.S., Bergh, M., Caleman, C., Huldt, G., van der Spoel, D., Timneanu, N., Hajdu, J., Akre, R.A., Bong, E., Emma, P., Krejcik, P., Arthur, J., Brennan, S., Gaffney, K.J., Lindenberg, A.M., Luening, K., and Hastings, J.B. (2005) *Phys. Rev. Lett*, 94 114801.

162 Gahl, C., Azima, A., Beye, M., Deppe, M., Döbrich, K., Hasslinger, U., Hennies, F., Melnikov, A., Nagasono, M., Pietzsch, A., Wolf, M., Wurth, W., and Föhlisch, A. (2008) *Nat. Photonics*, **2**, 165.

163 Haight, R. (1995) *Surf. Sci. Rep.*, **21**, 275.

164 Bauer, M. (2005) *J. Phys. D Appl. Phys.*, **38**, R253.

165 Cavalieri, A.L., Krausz, F., Ernstorfer, R., Kienberger, R., Feulner, P., Barth, J.V., and Menzel, D. (2010) Attosecond time-resolved spectroscopy at surfaces, in *Dynamics at Solid State Surfaces and Interfaces Volume 1: Current Developments* (eds U. Bovensiepen, H. Petek, and M. Wolf), Wiley-VCH Verlag GmbH, Berlin, pp. 537–554.

166 Passlack, S., Mathias, S., Andreyev, O., Mittnacht, D., Aeschlimann, M., and Bauer, M. (2006) *J. Appl. Phys.*, **100**, 024912.

167 Pietzsch, A., Föhlisch, A., Beye, M., Deppe, M., Hennies, F., Nagasono, M., Suljoti, E., Wurth, W., Gahl, C., Döbrich, K., and Melnikov, A. (2008) *New J. Phys.*, **10**, 033004.

168 Melnikov, A., Povolotskiy, A., and Bovensiepen, U. (2008) *Phys. Rev. Lett.*, **100**, 247401.

169 Perfetti, L., Loukakos, P.A., Lisowski, M., Bovensiepen, U., Wolf, M., Berger, H., Biermann, S., and Georges, A. (2008) *New J. Phys.*, **10**, 053019.

170 Melnikov, A., Prima-Garcia, H., Lisowski, M., Gießel, T., Weber, R., Schmidt, R., Gahl, C., Bulgakova, N.M., Bovensiepen, U., and Weinelt, M. (2008) *Phys. Rev. Lett.*, **100**, 107202.

171 Wietstruk, M., Melnikov, A., Stamm, C., Kachel, T., Pontius, N., Sultan, M., Gahl, C., Weinelt, M., Dürr, H.A., and Bovensiepen, U. (2011) *Phys. Rev. Lett.*, **106**, 127401.

172 Höfer, U., Shumay, I.L. Reuß, Ch., Thomann, U., Wallauer, W., and Fauster, T. (1997) *Science*, 277, 1480.

173 Shumay, I.L., Höfer, U., Reuß, C., Thomann, U., Wallauer, W., and Fauster, T. (1998) *Phys. Rev. B*, **58**, 13974.

174 Knoesel, E., Hotzel, A., and Wolf, M. (1998) *J. Electron. Spectrosc. Relat. Phenom.*, **88–91**, 577.

175 Weinelt, M. (2002) *J. Phys. Condens. Matter*, **14**, R1099.

176 Passek, F., Donath, M., Ertl, K., and Dose, V. (1995) *Phys. Rev. Lett.*, **75**, 2746.

177 Aeschlimann, M., Bauer, M., Pawlik, S., Weber, W., Burgermeister, R., Oberli, D., and Siegmann, H. (1997) *Phys. Rev. Lett.*, **79**, 5158.

178 Schmidt, A., Pickel, M., Wiemhöfer, M., Donath, M., and Weinelt, M. (2005) *Phys. Rev. Lett.*, **95**, 107402.

179 Goris, A., Döbrich, K.M., Panzer, I., Schmidt, A.B., Donath, M., and Weinelt, M. (2011) *Phys. Rev. Lett.*, **107**, 026601.

180 Berthold, W., Höfer, U., Feulner, P., Chulkov, E., Silkin, V., and Echenique, P. (2002) *Phys. Rev. Lett.*, **88**, 056805.

181 Schmidt, A.B. (2008) Spin-dependent electron dynamics in front of ferromagnetic surfaces. PhD thesis, Freie Universität Berlin.

182 Zhukov, V.P. and Chulkov, E.V. (2009) *Physics Uspekhi*, 52, 105.

183 Ogawa, S., Nagano, H., and Petek, H. (1997) *Phys. Rev. B*, **55**, 10869.

184 Pawlik, S., Bauer, M., and Aeschlimann, M. (1997) *Surf. Sci.*, **377–379**, 206.

185 Cao, J., Gao, Y., Miller, R.J.D., Elsayed-Ali, H.E., and Mantell, D.A. (1997) *Phys. Rev. B*, **56**, 1099.

186 Knoesel, E., Hotzel, A., and Wolf, M. (1998) *Phys. Rev. B*, **57**, 12812.

187 Gerlach, A., Berge, K., Goldmann, A., Campillo, I., Rubio, A., Pitarke, J.M., and Echenique, P.M. (2001) *Phys. Rev. B*, **64**, 085423.

188 Zhukov, V.P., Aryasetiawan, F., Chulkov, E.V., de Gurtubay, I.G., and Echenique, P.M. (2001) *Phys. Rev. B*, **64**, 195122.

189 Kittel, C. (1996) *Introduction to Solid State Physics*, John Wiley & Sons, Inc., New York.

190 Lengeler, B. (1978) Electronic structure of noble metals, and polariton-mediated light scattering, in *Springer Tracts in Modern Physics*, vol. 82 (ed. G. Höhler), Springer, Heidelberg, p. 1.

191 Schöne, W.D., Keyling, R., Bandić, M., and Ekardt, W. (1999) *Phys. Rev. B*, **60**, 8616.

192 Halas, N.J. and Bokor, J. (1989) *Phys. Rev. Lett.*, **62**, 1679.

193 Fann, W.S., Storz, R., Tom, H.W.K., and Bokor, J. (1992) *Phys. Rev. B*, **46**, 13592.

194 Lisowski, M., Loukakos, P.A., Bovensiepen, U., Stähler, J., Gahl, C., and Wolf, M. (2004) *Appl. Phys. A*, **78**, 165.

195 Jeong, S., Zacharias, H., and Bokor, J. (1996) *Phys. Rev. B*, 54, R17300.

196 Jeong, S. and Bokor, J. (1999) *Phys. Rev. B*, 59, 4943.

197 Ichibayashi, T. and Tanimura, K. (2009) *Phys. Rev. Lett.*, **102**, 087403.

198 Elsaesser, T., Shah, J., Rota, L., and Lugli, P. (1991) *Phys. Rev. Lett.*, **66**, 1757.

199 Anisimov, S.I., Kapeliovich, B.L., and Perel'man, T.L. (1974) *Sov. Phys. JETP*, **39**, 375.

200 Bonn, M., Denzler, D.N., Funk, S., Wolf, M., Wellershoff, S.S., and Hohlfeld, J. (2000) *Phys. Rev. B*, **61**, 1101.

201 Kaganov, M.I., Lifschits, I.M., and Tanatarov, L.V. (1957) *Sov. Phys. JETP*, 4, 173.

202 Groeneveld, R.H.M., Sprik, R., and Lagendijk, A. (1995) *Phys. Rev. B*, **51**, 11433.

203 Petek, H., Weida, M.J., Nagano, H., and Ogawa, S. (2000) *Science*, **288**, 1402.

204 Bonn, M., Funk, S., Hess, C., Denzler, D.N., Stampfl, C., Scheffler, M., Wolf, M., and Ertl, G. (1999) *Science*, **285**, 1042.

205 Hagen, S., Kate, P., Leyssner, F., Nandi, D., Wolf, M., and Tegeder, P. (2008) *J. Chem. Phys.*, **129**, 164102.

206 Beaurepaire, E., Merle, J.C., Daunois, A., and Bigot, J.Y. (1996) *Phys. Rev. Lett.*, **76**, 4250.

207 Stamm, C. *et al.* (2007) *Nat. Mater.*, **6**, 740.

208 Stanciu, C.D., Hansteen, F., Kimel, A.V., Kirilyuk, A., Tsukamoto, A., Itoh, A., and Rasing, T. (2007) *Phys. Rev. Lett.*, **99**, 047601.

209 Downer, M.C. and Shank, C.V. (1986) *Phys. Rev. Lett.*, **56**, 761.

210 Dziewior, J. and Schmid, W. (1977) *Appl. Phys. Lett.*, 31, 346.

211 Weinelt, M., Kutschera, M., Fauster, T., and Rohlfing, M. (2004) *Phys. Rev. Lett.*, **92**, 126801.

212 Sjodin, T., Petek, H., and Dai, H.L. (1998) *Phys. Rev. Lett.*, 81, 5664.

213 Loukakos, P.A., Lisowski, M., Bihlmayer, G., Blügel, S., Wolf, M., and Bovensiepen, U. (2007) *Phys. Rev. Lett.*, **98**, 097401.

214 Weinelt, M., Kutschera, M., Schmidt, R., Orth, C., Fauster, T., and Rohlfing, M. (2005) *Appl. Phys. A*, **80**, 995.

215 Ramstad, A., Brocks, G., and Kelly, P.J. (1995) *Phys. Rev. B*, **51**, 14504.

216 Tabata, T., Aruga, T., and Murata, Y. (1987) *Surf. Sci.*, 179, L63.

217 Wolkow, R.A. (1992) *Phys. Rev. Lett.*, 68, 2636.

218 Krüger, P. and Pollmann, J. (1995) *Phys. Rev. Lett.*, 74, 1155.

219 Pollmann, J., Krüger, P., Rohlfing, M., Sabisch, M., and Vogel, D. (1996) *Appl. Surf. Sci.*, **104**, 1.

220 Pollmann, J. and Krüger, P. (2000) Chapter 2: Electronic structure of semiconductor surfaces, in *Handbook of Surface Science* (eds K. Horn and M. Scheffler), Elsevier Science B.V.

221 Hagen F S. (2005) Adsorption molekularer schalter und elektronendynamik an Si(100)- und Si (100)-H-oberflächen. Diploma thesis, Freie Universität Berlin.

222 Eickhoff, C. (2010) Time-resolved two-photon photoemission at the Si(001)-surface. PhD thesis, Freie Universität Berlin.

223 Hamers, R.J. and Köhler, U.K. (1989) *J. Vac. Sci. Tech. A*, 7, 2854.

224 Rohlfing, M., and Louie, S.G. (1999) *Phys. Rev. Lett.*, **83**, 856.

225 Vollmer, R., Etzkorn, M., Kumar, P.A., Ibach, H., and Kirschner, J. (2004) *Thin Solid Films*, **464–465**, 42.

226 Balashov, T., Takács, A.F., Wulfhekel, W., and Kirschner, J. (2006) *Phys. Rev. Lett.*, **97**, 187201.

227 Stöhr, J. and Siegmann, H. (2006) *Magnetism: From Fundamentals to Nanoscale Dynamics*, Springer, Berlin.

228 Weinelt, M., Schmidt, A., Pickel, M., and Donath, M. (2007) *Prog. Surf. Sci.*, **82**, 388.

229 Weinelt, M., Schmidt, A., Pickel, M., and Donath, M. (2010) Spin-dependent relaxation of hot electrons on ferromagnetic surfaces, in *Dynamics at Solid State Surfaces and Interfaces Volume 1: Current Developments* (eds U. Bovensiepen, H. Petek, and M. Wolf), Wiley-VCH Verlag GmbH, Berlin, pp. 115–144.

230 Thomassen, J., May, F., Feldmann, B., Wuttig, M., and Ibach, H. (1992) *Phys. Rev. Lett.*, **69**, 3831.

231 Hong, J. and Mills, D. (2000) *Phys. Rev. B*, **62**, 5589.

232 Nigh, H.E., Legvold, S., and Spedding, F.H. (1963) *Phys. Rev.*, **132**, 1092.

233 Vaterlaus, A., Beutler, T., and Meier, F. (1991) *Phys. Rev. Lett.*, **67**, 3314.

234 Prima-Garcia, H. (2007) Laser-induced structural changes at surfaces investigated with synchrotron radiation. PhD thesis, Freie Universität Berlin.